Time-resolved fluorescence spectroscopic and microscopic investigation of biological barriers and nanosized drug delivery systems

Dissertation

zur Erlangung des Grades eines Doktors der Naturwissenschaften

am Fachbereich Physik

der Freien Universität Berlin

vorgelegt von

Johannes Stellmacher

Berlin 2021

Erstgutachterin: Prof. Dr. Ulrike Alexiev

Zweitgutachter: Prof. Dr. Holger Dau

Tag der Disputation: 12.03.21

Zusammenfassung

Für die Entwicklung neuartiger Strategien für die Medikamentenverabreichung sind umfassende Kenntnisse über die Penetrationswege, die physikalisch-chemischen Eigenschaften der beteiligten biologischen Barrieren und die Wechselwirkungen mit dem Medikament von größter Bedeutung. In dieser Arbeit habe ich biophysikalische Techniken wie zeitaufgelöste Fluoreszenzspektroskopie und -mikroskopie in Verbindung mit fortgeschrittenen analytischen Methoden eingesetzt, um neue Einblicke in die Struktur biologischer Barrieren sowie in die biomolekularen Wechselwirkungen von Arzneimitteln und Arzneimittelmimetika im Gewebe zu gewinnen.

Fluoreszierende molekulare Rotoren sind Fluorophore, mit deren Hilfe die lokale Nanoviskosität anhand der Fluoreszenzlebensdauer erfasst werden kann. Ich habe diese Sonden auf künstliche Lipidvesikel appliziert, um Membranviskositäten und Lipidphasenübergänge zu bestimmen. In lebenden Zellen des Gastrointestinaltraktes wurden sie verwendet, um das 3D-Viskositätsprofil der Schleimschicht, die den Dünndarm auskleidet, abzubilden und diese Diffusionsbarriere mit bisher unerreichter Präzision und räumlicher Auflösung zu charakterisieren. Die extrahierten Gradienten und Heterogenitäten des Muzinnetzwerks wurden auf der Grundlage der Kultivierungsbedingungen der schleimproduzierenden Epithelzellen verglichen, wodurch ein Rahmen für physiologische Zellwachstumsbedingungen erarbeitet werden kann.

Bei der Fluoreszenz Lebenszeit Mikroskopie (FLIM) kann die Zielfluoreszenz eines Moleküls anhand der Fluoreszenzlebensdauer vom autofluoreszierenden Hintergrund des umgebenden Gewebes unterschieden werden. Ich nutzte diesen Vorteil, um hintergrundfreie Penetrationsprofile des Wirkstoffmimetikums Nile Red in menschlicher Haut zu erstellen, um biophysikalische Eigenschaften der äußersten Barriere des Körpers zu extrahieren und die freie Penetration mit der durch Nanopartikel unterstützten Penetration über verschiedene transdermale Transportwege zu vergleichen.

Schließlich entwickelten wir eine neuartige Plattform für die Markierung von Biomolekülen mit einem Fluorophor und einem Spin-Label. Das multiplexte Auslesen von FLIM- und EPR-Daten ermöglicht die gleichzeitige Bestimmung der räumlich aufgelösten Zielmolekülkonzentration und die Charakterisierung derer unmittelbaren Umgebung, wobei analytische Inkonsistenzen, die sich aus der individuellen Markierung ergeben, vermieden werden.

Diese Arbeit demonstriert die Leistungsfähigkeit zeitaufgelöster Fluoreszenztechniken, wenn sie mit geeigneten analytischen Strategien für die Anwendung in der biophysikalischen Forschung und der Entwicklung neuer Arzneimitteltransportsysteme gepaart werden.

Abstract

For the development of novel strategies for drug administrations, extensive knowledge over the delivery pathways, the physicochemical properties of the involved biological barriers, and the interactions with the drug are of paramount importance. In this thesis, I employed biophysical techniques like time-resolved fluorescence spectroscopy and microscopy in conjunction with advanced analytical tools to gain new insight into the structure of epithelial barriers as well as the biomolecular interactions of drugs and drug mimetics in the tissue.

Fluorescent molecular rotors are fluorophores, which can be used to sense local nanoviscosity using their fluorescence lifetime. I applied these probes to artificial vesicles, in order to determine membrane viscosities and lipid phase transitions. In living cells of the gastrointestinal tract, they were used to map the 3D viscosity profile of the mucus layer lining the small intestine and characterize this diffusion barrier with unprecedented precision and spatial resolution. The extracted gradients and heterogeneities of the mucin network were compared based on culturing circumstances of the mucus producing epithelial cells, setting a framework for physiological cell growing conditions.

In fluorescence lifetime imaging microscopy (FLIM), the target fluorescence of a molecular of interest can be discriminated from the autofluorescent background of the surrounding tissue based on the fluorescence lifetime. I used this advantage to generate background free penetration profiles of the drug mimetic Nile Red in human skin to extract biophysical properties of the outermost barrier of the body and compare unaided penetration with nanoparticle-assisted administration through various transdermal delivery routes.

We finally developed a novel platform for labeling biomolecules with a fluorophore and a spin label. The multiplexed read-out of FLIM and EPR data facilitates the simultaneous determination of spatially resolved target molecule concentration and characterization of its immediate environment while avoiding analytical inconsistencies resulting from individual labeling.

This thesis demonstrates the capabilities of time-resolved fluorescence techniques when paired with proper analytical strategies for the application in biophysical research and the development of new drug delivery systems.

Table of Content

Table of Content 8
1 Introduction 11
1.1 Aim 12
2 Fundamentals 15
2.1 Fluorescence 15
2.1.1 Time-resolved fluorescence and time correlated single photon counting (TCSPC) 16
2.1.2 Quenching, energy transfer, and photoisomerization 17
2.2 Biological tissue and its relation to physics 23
2.2.1 Internal tissue barrier: mucus/mucosa 23
2.2.2 External tissue barrier: skin 31
3 Materials and Methods 39
3.1 Fluorescent reporter groups 39
3.2 Steady-state absorption and fluorescence emission spectroscopy 41
3.3 Time-dependent fluorescence decay measurements of fluorescent ensembles 41
3.4 Time-domain fluorescence lifetime imaging microscopy 43
3.5 Data analysis 45
3.5.1 Analysis of FLIM data using Cluster-FLIM 45
3.5.2 Lifetime fitting and exhaustive error analysis 48
3.6 Parallax method for determination of dPGS-ICCs membrane incorporation 49
3.7 Lipid vesicle preparation 49
3.8 Determination of apparent binding affinity of WGA-ICC 50
3.9 Rotational viscometer 50
3.10 The fluorescence-EPR dual label 51
3.11 Partition coefficient (n-octanol/water) determination of RhoB and DL 51
3.12 Skin sample preparation for dual label penetration 52
3.13 Loading of pH-sensitive nanoparticle and treatment of skin sections 53

3.14 Cell lines 53
3.14.1 HT29-MTX / Caco2 53
3.14.2 Human oral keratinocytes and squamous cell carcinoma (SCC-25, UM-SCC-22B) 54
3.15 Murine mucus samples 54
3.16 Labeling of cetuximab with FITC 54
4 Results and Discussion 57
4.1 ICC as a nanoviscosity probe in cell membrane and native mucus 57
4.1.1 Interaction of dPGS-ICC with spin-labeled lipids in MLV to facilitate sensing of lipid phase transitions and nanoviscosities in lipid membranes 59
4.1.2 Characterization of ICC excited state parameters and lifetime calibration for the complex mucus viscosity 65
4.1.3 Mucus viscosity determination in live cells using FLIM 74
4.1.4 ICC as viscosity sensor in murine mucus 84
4.2 Application of Cluster-FLIM to generate background free penetration profiles 86
4.2.1 Nanoparticle-enhanced drug delivery across the biological barriers of the skin 86
4.2.2 Drug interaction with tumor-microenvironment of epithelial mucosa squamous cell carcinoma model 93
4.3 Multiplexed FLIM-EPR spectroscopy: a dual fluorescence-spin label probe for the visualization and quantification of target molecules in tissue 99
5 Summary 109
Publications 113
References 115
Appendix 129
Selbstständigkeitserklärung 141
Danksagung 143

Abbreviations

AOTF	acousto-optic tunable filter
AU	airy units
CFD	constant fraction discriminator
DL	dual label
DMPC	1,2-dimyristoyl-sn-glycero-3-phosphocholine
DOPC	1,2-dioleoyl-sn-glycero-3-phosphocholine
dPGS	dendritic polyglycerol sulfate
EPR	electron paramagnetic resonance
FFA	free fatty acid
FITC	fluorescein isothiocyanate
FLIM	fluorescence lifetime imaging microscopy
FWHM	full width half maximum
HEC	hydroxyethyl cellulose
IC	internal conversion
ICC	Indocarbocyanine
IgA	immunoglobulin A
IRF	instrument response function
ISC	inter system crossing
LP	lamina propria
LUV	large unilamellar vesicle
MCP	multi-channel plate
MLV	mulitlamellar vesicle
NAG	N-acetylglucosamine
NHS	N-hydroxysuccinimid
NR	nile red
PI	photoisomerization
Rho B	rhodamine B
SC	stratum corneum
SCC	squamous cell carcinoma
SD	standard deviation
SG	stratum granulosum
SNR	signal-to-noise ratio
SSp	stratum spinosum
SUV	small unilamellar vesicle
TAC	time to amplitude converter
TCSPC	time correlated single photon counting
Ti:Sa	titanium-doped sapphire laser
VE	viable epidermis
WGA	wheat germ agglutinin

1 Introduction

Despite tremendous efforts in fundamental research, new drug development often suffers from low success rates in clinical trials frequently rooted in poor bioavailability or efficacy in the target tissue[1,2]. Beside improper study design or interspecies differences, and insufficient knowledge about the involved barriers leads to unsatisfactory results.

The human body possesses a multitude of distinct protective structures on an array of magnitudes, ranging from the cell membrane over endothelial barriers, such as the blood-brain barrier, to multi-layered organs like the skin, or the mucosa found on all wet interfaces like the gastro-intestinal or the respiratory tract. Generally, these barriers are designed to facilitate some degree of beneficial exchange with the environment while protecting against foreign materials and pathogens. Thus, the structure of these biological barriers needs to be at the core of research interested in the design of controlled drug delivery systems[3-5].

At the cellular level, membrane viscosity is tightly regulated, and the homeostasis of membrane fluidity is most important for the appropriate function of membrane bound proteins as well as for vesicle mediated uptake and transport through the cell. Various diseases are linked to the inability to stabilize membrane fluidity[6,7] and also viruses, drugs and nanoparticles have been found to alter membrane viscosity[8-12].

On the tissue level, the mucosa and the barrier qualities of the adjoined mucus layer are poorly understood. Mucus is best described as a non-Newtonian gel on the macroscale, characterized by a reduction of viscosity as response to high shear rates[13], which is important for mucus clearance in the airways and helps with food transport during peristalsis. On the nanoscale, its properties are very dependent on size and constitution of the probe used for investigation. Currently, most techniques measure bulk viscosity which lack spatial resolution and hence fail to replicate minute changes of mucus properties in the gradient directly at the epithelial surface. Alteration of mucus composition in response to pathogenic triggers or pathological thickening as seen in cystic fibrosis further complicate the situation and lead to the current lack of understanding.

For the topical treatment of skin diseases, therapeutic effect strongly depends on bioavailability of the drug in different skin layers. For this purpose, a careful analysis of the biological barriers which drugs need to overcome is key to evaluate feasible penetration pathways and helps in the development of successful dermatotherapy.

For the characterization of these biological barriers and the assessment of drug delivery systems design to overcome them, fluorescence is an especially suitable and powerful tool. The

fluorescence lifetime is often sensitive to the immediate microenvironment of the fluorophore and can report on local pH, polarity, viscosity, and other biomolecular interactions[14-20]. In combination with microscopy techniques like fluorescence lifetime imaging, it can be used to spatially resolve a multitude of parameters from the cellular to the tissue level.

1.1 Aim

The aim of this work is to use and refine state-of-the-art time-resolved spectroscopic and microscopic techniques in order to further the understanding of modern drug delivery systems und uptake pathways. Fluorescence lifetime imaging (FLIM) is of particular interest for life sciences as it is able to visualize endogenous and exogenous fluorophores on the subcelluar and even suborganelle level[14,15,21,22]. It is mostly independent of fluorophore concentration and optical loss in the sample while being sensitive to the local environment and reliably reports on physicochemical parameters like local pH, viscosity, or reactive oxygen species[17,18,23]. Hence, FLIM is the perfect tool to investigate drug delivery pathways, visualize their biodistribution, and characterize the microenvironment of labeled biomolecules and nanoparticles.

Our newly developed multivariate Cluster-FLIM analysis tool further extends the potential of time-resolved fluorescence data as the fitting-free algorithm dynamically optimizes low photon statistics to yield unique fluorescence lifetime signatures with high contrast and without sacrificing spatial resolution.

Fluorescent molecular rotors to probe nanoviscosity

In order to understand drug penetration pathways and diffusion profiles, knowledge about the immediate nanoscopic environment in biological target structures is of utmost importance. One of the most influential parameters for particle diffusion is the viscosity. Fluorophores have been extensively used to probe viscosity in different scenarios, using fluorescence depolarization[24], fluorescence recovery after photobleaching[25], and fluorescence correlation spectroscopy[26]. Fluorescent molecular rotors like Indocarbocyanine (ICC) use the increasing quantum yield due to a prolonged excited state lifetime in a viscous environment as read-out, which makes them tremendously versatile for the characterization of viscosity gradients of the mucus layer *in vivo*. After initial viscosity calibration of the fluorescence lifetime of ICC, it can be used to map membrane viscosities and identify different membrane domains in artificial membrane systems and living cells. With the help of lectins, which have a high affinity for the sugar sidechains of mucins, ICC will be labeled to mucin and report on local viscosity of mucus. Using FLIM one can reconstruct a 3D map of mucus layer viscosity on living cells and reveal gradients and heterogeneities.

Background free penetration profiles of drugs and drug mimetics in tissue

The fluorescence lifetime can be used to unambiguously discriminate target fluorescence from the autofluorescent background of the tissue. As a direct consequence, drug distribution can be studied in much more detail and direct comparison of drug penetration profiles in tissue with different levels of autofluorescence, like the skin and the hair follicle, becomes feasible. These penetration profiles will provide deeper insight into the biophysical properties which regulate epidermal translocation. Furthermore, the fluorescence lifetime contains indications for drug interactions within the tissue. Thus, FLIM allows to spatially resolve sites of drug accumulation and recognize unique features in the target tissue for the exploitation for directed drug delivery.

Multiplexed FLIM-EPR read-out for drug localization and quantification

FLIM and electron paramagnetic resonance (EPR) spectroscopy are complementary methods. FLIM provides environmental sensitivity, reports on the biomolecular interactions, and spatially resolves the penetration profile of biomolecules in the target tissue or cell. EPR intrinsically allows for the quantification of a labeled compound and is sensitive to polarity, pH, and viscosity of the microenvironment[27,28]. Up to now, biomolecules were singly labeled to use the read-out from either technique, but individual labeling will lead to unequal properties like charge, mass, and hydrophilicity. By extension, discrepancies between findings of both methods are inevitable.

So, the aim is to develop a novel platform for dual-labeled compounds which enables simultaneous fluorescence and EPR measurements. Not only to compare results but also to benefit from the synergy between FLIM and EPR in drug delivery research.

2 Fundamentals

2.1 Fluorescence

The emission of a photon during the relaxation of an electron from an excited into its ground state is called fluorescence. The exact position of the excited states in the energy landscape of outer electrons may shift upon interaction of any molecule with its environment, rendering the fluorescence emission often sensitive to the local environment of the fluorophore. This fact makes fluorescence spectroscopy and microscopy an essential tool in biophysical research.

Figure 2-1 shows the Jablonski diagram, a depiction of the electronic and vibronic states of a fluorescent molecule's electrons and possible transitions between those states. After absorption of a photon, the electron gets excited into the S_1 state or possibly even higher singlet states. Although it might arrive in a higher vibronic state, the transition into the vibronic ground state is achieved by internal conversion, i.e. collisions with solvent molecules. The rate of internal conversion is proportional to the density of states, so at room temperature and in solution it is usually very fast in states higher than S_1 (~10^{-13}-13^{-11} s). This is the reason why the vibronic ground state of the S_1

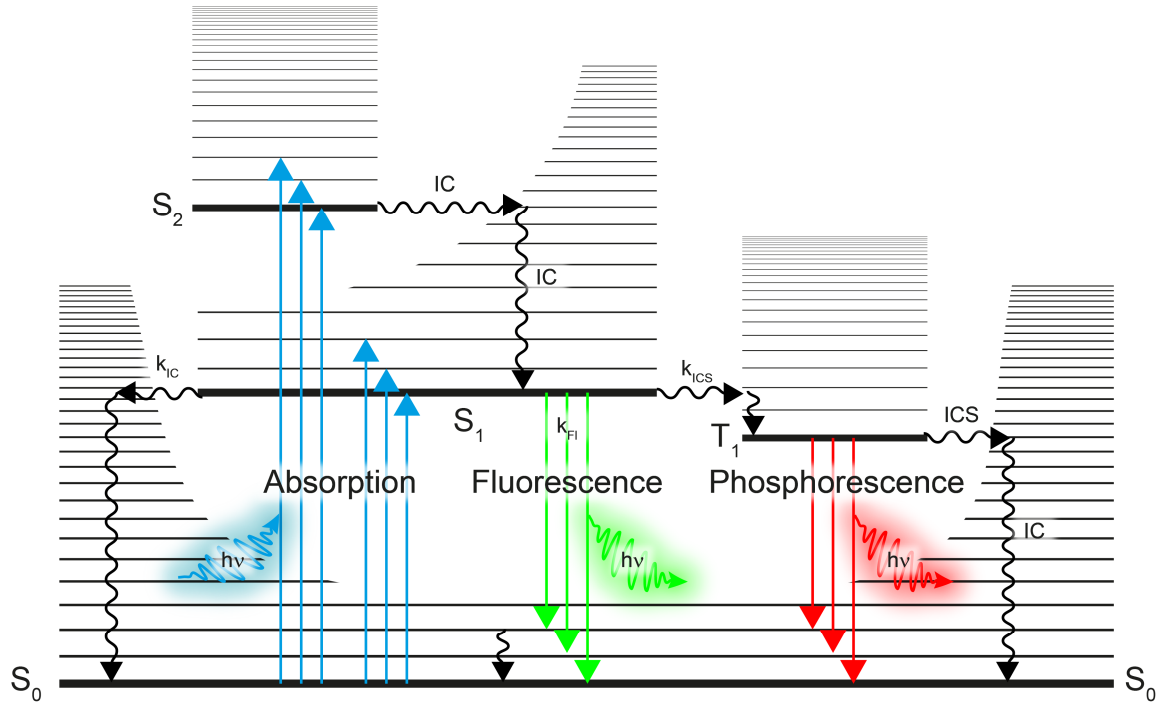

Figure 2-1. Jablonski diagram, illustration of the relative positions of electronic states and possible transitions between them. S_0 is the electronic singlet ground state, S_1 is the first excited singlet state, T_1 the equivalent triplet state. Straight arrows indicate absorption or emission of a photon $h\nu$, wavy arrows are radiationless transitions i.e. internal conversion (IC), inter system crossing (ISC) and vibrational/rotational relaxation with the associated transition rates k_{Fl}, k_{IC}, and k_{ICS} which depopulate the S_1 state.

can be considered the starting point for almost every fluorescent emission, which happens much slower (~10^{-12}-10^{-8} s). This is known as Kasha's rule. Vertical transitions in the Jablonski diagram are subject to the Born-Oppenheimer approximations. Hence, absorption and emission spectra are well described by the Franck-Condon principle. Arrow length of the vertical transitions are proportional to photon energy. The fast vibronic relaxation leads to a red shifted emission spectrum, the so-called Stokes-shift. From the S_1state, there is also the possibility of inter system crossing into an excited triplet state T_1. A direct transition into the ground state S_0 is forbidden by the selection rule $\Delta S = 0$. In practice though, this results in a severely delayed transition under the emission of a phosphorescent photon, which can take microseconds to minutes.

2.1.1 Time-resolved fluorescence and time correlated single photon counting (TCSPC)

The depopulation of the excited electronic state is a statistical process. The mean time an electron stays in the excited state is called excited state lifetime or fluorescence lifetime and is a characteristic for any given fluorophore while being highly sensitive to the local environment. To describe the evolution of the fluorescence intensity over time, consider an ensemble of molecules $[A]$ brought into the excited state $[A^*]$ by an intense delta-shaped photon pulse at t=0. From the excited S_1 state a molecule returns to the ground state S_0 either by emitting a fluorescence photon or via non-radiative relaxation processes like internal conversion (Figure 2-1). The associated transition rates are k_{Fl} and k_{nr} respectively. So, after the time interval dt, the change in concentration of molecules in the excited state is given by:

$$-\frac{d[A^*]}{dt} = (k_{Fl} + k_{nr})[A^*] \tag{1}$$

This differential equation is solved with an exponential ansatz for $[A^*](t)$:

$$[A^*](t) = [A^*]_{t=0} e^{-t/\tau} \tag{2}$$

with the fluorescence lifetime τ:

$$\tau = \frac{1}{k_r + k_{nr}} \tag{3}$$

The fluorescence intensity I_{Fl} is defined as photons emitted per time from a sample solution. Given that k_{Fl} is the rate at which excited molecules return into the ground state under emission of a photon, the fluorescence intensity is proportional to the concentration of excited molecules $[A^*](t)$ and the transition rate k_{Fl} at any given time:

$$I_{Fl}(t) = k_{Fl}[A^*](t) = k_{Fl}[A^*]_0 e^{-t/\tau} \tag{4}$$

where $k_{Fl}[A^*]_0 = \alpha$ is constant. Under homogeneous conditions for a single fluorophore, this would yield a monoexponential decay of the fluorescence intensity. As soon as different micro-environments are present in a sample volume, different sub-populations of the fluorophore with distinct $k_{Fl,i}$ emerge. Since these rates are generally not coupled, the fluorescence intensity of the ensemble can be modelled as a sum of exponentials:

$$I(t) = \sum_i^n \alpha_i \, e^{-t/\tau_i} \tag{5}$$

A population weighted mean lifetime can be calculated from:

$$\bar{\tau}_{pop} = \sum_i^n \beta_i \, \tau_i \tag{6}$$

using the fractional amplitudes β_i:

$$\beta_i = \frac{\alpha_i \tau_i}{\sum_i^n \alpha_i \tau_i}. \tag{7}$$

Due to the fast timescale of the fluorescence decay on the ps to ns range, a special measuring technique called time correlated single photon counting (TCSPC) is often required to differentiate even subtle changes in a fluorophores decay. TCSPC is based on repeated pulsed excitation of a fluorescent ensemble and detection of single photons of the fluorescence emission. The time between the excitation pulse and the arrival time of the first photon registered by the detector is precisely measured and the delay time then sorted into a histogram. With repeated measurements of delay times and increasing photon statistic, this histogram accurately reproduces the fluorescence decay curve of the fluorophore. A detailed description of the technical realization of the TCSCP setup is given in chapter 3.3[29].

2.1.2 Quenching, energy transfer, and photoisomerization

All processes which reduce the fluorescence intensity of a sample are called fluorescence quenching. In particular, this includes processes which either prohibit the formation of the excited state or dissipate the energy of the excited state without the emission of a photon. This divides the quenching processes into static and dynamic quenching[30,31]. In static quenching, the quencher forms a complex with the fluorophore before excitation. This complex has its own distinct properties and might have a shifted absorption spectrum or does not emit a photon during the transition into the ground state after photon absorption. In dynamic quenching, the energy of the absorbed photon is transferred to the quenching during the lifetime of the excited state. This can either be facilitated by exchanging the excited electron, called Dexter electron transfer, or via

fluorescence resonant energy transfer (FRET), which is a dipole-dipole interaction between the fluorophore and the quencher and which permits radiationless energy transfer. All quenching processes are dependent on quencher concentration $[Q]$ and the relation between $[Q]$ and the reduction of fluorescence intensity and fluorescence lifetime are governed by the Stern-Volmer equation[32]. In the static case, every fluorescence photon is coming from a fluorophore not in complex with the quencher. Hence, its fluorescence lifetime is not changed but the fluorescence intensity of the ensemble is reduced because of the presence of non-fluorescent complexes:

$$\frac{I_0}{I} = 1 + K_S[Q] \qquad \text{and} \qquad \frac{\tau_0}{\tau} = 1 \tag{8}$$

where I_0 and I are the unquenched and quenched fluorescence intensity, τ_0 and τ are the respective fluorescence lifetimes, and K_S is the quencher specific Stern-Volmer quenching constant for static quenching. In the dynamic case, also the fluorescence lifetime is reduce as the energy transfer to the quencher poses an additional non-radiative transition rate into the ground state k_q (see eq. (3)):

$$\frac{I_0}{I} = 1 + \tau_0 k_q[Q] \qquad \text{and} \qquad \frac{\tau_0}{\tau} = 1 + \tau_0 k_q[Q] \tag{9}$$

Finally, the quantum yield expresses the ratio of absorbed photons to emitted photons:

$$\varphi = \frac{k_r}{k_r + k_{nr}} \tag{10}$$

2.1.2.1 Fluorescent molecular rotors

Fluorophores in the family of the molecular rotors, as for example many cyanine dyes, have the ability to undergo photoisomerization[33-35], a process also resulting in reduced quantum yield. They have an intramolecular axis which facilitates a twisting or rotating motion (Figure 2-2A). In the case of Indocarbocyanine (ICC) or Cy3, the methine linker between the two indole groups adopts an all-t*rans* conformation in the S_0 state as it constitutes the energetically lowest state (Figure 2-2B). After absorption of a photon and transition into the S_1 state, a conversion into a twisted or mono-*cis* configuration can occur. Hence, the depopulation of the S_1 state is driven by three competing processes: internal conversion k_{ic}, fluorescence k_r, and the route involving photoisomerization k_{PI} and further non-radiative decay of the excited state, either directly into the all-*trans* state or via the meta-stable mono-*cis* state followed by an first-order back reaction into the all-*trans* state. The contribution of photoisomerization is dependent on solvent viscosity, molecular weight,

temperature, and steric hindrance of the rotation. In low viscosity solvents, photoisomerization has a very high efficiency leading to a fast depopulation of the S_1 state and fluorescence lifetimes for ICC below 0.2 ns (Figure 2-2C).

The correlation of ICCs excited state lifetime and solvent viscosity can be investigated by time-resolved fluorescence spectroscopy measurements of ICC in solutions of varying in viscosity. Viscosity can be adjusted on the one hand with sucrose-water mixtures ranging from 0-70% (w/w) sucrose, and varying temperature on the other hand, in order to span a calibration range of 1-2000 mPa s.

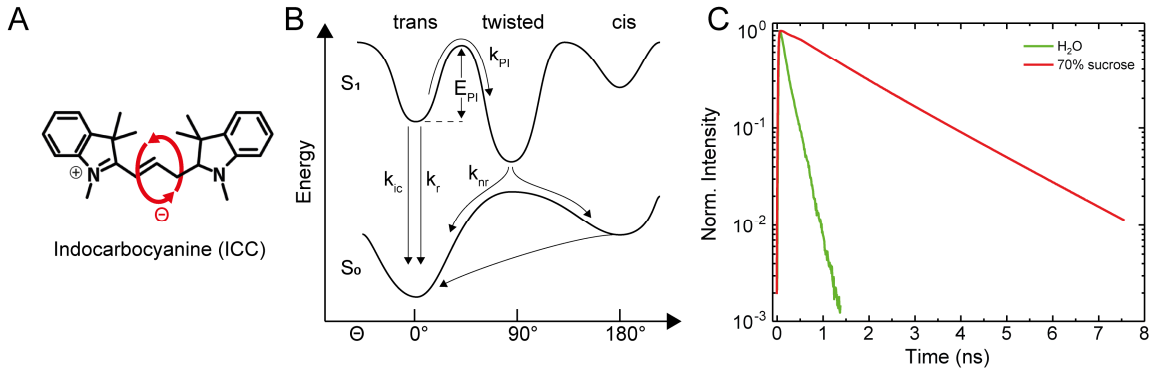

Figure 2-2. Photoisomerization of ICC. (A) Structural formula of ICC (obtained from Mivenion GmbH, see chapter 3: Materials and Methods) with indicated axis of rotation. (B) Energy diagram of ICC's photoisomerization process. θ indicates the torsion angle of the polymethine chain between the two indoles. (C) Fluorescence decay curves of ICC in a low (green, $\bar{\tau} = 0.14\ ns$) and a high viscosity (red, $\bar{\tau} = 1.33\ ns$) environment.

Resulting fluorescence decays are fitted with a sum of three exponentials (eq. (5)) and the population weighted mean fluorescence lifetime $\bar{\tau}_{pop}$ is calculated according to eq. (6). Viscosity is either measured in a rotational viscosimeter (see 3.9), or taken from literature[36,37]. Viscosity dependent mean fluorescence lifetimes are further analyzed using the Förster-Hoffmann equation[38]:

$$\varphi_f = C\eta^{\alpha}, \tag{11}$$

where C and α are empirical constants specific for each molecular rotor. Using eq. (3) and (10), this gives an expression for viscosity dependent fluorescence lifetime:

$$\tau = \left(\frac{C}{k_r}\right)\eta^{\alpha} \tag{12}$$

$$\log\tau = \log\left(\frac{C}{k_r}\right) + \log\eta^{\alpha} = \beta + \alpha \cdot \log\eta, \tag{13}$$

presenting a linear relationship in a log-log-plot between lifetime τ and viscosity η with slope α. It is possible for the fluorescence lifetime relation to viscosity to be temperature dependent. This behavior can be modelled by introducing an activation energy E_a of the isomerization[35]:

$$k_{rot} = A(\eta)e^{-\frac{E_a}{k_B T}} \tag{14}$$

Here $A(\eta)$ is the viscosity-dependent amplitude, k_B is Boltzmann's constant and T the temperature. Using the Förster-Hoffmann equation (eq. (11)), eq. (14) can be rewritten as:

$$k_{rot} = \frac{1}{C\eta^{\alpha} + \frac{1}{A_{max}}} e^{-\frac{E_a}{k_B T}} \tag{15}$$

and finally, using $\tau = (k_{rot}(\eta, T) + k_r + k_x)^{-1}$, yields:

$$\tau = \left(\frac{1}{C\eta^{\alpha} + \frac{1}{A_{max}}} \cdot e^{-\frac{E_a}{k_B T}} + k_r + k_x \right)^{-1} \tag{16}$$

$1/A_{max}$ is a constant, acknowledging the fact that τ will not got to zero for zero viscosity. k_r is the radiative (i.e. fluorescence) rate and k_x are all other non-radiative rates from the excited into the ground state. Eq. (16) will be used as a global fitting function for mean fluorescence lifetime $\overline{\tau}_{pop}(\eta, T)$.

2.1.2.2 Fluorescence quenching by unpaired electrons

Besides the dipole-dipole interaction in FRET or static ground state quenching, there is also the possibility for the interaction of a fluorophore with a paramagnetic species, such as oxygen or nitroxides, during the excited state lifetime. This interaction does not require optical overlap and is short ranged (5-7 Å[39]) and is thus considered collisional. The mechanism is most likely based on electron transfer between the oxide and the fluorophore[40,41]. Spin-orbit coupling then leads to rapid intersystem crossing from the excited state followed by non-radiative energy loss from the triplet state. The dependency of efficient quenching on the oxide-fluorophore distance was recognized as a viable tool to measure distances in biological systems[42] and has since developed into one of the most frequent applications of spin-label quenching[40], known as the parallax method.

2.1.2.3 Parallax method

The parallax method to determine the axial distance between a fluorophore and a nitroxide label was first described by Chattopadhyay and London[43]. Following Chattopadhyay and London, we used

the Perrin equation, which is used to analyze static quenching of randomly distributed fluorophores, and applied it to quenching analysis in membranes. For this application, assume randomly distributed fluorophores and quenchers on a plane and use a hard sphere approach for fluorophore-quencher interaction. In that case the Perrin equation yields:

$$\frac{F}{F_0} = e^{-\left(\int_0^{R_c} 2\pi r\, dr\right)C} = e^{-\pi R_c^2 C}, \tag{17}$$

where F/F_0 is the ratio of unquenched fluorescence and fluorescence intensity in presence of the quencher, C is the concentration of quencher molecules per unit area and R_c the critical radius of the hard sphere, so πR_c^2 describes a circle around the quencher within which the fluorophore is fully quenched. To determine intercalation depth into the membrane, it is useful to define z as the minimal vertical distance between fluorophore and quencher, so it will become the lower boundary of the integral in eq. (17). So hard-sphere quenching is then given by:

$$\frac{F}{F_0} = e^{-\pi R_c + \pi z^2 C} \qquad (z \le R_c) \tag{18}$$

$$\frac{F}{F_0} = 1 \qquad (z > R_c) \tag{19}$$

In the two-dimensional case, where lateral distance x is also included eq. (18) is extended to:

$$\frac{F}{F_0} = e^{-\pi R_c + \pi z^2 C + \pi x^2 C} \qquad \left(\sqrt{z^2 + x^2} \le R_c\right) \tag{20}$$

To eliminate the requirement of knowing anything about R_c and to ignore the fact that there might be restrictions on the lateral distance x of fluorophore and spin-label, it is instructive to consider a set of two or more quenching experiments, i.e. quenching by spin-labels at different positions in the carbon chain of the fatty acids of phospholipids (Figure 2-3). Ratio of both experiments are given by:

$$\frac{F_1/F_0}{F_2/F_0} = \frac{F_1}{F_2} = \frac{e^{-\pi R_c + \pi z_{1F}^2 C + \pi x^2 C}}{e^{-\pi R_c + \pi z_{2F}^2 C + \pi x^2 C}} \tag{21}$$

where the subscripts 1 and 2 denote the shallower and deeper quencher respectively. Accordingly, F_1 is the fluorescence in presence of quencher 1, F_2 in presence of quencher 2, z_{1F} the distance between fluorophore and quencher 1, and z_{2F} the distance between fluorophore and quencher 2. Now all terms dependent on R_c or x cancel out. Introducing L_{21} as the distance between both

quenchers, so $z_{2F} = L_{21} + z_{1F}$, and the subscript c denoting distances from the bilayer center, eq. (21) can be rearranged to:

$$z_{cF} = \left(\frac{1}{-\pi C} \ln \frac{F_1}{F_2} - L_{21}^2\right) / 2L_{21} + L_{c1} \tag{22}$$

Where L_{c1} can be generally deduced from the labeling position of the spin-label. z_{cF} is now the measure for incorporation depth of ICC into the lipid bilayer and is only dependent on the 2 fluorescence intensities F_1 and F_2, and the quencher concentration C in molar fraction of quencher lipid in total lipid per 70 Å² (usual surface area per phospholipid). We assume a total thickness of 30 Å for the hydrocarbon region and 5 Å for the polar head groups based on structural data[44].

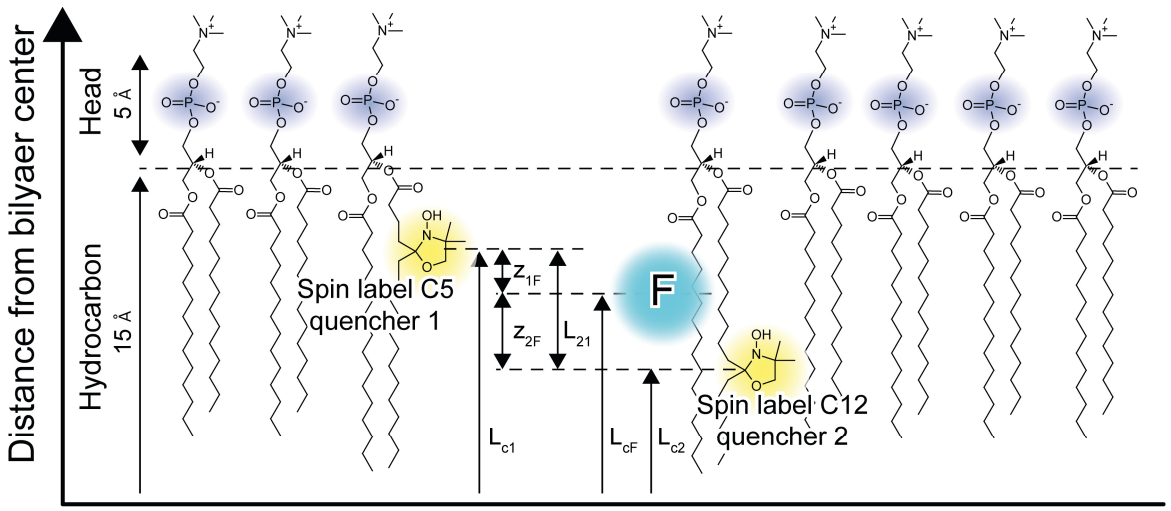

Figure 2-3. Schematic of a half lipid bilayer illustrating the incorporation of the fluorophore (F) in relation to the labelling positions of the spin-labeled phosphocholins which act as quenchers for the fluorescence. Indicated are also all distances necessary for the calculation of the insertion depth of the fluorophore. Thickness of hydrocarbon and polar head region are taken from [44].

2.2 Biological tissue and its relation to physics

2.2.1 Internal tissue barrier: mucus/mucosa

The specialized epithelium lining the gastrointestinal and respiratory tract as well as all other wet barrier surfaces in the body is called mucosa. It is made up of a single cell layer, consisting of several different cell types with unique functions and tasks. The mucosa usually is protected by a mucus layer, which lubricates the surface thereby lowering mechanical stress on the epithelium, and is able to trap and transport debris as well as bacteria away from the cellular layer. As such, it plays an important role in the innate immune response as it also often also contains a plethora of antimicrobial peptides[45]. Mucins, the mucus' main constituent, have many inherent properties which can be controlled by the host and which allows the mucus layer to meet the demanding and multilateral exigencies posed on it[46].

2.2.1.1 The mucus layer and its importance for the exchange with the environment

Mucins are glycoproteins which have at least 50% and up to 80% of their dry mass made up of O-glycans (Figure 2-4). Different types of mucins reach a molecular weight of up to 40 MDa and have a diameter of 3-10 nm[47]. Most extensive domains in mucins are the PTS domains, named after the prevalence of the amino acids proline threonine and serine which are heavily decorated with O-glycans. These polysaccharide sidechains bind vast amount of water and give mucins gel-like properties, meaning that its structural properties are not defined by the solvent but rather by the mucins protein backbone and its crosslinking. Hence, mucins can be imagined as an extended, voluminous rods with central protein cores, interlinked and entangled among each other, forming a 3D surface which is able to interact with cells, microorganisms, and other agents. Abundancy of sialic acids, an acidic sugar, and sulfates in the glycans grant mucins a strong negative surface charge. Generally, one distinguishes between transmembrane and gel-forming mucins[48,49]. Their nomenclature is a bit bewildering as their name holds no information over their form, function or location in the body. Transmembrane mucins are characterized by a single membrane spanning domain at the C-terminus which can be involved in cell signaling. Most important transmembrane mucins are MUC3, which is found throughout the intestinal tract but mainly in the duodenum[50],

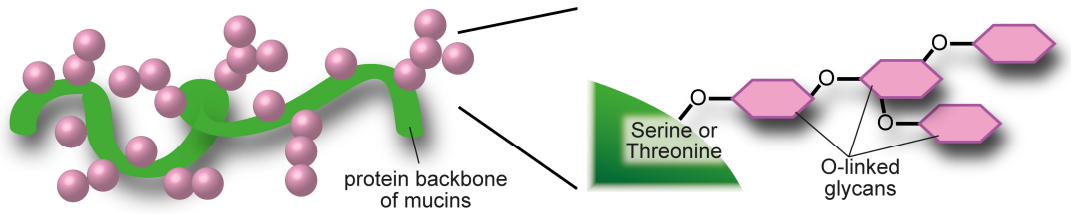

Figure 2-4. O-linked glycosylation of the mucin protein backbone. Using the oxygen of serine or threonine residues to attach sugar moieties.

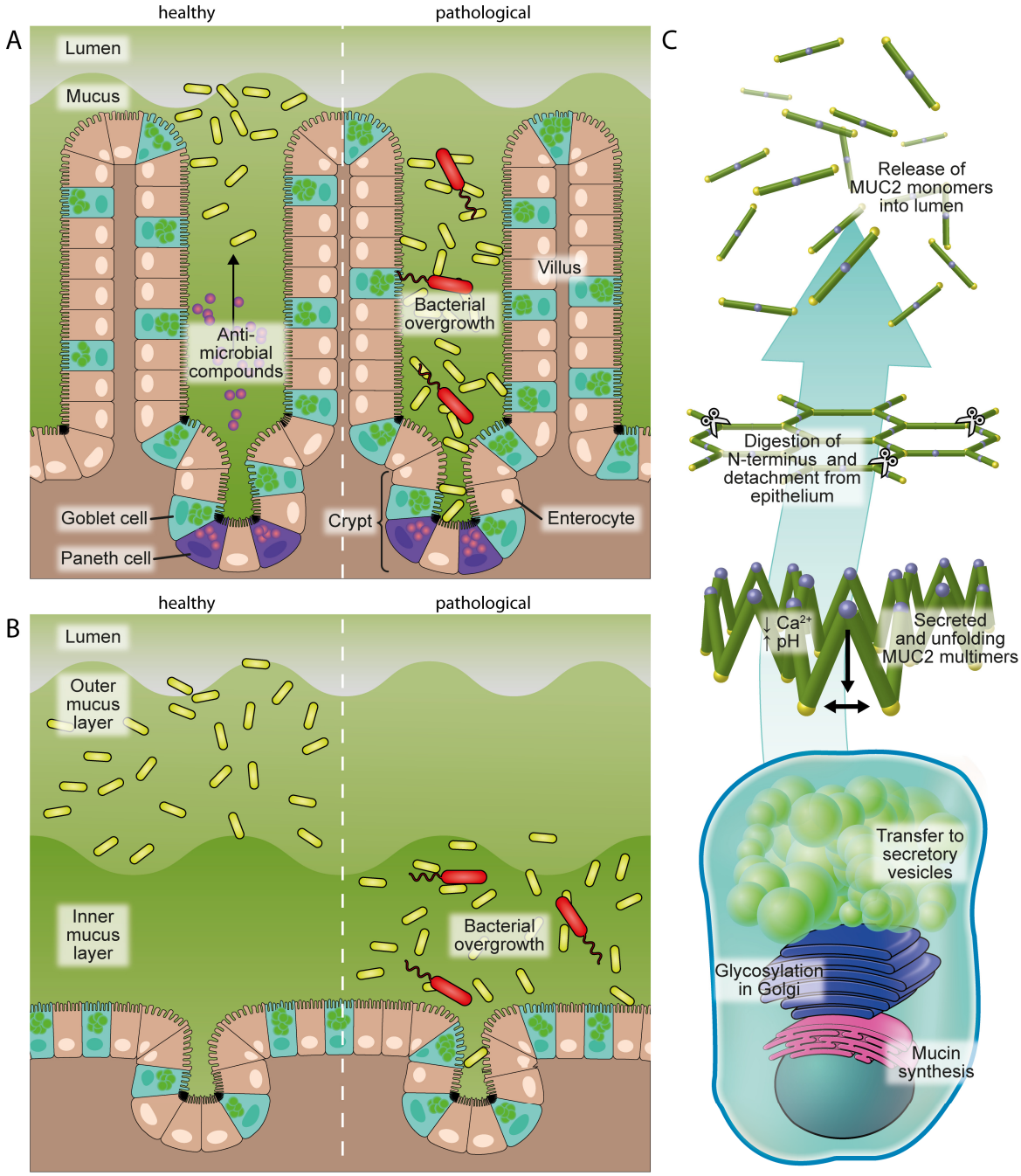

Figure 2-5. Mucosa physiology and mucin secretion. Cellular composition and structure of the mucosal epithelium in small intestine (A) and colon (B) and its interplay with healthy and pathological bacterial population. (C) Schematic of mucin synthesis, posttranslational modification, and secretion by goblet cells.

MUC4 and MUC 12, commonly found in the colon[51], MUC13, also present in the entire intestine, and MUC 17, mainly found in the small intestine and duodenum but also in the transverse colon[50]. While aforementioned mucins are always present in a healthy human, MUC1 and MUC16 have been shown to be upregulated during infection or in cancer[52,53]. Apart from MUC13, all transmembrane mucins are eventually cleaved from the transmembrane domain at the apical side.

They stay associated to the cell surface but may be removed by mechanical forces. MUC3, 12, and 17 are the largest membrane bound mucins with more than 4000 amino acids. The form the so-called glycocalyx, which reach up to 1 µm into the lumen and protect the underlying epithelial cells. Most prominent member in the gel-forming mucin family are MUC2, MUC5B, MUC5AC, and MUC6. The main gel-forming mucin of the stomach and intestines is MUC2[54]. MUC5B is predominantly found in saliva and lungs but in low levels also in cervical mucus and the human colon[55]. MUC6 lines the stomach and duodenum[54]. And while MUC5AC is common in the respiratory tract, it is only present in the intestine during infection[56].

Mucins are produced by specialized epithelial cells (Figure 2-5). While enterocytes produce predominantly transmembrane mucins and only in comparatively small amounts, the main mucus secreting cells in the intestine are goblet cells. They reside mainly in the crypts of the small intestine but are also abundant in the colon and produce predominantly MUC2. Inside the goblet cells, the mucins' protein backbone is glycosylated in the Golgi apparatus and then transferred into secretory vesicles. Tight packing of the glycoproteins inside of these vesicles is achieved by multimerization via intermolecular disulfide bonds of cysteine rich domains of the mucins. MUC2 forms trimeric linkages[46] while MUC5B is connected in linear arrangements[57]. Multimers of other mucins are suspected but their nature is not clear up until this point. When secreted at a basal rate, mucin containing vesicles fuse with the apical cell membrane, releasing the mucins into the lumen. The expelled tightly packed granules of mucins inflate upon water binding into flat sheets, interacting with previously formed ones, initially attached to the epithelium but eventually cleaved by the protease meprin-β[58]. After mechanical or chemical stimulation, it is also possible for a process to happen called compound exocytosis, where most of the mucus granulae are fusing, emptying almost the entire cell interior [59]. Inflammation has been observed to trigger MUC2 release as well[60]. This coordinated mucus release is thought to expel pathogens and protect the intestinal crypts from bacterial overgrowth.

In the small intestine, the mucus forms a single continuous but porous layer, easily removable by mechanical force. It is partly permeable which is necessary for nutrient absorption but makes it also penetrable for bacteria[61]. Hence, pathogens need to be kept away from epithelial cells by antibacterial mediators like the antibody immunoglobulin A (IgA) and defensins, antimicrobial proteins, produced by Paneth cells and released into the lumen alongside with the mucus. Thus IgA concentration forms a gradient with mucus depth because of its relatively slow diffusion through the mucus layer[45]. In the small intestine, the MUC2 detachment is almost instant, facilitating a smoother transport during peristalsis, and also clearing cellular debris and bacteria in the process. In the colon on the other hand, the release mucins form a double layer with the inner layer thick

and firmly attached to the epithelium. This dense layer of stratified MUC2 multimers protects the mucosa lining the colon from mechanical stress during slow propulsion of firm fecal matter and thereby avoids prolonged exposure to microorganisms in the lumen. The inner mucus layer is eventually converted into a less dense outer layer by endogenous proteases to provide lubrication[62]. Hence, this turnover requires constant and quick renewal of the mucus layer in order to maintain homeostasis. In mice, 50 µm of inner mucus layer is regenerated every hour[63]. Mucus composition varies a lot between species. For example, the cecum of mice has fermentation function and bacteria have been found to be in direct contact to the local epithelium but are separated by an intact mucus layer in the colon[61]. In contrast, in humans, the mucus protects the epithelium throughout the large intestine[64].

2.2.1.2 Viscoelastic properties of mucus and mucins and challenges for their investigation

Mucus is a selective barrier, meant to enable gas exchange and nutrient absorption while hindering pathogen invasion, providing lubrication, and protecting the epithelium from mechanical shear stress. These tasks pose different requirements on the biophysical properties of the mucus across vastly different length scales. Hence, it is instructive to differentiate between the macroscale and the micro-/nanaoscale. In this context, nanoviscosity should be thought of as the viscosity encountered by a nanometer sized probe. Understanding these properties, i.e. viscosity (η) and elasticity encountered by agents of different sizes and mucus interactions, is of utmost importance for the understanding of nanoparticulate drug delivery systems. At the macroscale, mucus deviates from the constant viscosity of a newtonian fluid ($\eta = const$) but is better described by a non-newtonian gel, meaning its viscosity is dependent on shear stress (σ) and rate ($\dot{\gamma}$). At the microscale on the other hand, mucus tends to present itself as a low viscosity fluid. Here, shear stress σ is defined as:

$$\sigma = \eta\dot{\gamma}, \tag{23}$$

with γ being the shear strain or deformation and $\dot{\gamma}$ the shear rate. Furthermore, the shear modulus G can be gathered from Hook's law, as the ratio of shear stress to shear strain:

$$G = \sigma/\gamma, \tag{24}$$

which is complex in viscoelastic fluids:

$$G^* = G' + iG''. \tag{25}$$

Here, the storage modulus G' and the loss modulus G'' describe the elastic (stiffness) and the viscous (resistance to flow) properties of viscoelastic fluids, respectively. Hence, the G'-value can be imagined as a measure for energy stored by the material during deformation, while the G''-value

represents energy dissipation as heat during the shear process. Note that the shear modulus also often is dependent on shear frequency. The diffusion of spherical particles with radius r through a viscous medium can be described using its diffusion coefficient D in the Stokes-Einstein-equation:

$$D = \frac{k_B T}{6\pi * \eta * r} \tag{26}$$

In any case, the viscoelastic properties originate in a heterogenous mucus composition and the interplay of its various constituents. As stated earlier, mucins are the main component of mucus with a dry mass fraction of 2-5%. Mucins with their hydrophilic sidechains are also responsible for the high water content in mucus (90-98%)[65-70]. In addition, salt ions, which contribute up to 1% of the mass in mucus[71], are directly responsible for swelling and shrinkage of the mucus because water content is directly proportional to salt concentration. Lipids and DNA is also found in the mucus and likely originates in shed cells from the mucosal epithelium. Although only contributing with 1-2%[71] and 0.02%[71], to the mass of the mucus respectively, their contribution to mucus viscosity shouldn't be overlooked. An increase of DNA content to 0.5-1.5% for example has been linked in part to a 10-100 fold viscosity increase in cystic fibrosis[72]. Also, DNAse has been shown to reduce viscosity better than typical mucolytic agents like n-acetyl cysteine in some cases[73].

Under low shear stress, mucus behaves like an elastic solid characterized by a high storage module (G'). With increasing shear rate its behavior shifts to more of a viscous liquid where viscosity increases with second or third power of mucin concentration[74]. This shear thinning results from the alignment of the mucin polymer network, facilitating a flow with much less resistance. This effect is desirable for example during peristalsis in the intestine. The initially lost elasticity under high shear rates is quickly recovered a soon as the shear stress is removed, usually within seconds to minutes[75]. This suggests that much of mucus' macroscopic viscoelastic properties relies on reversable linkage and physical entanglement[76] of mucins and DNA strands in addition to the covalent disulfide bonds of the cysteine rich domains of mucins[77]. Also antibodies present in the mucus have an influence on viscosity and serve as restructuring molecules[78]. Their fragment crystallizable region (Fc-region) has been shown to interact with mucins, probably in order to capture pathogens in the mucin network[79], immobilizing them and facilitate their eventual expulsion. Additional contribution of free-floating cells and cellular debris to the viscoelastic properties of mucus is not fully understood. They probably are the origin of many lipids, DNA, and proteins, in particular actin filaments, found in the mucus which definitely influence viscoelasticity but as to what extend adhesive interactions between the cell surface and mucins play a role beyond the afore mentioned mechanism is next to impossible to investigate in isolation.

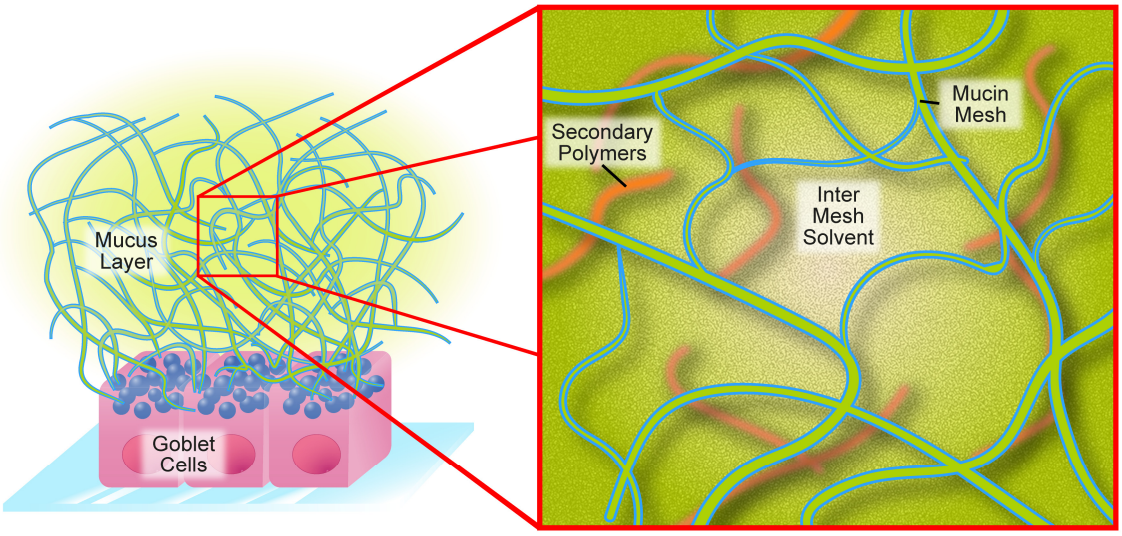

Figure 2-6. Structures of mucus that affect viscosity in the mucus layer.

On the microscopic and nanoscopic scale, mucus is very heterogeneous resulting from its diverse composition (Figure 2-6). For an integrated picture, steric hindrance by and interaction with the mucin mesh has to be considered as well as micro-domains in between the mesh, usually characterized by the low viscosity of the solvent water. Therefore, sensor size in comparison to mucins mesh size, typically 100-400 nm[80], has to be evaluated critically as it will influence what quality and quantity of the mucus will be probed and hence be pivotal to valid conclusions. For example, small viruses (38-55 nm) have been found to diffuse in cervical mucus as fast as in water while larger viruses (180 nm) experienced a 100-1000 fold decrease of diffusivity[79]. On the mesoscopic length scales, encountered by particles with diameters comparable to mucin mesh size, mucoadhesion seem to have the largest contribution to particle diffusion. Low molecular weight polyethylene glycol coating can greatly reduce mucoadhesion and hence mucoinert polymeric particles with diameters of 200 and 500 nm experienced only slight reduction of diffusion in human mucus compared to water[81]. In contrast, particles of 1000 nm with the same polymeric coating did not share the same high diffusivity anymore and instead encountered substantial steric hindrance by the mucin mesh, greatly reducing transport.

When investigating viscoelastic moduli of mucus, one is faced with a multitude of obstacles. First one being acquiring adequate sample volumes for basic characterization. Depending on species and tissue site, even 20 µl can be challenging to harvest. Often mucus samples are contaminated by saliva or feces and in addition, the mechanical force applied by a cell scraper for mucus harvesting might induce unphysiological mucus secretion and lead to unrepresentative results. Substantial inter- and intrasubject variability in human and animal models make it hard to assess the appropriateness of a given model[82] but it is generally assumed that similarity in organ size is a good

indicator for similar mucus physiology[83]. Hence, for investigating human physiology, porcine mucus would be a natural choice as their bulk viscosity have already been shown to be comparable and mucus of both species exhibit structural similarities[84-86]. Furthermore, purified porcine colonic mucin had the same rheological properties as *in vivo* secretion[87]. Hence, isolated porcine mucins will be basis for the later presented studies as it is commercially available and sufficiently representative for the human intestine.

2.2.1.3 Bacterial interplay with mucus viscosity in health and disease

Mucus poses a physical diffusion barrier for most bacteria and pathogens. In addition, IgA is secreted in high concentration in duodenum, ileum and to some extend also in the colon[88,89]. It binds to the microorganisms and viruses, aggregates them and reduce their mobility and diffusion rates. In the colon, IgA is not as necessary to separate bacteria from the epithelium as the inner thick mucus layer is sufficiently capable for this task. Furthermore, Paneth cells produce defensins which mix at the openings of the crypts with the MUC2 produced by goblet cells and contribute to the innate immune system.

In the small intestine, one finds very high bacterial activity. The mucus layer here is partially penetrable, so it is intermixed with bacteria. In the healthy small intestine, they stay in a planktonic an motile state rather than forming biofilms on the underlaying cell surface[90]. They have been observed to use proteolytic enzymes in order to decrease local mucus viscosity and facilitate their motion[91]. Microbiota composition is balanced by interspecies competition. Food choices of the host select for different bacterial strands[92] and even varying glycosylation of the secreted mucins might provide nutrients for bacteria[93] and as such select for an individual microbiome[94]. Finally bacteriophages which adhere to the mucus[95] and most of which are specific for only one bacterial species, have a drastic influence on microbiome composition. Therefore, in the small intestine, one finds a less diverse microbiota as for example in the colon[96], which is the consequence of a highly competitive environment, which is also much more susceptible to exterior influences like host provided nutrient sources. Under germ free conditions, it has been shown that it is difficult to clear the built-up mucus layer. Left untreated, the intervilli space eventually becomes colonized by biofilm forming pathogenic bacteria, leading to infection. This shows that moveable mucus is imperative for homeostasis in the small intestine[97]. In the colon, the mucus is typically impenetrable to bacteria but becomes more porous in germ-free mice[97]. During recolonization, increased mucus secretion is observed in response to the stimulus generated by the presence of bacteria and full recovery of the 2 fully functional mucus layers is achieved after 5 weeks[97,98]. The shift in bacterial composition takes place first in the small intestine and soon after in the colon, implying an important role of the small intestine in pre-selecting bacteria colonies. Antibiotics obviously have

severe effects on the intestinal microbiota but earlier studies show that they also lead to physiological changes of the mucosal epithelium itself[99]. They have been shown to increase the cell-associated antigen passage (GAP) of goblet cells to the subjacent lamina propria and local dendritic cells, promoting inflammation[100]. The effect of antibiotics on mucus layer thickness and viscosity though is very unpredictable and often depends on the specific drug in combination with the test specimen. Results range from thinning of the colonic mucus over having no impact[101] to increasing mucus layer thickness[97].

2.2.2 External tissue barrier: skin

The skin is the largest organ in the human, covering about 2 m². It is the outermost layer in all vertebrates and with that needs to protect against a plethora of environmental hazards like ultraviolet light, mechanical insult, dangerous chemicals as well as pathogenic microorganisms. It also regulates thermal insulation and transdermal water loss. As a first line of defense, it also hosts several immunocompetent cells as well as components of the innate immune response. In general, every function of the skin – besides vitamin D metabolism – can be considered protective to some degree. And this protection is achieved by an intricate interplay of physical, biochemical as well as immunological barriers.

2.2.2.1 Morphology

The skin can be divided into three layers, hypodermis, dermis and epidermis with further subdivision of the latter two (Figure 2-7). The hypodermis characterized by adipose tissue lending the skin its thermal insulation and shock absorbance capabilities. Fibrous collagen and elastin bands produced by fibroblast anchor the hypodermis to deep fascia and the overlaying dermis. The dermis is about 1-2 mm thick and is divided into the *stratum reticulare* and the *stratum papillare* (Figure 2-7A). In the *stratum reticulare*, fibers mainly composed from elastin and collagen type III form an extracellular matrix which provide stability and grant the skin its elastic properties. Several immunocompetent cells like dendritic cells, mast cells and macrophages are located in the dermis in anticipation of pathogens entering the skin. Merkel cells and nociceptors constitute the sensory nerve component in the skin, responsible for sensation of touch, temperature and pain. The dermis is also rich in vasculature, important for the nutrient supply of the here residing hair follicles, various glands as well as for the overlaying epidermis. The *stratum papillare* is characterized by looser connective tissue and forms excrescences towards the epidermis filled with capillary blood vessels, which increases the boundary surface area necessary for diffusion driven nutrient transport into the outermost skin layers. Lymphatic vessels here ensure the clearance of cellular waste in the metabolically very active skin layers and facilitate the recruitment of further lymphocytes to inflammation sites if needed. The basal membrane separates the epidermis from the dermis. It anchors the first cell layer of the epidermis to the subsiding connective tissue of the dermis. The epidermis is the outermost layer of the skin and provides physical as well as biochemical protection against the exterior. Depending on body site and exposure it is between 50 and 100 µm thick but can extend up to 600 µm in areas with particularly high mechanical stress like the palms and foot soles[102-104]. Besides melanocytes, responsible for the protection against UV-radiation, and dendritic cells, the keratinocytes are by far the most prominent cell type of the epidermis, comprising about

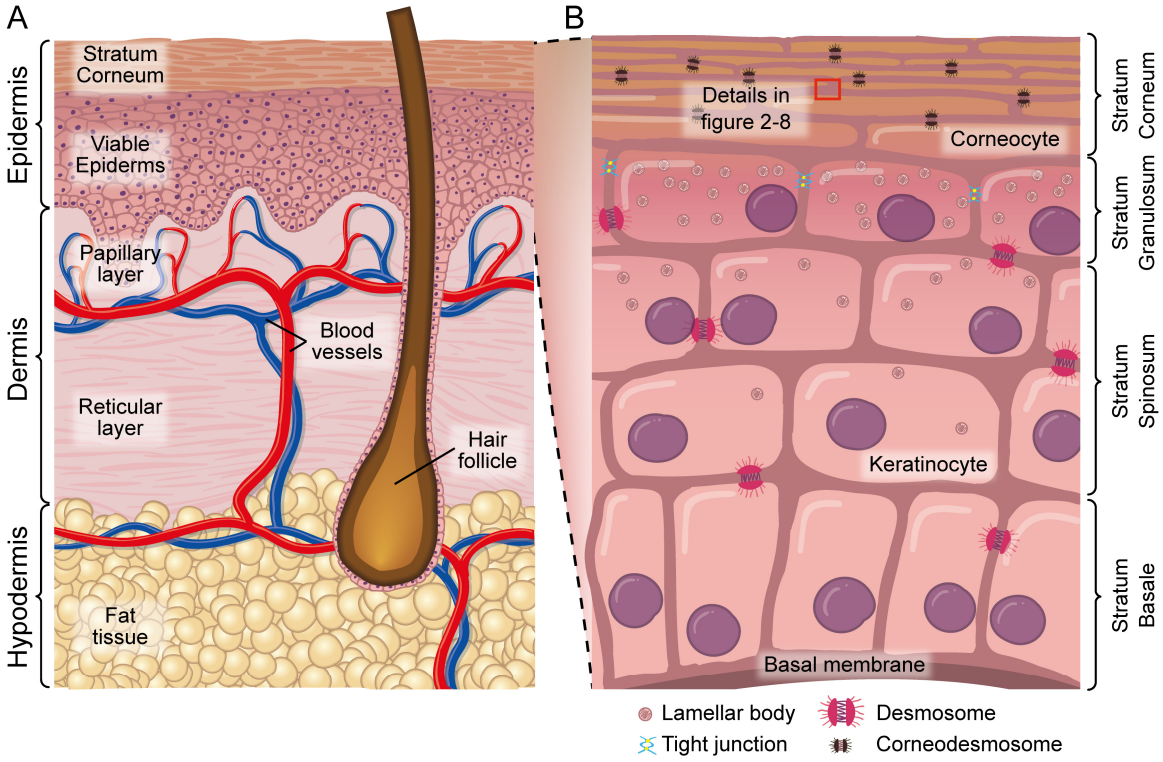

Figure 2-7. Skin morphology. (A) Structure of the three main dermal layers: Epidermis, dermis and hypodermis. (B) Further subdivision of the epidermis into *stratum corneum*, *stratum granulosum*, *stratum spinosum*, and *stratum basale*. Indicated are also structures which are important for the epidermal barrier function. A detailed description of the barrier function of the stratum corneum is given in Figure 2-8.

90% of the local cells. The epidermis is further subdivided into 4 layers based on the proliferation and differentiation of the keratinocytes, *stratum basale*, *stratum spinosum*, *stratum granulosum*, and *stratum corneum* (Figure 2-7B). The *stratum basale* is made up of epidermal stem cells attached to the extracellular matrix of the basal membrane via the protein anchors called hemidesmosomes. They are constantly renewing the suprabasal cell layer, so their metabolic rate is naturally very high. At basal rate only about 15% of the cells are involved in skin cell renewal while the rest is only recruited for wound healing after physical insult of the skin[105]. In the *stratum spinosum*, the newly formed keratinocytes begin to differentiate. Intercellular joints in the form of desmosomes are established and extracellular keratin is built up. In the *stratum granulosum*, intracellular granules start to accumulate. These lamellar bodies contain a multitude of lipid and protein precursors, the destination of which is the *stratum corneum*. These vesicles fuse with the cell membrane of the keratinocytes at the interface of *stratum granulosum* and *stratum corneum* and release their contents into the intercellular space. Lipid processing enzymes, proteases important for desquamation, as well as antimicrobial peptides are cosecreted from the lamellar bodies[106] (Figure 2-8). Cell-cell contacts increase in number. In addition to desmosomes, also so-called tight junctions form at the lateral cell faces and form a selective diffusion barrier which is also involved in

transepidermal water loss. The *stratum corneum* is the outermost layer of the epidermis and the terminal differentiation site for keratinocytes. They lose their nucleus, flatten, and become embedded in a cornified envelope within the intercellular lipid matrix. At this point they are called corneocytes and are metabolically inactive. Lipids from the lamellar bodies are further metabolized into free fatty acids, ceramides and cholesterol which are the main constituents of the intercellular lipid matrix. Together with the cornified corneocytes, it forms the first physical diffusion barrier for foreign pathogens and harmful chemicals and is often depicted as the 'brick and mortar' model for the *stratum corneum*'s barrier function[107]. The *stratum corneum* is typically 15-20 µm thick but can reach a thickness of 170 µm at the palms and feet due to the demand of withstanding higher mechanical stress at those sites[108]. There is a calcium gradient throughout the epidermis, starting with a low calcium concentration in the basal layer, peaking in the *stratum granulosum* and dropping again in the *stratum corneum*. It is thought to regulate most differentiation steps of the keratinocytes as well as cell-cell adhesion, transglutaminase activity[109] and exocytosis of lamellar bodies[110].

2.2.2.2 Skin barrier function

Physical barrier

As stated earlier, the skin hosts a variety of protective mechanisms, most of which are located in the epidermis. They defend the body from a plethora of harmful agents. The *stratum corneum* acts as a physical diffusion barrier, hindering most foreign substances and pathogens to enter the skin. The corneocytes embedded into the tightly interwoven lipid matrix, as depicted in the 'brick and mortar' model[107], form an impermeable structure. The profilaggrin from the lamellar bodies is metabolized into filaggrin which in turn aggregates the keratin inside the corneocytes into tight bundles, covalently linked by disulfide bonds. Together, keratin and filaggrin constitute 80-90% of the protein mass in corneocytes and provide most of their structural integrity[111]. Ceramides, which are specialized lipids, and the proteins involucrin, loricrin and keratolinin form the approximately 15 nm thick cornified envelope around the corneocytes. It is covalently linked by trans-glutaminases, has water repelling properties and acts as a scaffold for the intercellular lipid layers[112]. Lamellar bodies also contain the precursor lipids for the intercellular space of the *stratum corneum*, prearranged in folded double-layers (Figure 2-8A). These lipids are for the most part cholesterol, phospholipids, glucosylceramides, and sphingomyelin. The lipases and proteases to further metabolize these lipids are coexcreted and activated at the interface of *stratum granulosum* and *stratum corneum*. Glycosylceramides are processed into ceramide 1 and 7 while sphingomyelin is transformed into ceramide 2 and 5. Phospholipids are degraded into mostly apolar free fatty acids. This results in an approximately equimolar ratio of ceramides, cholesterol and free fatty acids

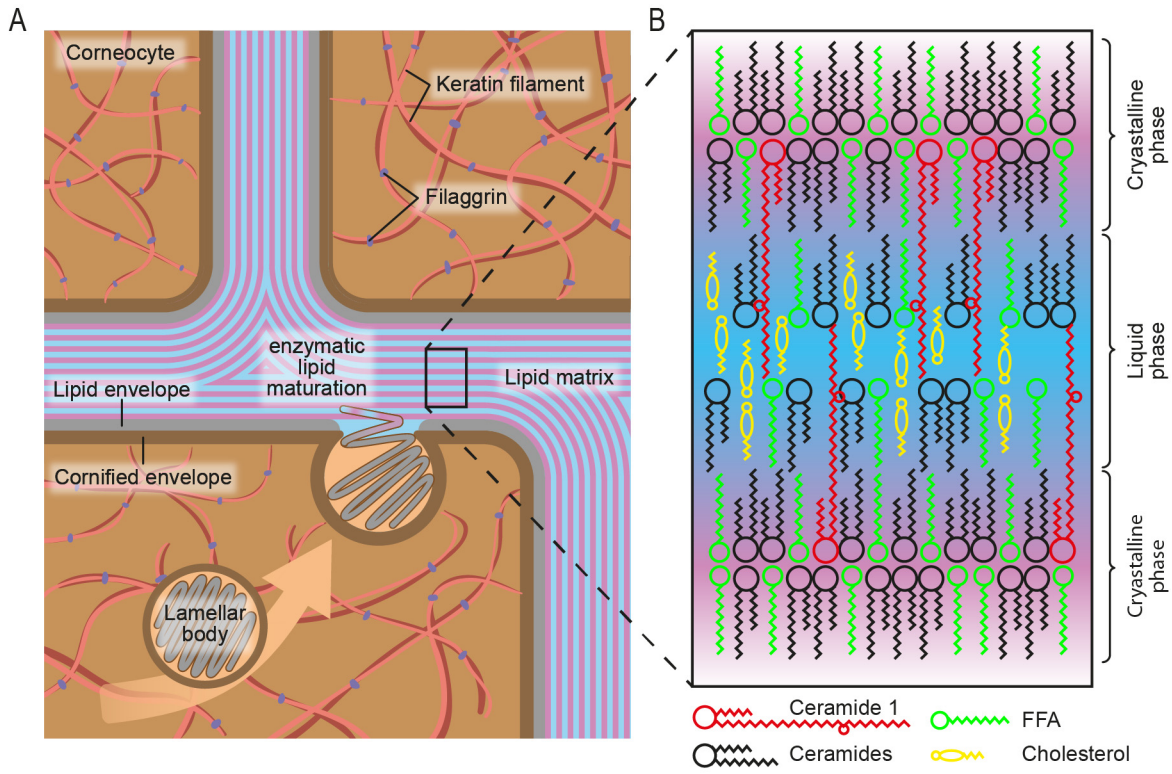

Figure 2-8. Structure of *stratum corneum.* (A) Corneocytes obtain their structural integrity from keratin and filaggrin bundles anchored in the cornified envelope. Folded double layers of precursor lipids are excreted from the lamellar bodies into the intercellular space and are further processed to form the intercellular lipid matrix. (B) The lipid matrix receives its properties from a finetuned mixture of ceramides, free fatty acids (FFA) and cholesterol. The alternating structure of lipid phase and crystalline phase results in a selective diffusion barrier while maintaining mechanical flexibility.

in the intercellular matrix of the *stratum corneum*[106] with a weight distribution of 50% ceramides, 25% cholesterol and 15% free fatty acids (Figure 2-8B)[113]. This specific lipid mixture is very important for homeostasis of the epidermal barrier function and deficiencies in any of those components results in severe impairment of this diffusion barrier[114,115]. The intercellular lipid matrix is a highly ordered structure. It is organized in multilamellar stacks of lipid membranes. The lateral organization of the lipids in the membrane dictates their phase behavior, i.e. the ratio of headgroup volume to tail region determines the packing density of the lipids and by extension the rigidity or fluidity of any lipid membrane. Ceramides and straight-chain fatty acids in the *stratum corneum* are best described by a rod shape which facilitates a dense and tightly ordered packing which forms a much more rigid and impermeable structure then the common cell membrane[116]. In addition, adjacent bilayers are linked via an extensive network of hydrogen bonds[117]. At higher temperatures than the skins physiological 32°C, the bilayers undergo phase transitions and their lipids start to pack less dense. These phase transitions aren't accompanied by a significant loss in barrier function, indicating that the multilamellar organization is of much greater importance than the specific packing geometry[118]. Additionally, cholesterol forms defects of the tight packing when inserted into

the membrane, which provides more flexibility and fluidity to the lipid matrix. These defects are also the basis for small hydrophobic and hydrophilic diffusion pathways through the *stratum corneum* (Figure 2-8B, Figure 2-9B)[119].

Biological diffusion barrier

Another large part of the epidermal permeability and structural integrity are the variety of anchoring mechanisms forming cell-cell contacts, namely tight junctions, adherens junctions, desmosomes, corneodesmosomes, and other protein-protein interactions[120]. Adherens junctions couple intercellular adhesion to the cytoskeleton thereby contributing to the epidermal mechanical cohesion but also form a intercellular signaling platform which orchestrates cytoskeletal dynamics and coordinates cell polarization in the basal layer[120]. They are mainly mediated by the calcium dependent cadherins of neighboring cells linked to the cytoskeleton by catenins or nectins. Desmosomes are mechanical junctions which also utilize cadherins, but are formed primarily at lateral cell interfaces for cell cohesion. During the differentiation of keratinocytes, desmosomes are constantly built up and retrieved but stabilize with rising calcium levels. Hence, naturally they are found in highest concentration in the *stratum granulosum* but are gradually replaced by corneodesmosomes in the *stratum corneum*. Corneodesmosomes are specialized glycoproteins which further increase mechanical integrity of the tissue while decreasing the permeability of the *stratum corneum*[121]. The coordinated digestion of corneodesmosomes in the outer *stratum corneum* is necessary to eventually permit desquamation[120]. One last example of cell-cell contact points are tight junctions. They form at the lateral plasma membrane of keratinocytes in the *stratum granulosum* and are seen as a selective barrier also involved in water and ion transport through the outer layers of the skin. They help maintain polarity of the cells and might also regulate apical vesicles secretion thereby actively influencing the barrier formation at the interface of *stratum granulosum* and *stratum corneum*[120]. Although over 40 proteins have been identified within tight junctions, the most important protein families which form tight junctions are claudins and occludins which are connected to the cytoskeleton by zonula occludens (ZO) proteins[122]. While claudins are present throughout all epidermal layers, occludin is exclusive to the *stratum granulosum* and only here functional tight junctions are formed, indicating the importance of both proteins interplay for efficient regulation of transepidermal diffusion.

Physico-chemical barrier

In addition to the diffusion barrier, the skin is also equipped with a variety of biochemical mechanisms complementing the physical barrier in hindering the penetration of pathogens. The cornified envelope provides strong chemical resistance for the *stratum corneum* as its pH is relatively acidic with pH as low as 4.5-5[123] but with a gradient to normal pH with increasing skin

depth. It is water repellent and resilient against mechanical force. The pH is influenced by several endogenous as well as exogenous factors like skin moisture, sweat and sebum production, anatomic site, genetic predisposition, age, detergents, cosmetic products used, and not least occlusive dressing. Although some pathways are known which lower the pH in the *stratum corneum*, the exact origin and objective of the low pH isn't fully understood yet[106,114]. It is clear that this 'acid mantle' of the skin greatly decreases the permeability for bacteria and as such acts as an antimicrobial system[106]. The acidic environment also helps in selecting for a harmless physiological skin surface microflora which additional prevents pathogenic invasion[124]. Free fatty acids and sphingosine, abundant in the lipid matrix in the *stratum corneum* has also been proven to exhibit antimicrobial, antiviral and antifungal properties[121]. Defensins, antimicrobial peptides, are permanently present in the epidermis and serve as an integral component of the innate immune response[121] and ensure the homeostasis of the skins barrier function. Lastly, a great many of immunocompetent cells in dermis and epidermis readily initiate a cytokine induced immune response after physical insult or pathogen penetration[106,114]. As such, the skin is considered a pro inflammatory organ and is an important part of the immune system comprising active and passive components.

2.2.2.3 Dermal and transdermal drug delivery

The most important advantage of the dermal and transdermal drug delivery compared to oral or intravenous administration is the significant lower metabolic activity of the skin compared to the liver. This results in longer retention times, more evenly distributed blood levels with possibilities for continuous delivery and with that fewer side effects and less strain on other organs. It is most advantageous of course for the treatment of skin diseases like psoriasis or atopic dermatitis.

The diffusion through the epidermis in particular the *stratum corneum*, the outermost skin layer, is mainly determined by the physico-chemical properties of the penetrating agent. Generally, there are three conceivable transepidermal penetration routes: the transfollicular or tranglandular pathway, the inter-, or the intracellular penetration pathway. The transfollicular rout promotes the penetration of particles with a size range of about 300-600 nm in diameter, probably taking advantage of the physical shape of the hair surface with scaly features on the same order of magnitude [125-127].

The intracellular route is the shortest but by far also the most unlikely route since any given drug has to pass the apolar regions of the lipid matrix as well as the polar region of the corneocytes cytosol alike[128]. This leaves the intercellular route where molecules diffuse solely in the lamellar region of the lipid matrix. Here again, the specific properties like hydrophilicity, size, charge and

flexibility of the diffusing agent ought to be considered as the lipid matrix features hydrophobic as well as hydrophilic regions but with different diameter. Studies found 3.8 nm for the lipophilic region and 0.5 nm for the hydrophilic space providing estimates for the upper size limits for polar and apolar molecules[129].

Lipophilic molecules are generally found to perform better in penetration studies but without penetration enhancers, there is the standing rule of thumb which considers 500 Da to be the upper limit for efficient transepidermal transport[5]. However, penetration of 200 nm nanoparticles into deeper skin layers has been observed recently[130], rendering nanoparticle assisted drug delivery as a promising tool for drug penetration studies. The diffusivity of polar molecules have been found to correlate with their partitioning coeffcient[131] but has it has also been suggested that hydrophilic molecules might penetrate via defects in the *stratum corneum* and not exclusively through the intercellular space. These defects form where corneocytes do not properly overlap and lipids aren't as ordered as usual[5,132]. Theses pathways most likely don't exceed 10 nm but depending on skin condition, they can widen to 20-30 nm[5]. Induced by occlusion, prolonged hydration or iontophoresis, aqueous pathways formed by these lacunar domains within the *stratum corneum* might expand and interconnect to constitute a continuous porous system through the *stratum corneum*[133,134]. Penetration enhancer like hydrogels might take advantage of this effect and increase the permeability of the *stratum corneum* via extensive exposure to water. Beyond that, most penetration enhancer aim to disrupt or fluidize the lipid lamellae of the *stratum corneum* or

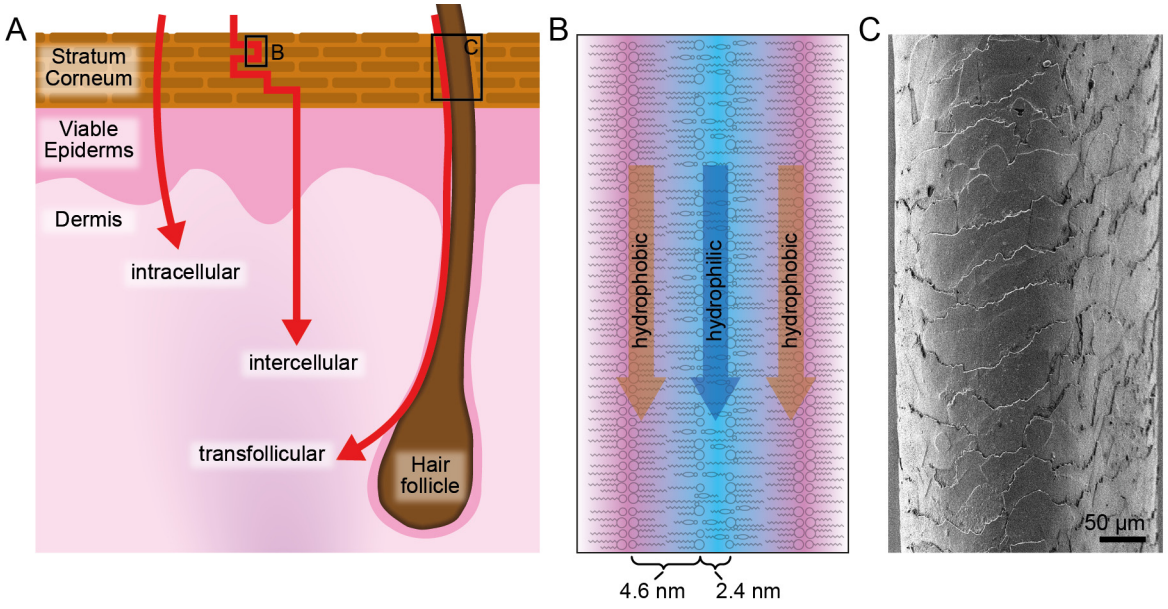

Figure 2-9. Transdermal penetration pathways. (A) Intracellular, intercellur, transfollicular penetration pathway through the epidermis. (B) Hydrophobic and hydrophilic channels through the intercellular matrix of the *stratum corneum*. (C) SEM micrograph of the human hair (permission under CC by 3.0, credit goes to the CSIRO).

improve the uptake of the drug using a vesicular formulation like liposomes. Generally, the complex interplay of the multitude of penetrator properties and skin conditions are difficult to assess a priori which makes predictions over the penetration behavior of any given substance challenging.

Nanocarriers and nanoparticles for assisted drug delivery have been investigated for over a decade now but still growing interest[135]. They can be utilized to enhance solubility of hydrophobic drugs, increase stability, and provide the means for controlled release. Fort topical drug delivery, the most common nanoparticles are polymeric nanoparticles, nano-emulsions, liposomal formulations, metal nanoparticles, and hyperbranched dendrimers[136].

Solid lipid nanoparticles have been found to enhance skin penetration of drugs and the hydrophobic dye Nile Red[137]. Polymeric particles also provide improved drug delivery[138] and increase drug tolerability[139], but have recently gained special interest as their tumor targeting capabilities have been revealed[140,141]. As the drugs pharmacokinetics are increased using dermal and transdermal delivery systems, systemic side effect which would otherwise occur after oral administration are also effectively mitigated[142]. Furthermore, core-multishell (CMS) architectures have been found to accumulate in the outermost skin layer and release their cargo from there. This reservoir function proved advantageous as dose and frequency of drug administration can be effectively reduced[143]. Nanoparticle assisted drug delivery is especially effective through the transfollicular route. Based on the hair surface structure, there seems to exist an optimal diameter for nanoparticles of about 600 nm which promotes a penetration deep into the hair shaft and enables a lateral diffusion into the adjacent dermis[125-127]. Therefore, nanoparticles hold a great promise for novel drug delivery systems but also require careful analysis and characterization of penetration pathways and modes of action to use them to their fullest potential.

3 Materials and Methods

3.1 Fluorescent reporter groups

An overview of all used fluorescent reporter groups can be found in Table 1 and Figure 3-1. 6-aminofluorescein was purchased from Carl Roth (45350, Carl Roth, Germany), Rhodamine B was purchased from Fischer Scientific (Fischer Scientific GmbH, Germany), and Nile Red was purchased from Merck as microscopy grade (Merck, Germany). The free dye Indocarbocyanine (ICC) was used as its sulfated NHS-ester derivative (Mivenion GmbH, Germany). ICC conjugated to the dendritic polyglycerol sulfate (dPGS) was also provided by Mivenion GmbH, Germany. The conjugation of ICC to the dPGS particle was done by Dr. Kai Licha (Mivenion GmbH, Germany) and a detailed description of the process can be found here[144]. Wheat germ agglutin with covalently bound ICC (WGA-ICC) was purchased from Zellbio (21761148-1, ZellBio, Germany). It was provided in aqueous solution with a concentration of 20.9 µM. WGA is a lectin which is able to bind to N-acetyl-glucosamine and sialic acid[145]. Both sugar moieties are posttranslational modifications abundantly found in mucins. As such, WGA is well suited to label the mucin network with the fluorescent probe ICC. The WGA structure and in particular the binding pocket to which the glycans of mucin bind is shown in Figure 3-2.

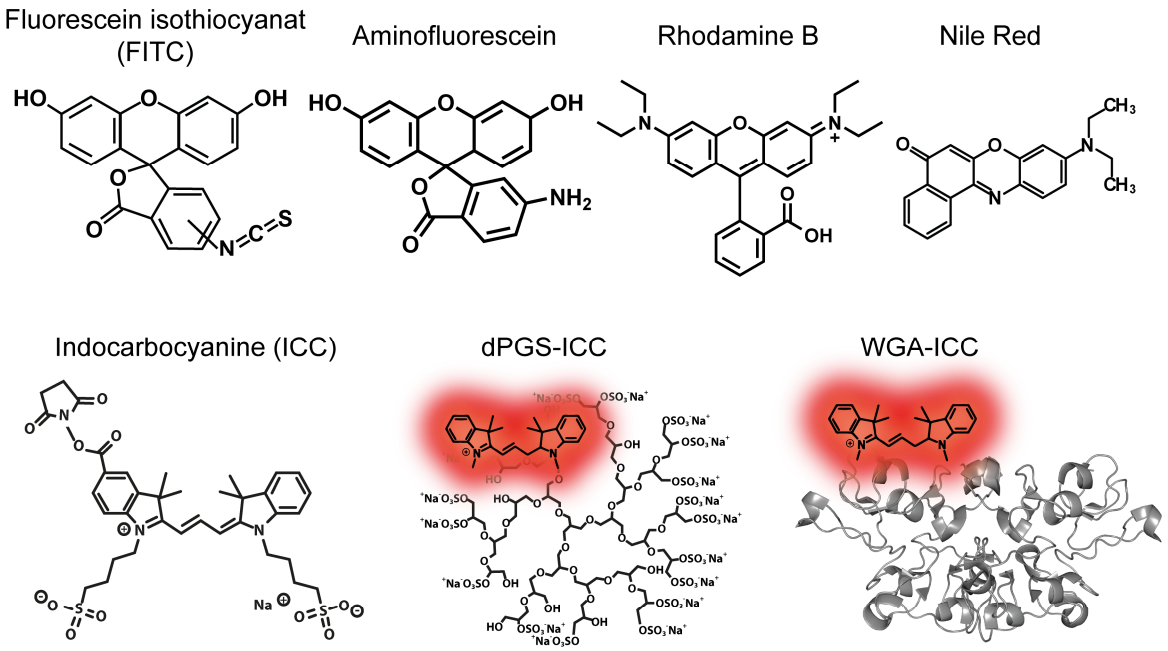

Figure 3-1. Structural formula of all fluorophores used in this thesis.

Table 1. Overview of fluorophores and its properties used in this thesis. *molar extinction coefficients of dPGS-ICC and WGA-ICC were adopted from the free dye ICC.

Fluorophore	extinction coefficient	molecular weight	λ_{max}(abs)	λ_{max}(em)	solvent
Aminofluorescein		347.3 Da	488 nm	514 nm	TRIS pH 9
Rhodamine B (RhoB)	106000 $cm^{-1}M^{-1}$	479.0 Da	555 nm	581 nm	Ethanol
Fluorescein isothiocyanate (FITC)	73000 $cm^{-1}M^{-1}$	389.4 Da	498 nm	516 nm	TRIS pH 9
Indocarbocyanine (ICC)	130000 $cm^{-1}M^{-1}$	767.0 Da	550 nm	565 nm	Ethanol
dPGS-ICC	130000 $cm^{-1}M^{-1}$*	12 kDa	553 nm	572 nm	Water
WGA-ICC	130000 $cm^{-1}M^{-1}$*	38 kDa	550 nm	564 nm	Water
Nile Red	38000 $cm^{-1}M^{-1}$	318.4 Da	559 nm	635 nm	Ethanol

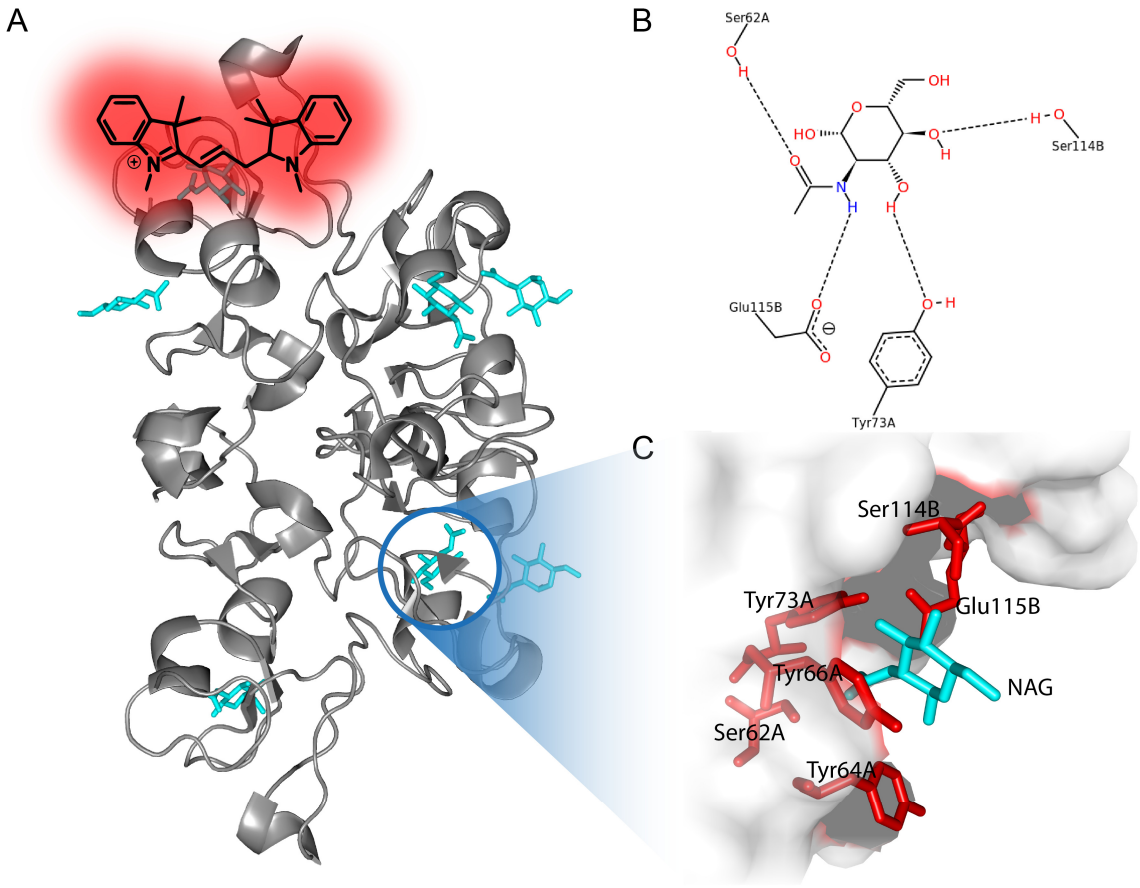

Figure 3-2. (A) Structure of WGA-ICC and its (B, C) N-Acetylglucosamine (NAG) binding pocket (2UVO).

3.2 Steady-state absorption and fluorescence emission spectroscopy

Steady-state absorption measurements were performed on either a UV-2450PC dual-beam UV-VIS scanning spectrophotometer (Shimadzu, Japan) in parallel mode or on the NanoDrop™ One micro-volume UV-VIS spectrophotometer. The UV-2450PC in conjunction with 3x3 mm quartz cuvettes (Hellma, Germany) was primarily used for initial characterization of a compound. Its superior accuracy is better suited to resolved spectral features of a compound. The NanoDrop™ One on the other hand was used to quickly assess the concentration c of a given solution using Lambert-Beers law:

$$A_\lambda = \varepsilon_\lambda * \mathrm{c} * \mathrm{d} \tag{27}$$

where ϵ_λ is the wavelength dependent molar extinction coefficient, A_λ is the optical density and d is the path length. Note that the NanoDrop™ One when in micro-volume mode shows the optical density as normalized to 1 cm. Using the micro-volume mode though, has the advantage that only a volume of 1-2 µl has to be expanded to determine dye concentration.

Steady-state ensemble fluorescence measurements were recorded with a SPEX Fluoromax 3 spectrophotometer (HORIBA Jobin Yvon, Japan) in L-format configuration using the DataMax Software Version 2.20. If not otherwise indicated emission spectra were recorded at 20°C.

3.3 Time-dependent fluorescence decay measurements of fluorescent ensembles

Time-resolved fluorescence spectroscopic investigations of fluorophores and fluorescently labeled nanoparticles are achieved via time correlated single photon counting. In order to resolve the fluorescence decay of a sample, we need to generate an ensemble of excited molecules at a defined point in time t_0. In our setup(Figure 3-3), in the group of Prof. Alexiev (FU Berlin, Germany)[146,147],

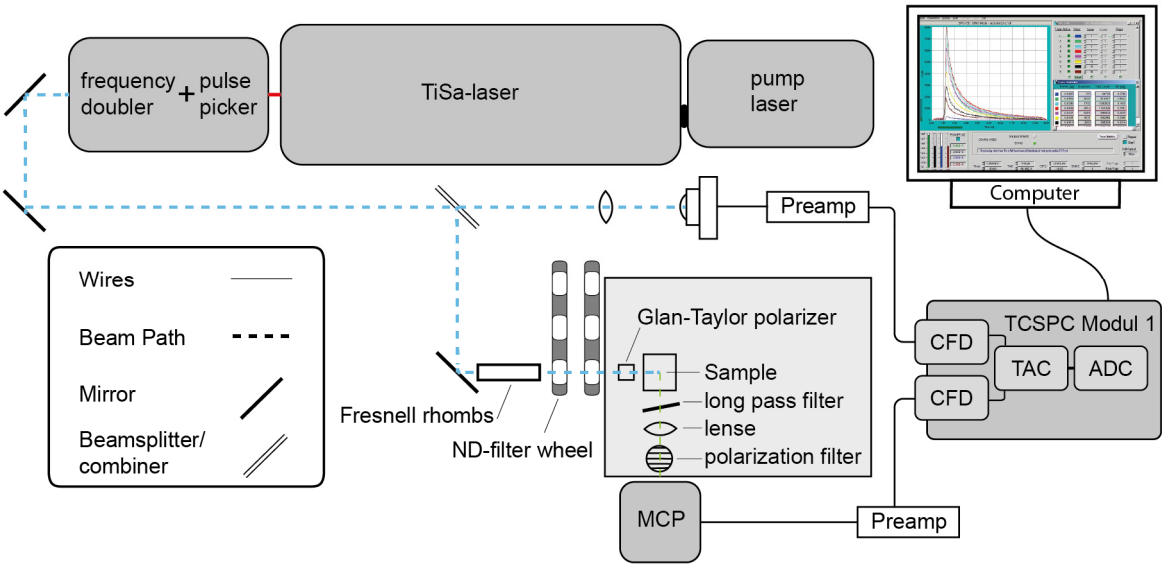

Figure 3-3. Ti:Sa TCSPC cuvette setup.

this is achieved via a titanium-doped sapphire (Ti:Sa) laser. The Ti:Sa crystal of the Tsunami laser (Spectra physics) is pulse by the 5W continuous wave diode laser Millenia V (Spectra physics) at 532 nm. Ti:Sas stand out since they have an especially broad gain bandwidth of about 300 nm, centered around 800 nm, allowing more longitudinal modes in the laser cavity. Modes with fixed phase relation are then allowed to periodically constructively interfere to form a very short and intense pulse of laser light. In our setup, we achieve pulses with FWHM of about 1-2 ps and a repetition rate of 82 MHz (one pulse every 12.2 ns), tuned to 976 nm. The mentioned repetition rate would be to high for most fluorophores und would result in one fluorescence decay stretching over several pulse cycles, which can not be readily be accounted for. In a next step, pulses from the Ti:Sa will be picked and also frequency doubled which results in 4 MHz at 488 nm. Before the pulse train excites the sample, it is split into two paths, one of which is redirected to hit a photodiode. The signal from the photodiode will be used as a reference point in time for the recorded fluorescence photons. Furthermore, the photodiode is connected to an oscilloscope which allows for the optical inspection of the laser pulse shape. The other laser path is directed through a pair of Fresnel rhombi which effectively switches the polarization of the excitation light from horizontal to linear vertical. And additional Glan-Taylor polarizer directly in front of the sample filters out any light not polarized vertically to ensure very uniform excitation. A pair of neutral density filter wheels in combination with appropriate fluorophore concentration in the order of single digit µM is used to adjust the fluorescence intensity so low, that an average of one photon hits the detector in 200 pulse cycles. This is needed to avoid the arrival of a second photon during the dead-time of the detector, the so-called pileup effect, which would artificially shorten the measured fluorescence decay time. The fluorescence of the sample is recorded under a 90° angle and after passing a suitable longpass filter. Both measures are taken to avoid scattered photons reaching the detector. Additionally, a movable polarizer is used for detection of polarized light with fixed relation to the polarization of the excitation light, i.e. 0° meaning parallel and 90° meaning perpendicular, facilitating time-dependent anisotropy measurements. It is set to 54.7°, the magic angle, to suppress any contributions of an anisotropic emission, if only the fluorescence decay time is of interest. The arrival of the fluorescence photons is registered by a multi-channel plate (MCP). Since signals from the MCP and the photodiode are not δ-peaks, constant fraction discriminators (CFD) are used to determine the exact time of arrival of the photon. For this purpose, the signal is doubled, one part is inverted and slightly offset in time and subsequently both peaks are added again which leads to a signal with a zero crossing which is then used as the arrival time of the photon. In the time to amplitude converter (TAC), an incoming signal triggers a capacitor to start charging and the second signal stops the charging process. In this arrangement, the charge on the capacitor is directly proportional to the delay time Δt between the two signals. The voltage values

are then passed on to the analogue-digital converter and are store as Δt in a histogram. Given a sufficient photon statistic, this histogram is equivalent to the fluorescence decay of the fluorescent ensemble. It should be noted that our setup runs in inverse mode. This means the fluorescence photon will start charging the TAC and the diode signal, which now is fed into a delay loop, will stop it. This avoids having to charge and discharge the TAC every time a reference pulse is registered at the photodiode effectively reducing dead time of the electronics by a factor of 200. It was mentioned before, that even though the laser pulse is only 1-2 ps wide, the electronics additionally broaden the signal during processing, leading to a non-neglectable instrument response function (IRF) which is convoluted with the measured fluorescence decay. This is accounted for by recording scattered light pulses which are later used to deconvolute the fluorescence data. In our setup we achieve IRFs with typically FWHM of ~40 ps.

3.4 Time-domain fluorescence lifetime imaging microscopy

Fluorescence lifetime imaging microscopy data of fluorescent samples were collected on a home-built setup[148,149] (Figure 3-4) consisting of a white-light supercontinuum laser (WLS, SuperK Extreme EXU-3, NKT photonics, Denmark), a confocal scanning unit (DCS-120, Becker& Hickl, Germany) and an inverted microscope (Olympus ix71, japan). In the WLS, a polarization maintaining single-mode nonlinear photonic crystal fiber (PCF) is pumped by a ~5 ps seed pulse at 1064 nm. A plethora of non-linear optical effects, most notably self-phase modulation and four-wave mixing, lead to a massively broadened laser spectrum ranging from 400 nm to 2400 nm. The seed frequency is usually reduced by a pulse picker to 19.5 MHz, again, to avoid secondary excitation during the initial decay process. From the broad band spectrum, up to 8 narrow bands (1.8-8.5 nm) can be selected using an acousto-optical tunable filter (AOTF) (SuperK SELECT UV-VIS, NKT photonics, Denmark) and individually modulated in intensity. Laser pulse width FWHM ranging from 82.6 ps at 405 nm (2.4nm width) to 51.9 ps at 640 nm (7 nm width). Unfortunately, the AOTF by itself is not sufficient to suppress all photons of unselected wavelengths. Due to dispersion, these photons are shifted in their arrival time with respect to the selected wavelength. Especially red-shifted photons will not be filtered by the long-pass emission filter and arrive unhindered at the detector which leads to artefacts in the rising flank of the fluorescence decay i.e. a shallow rise or even prepeaks. Those artefacts make it next to impossible to perform a proper deconvolution with the instrument response function and necessitate the use of a quad-band-pass filter (ZET 405/488/532/642, Chroma, USA) to clean up the signal while maintaining sufficient flexibility with 4 commonly used beamlines. The laser pulses are now routed to the confocal scanning unit (DCS-120, Becker& Hickl, Germany) via a broadband connection fiber (FD7, NKT Photonics, Denmark). The DCS-120 scanning

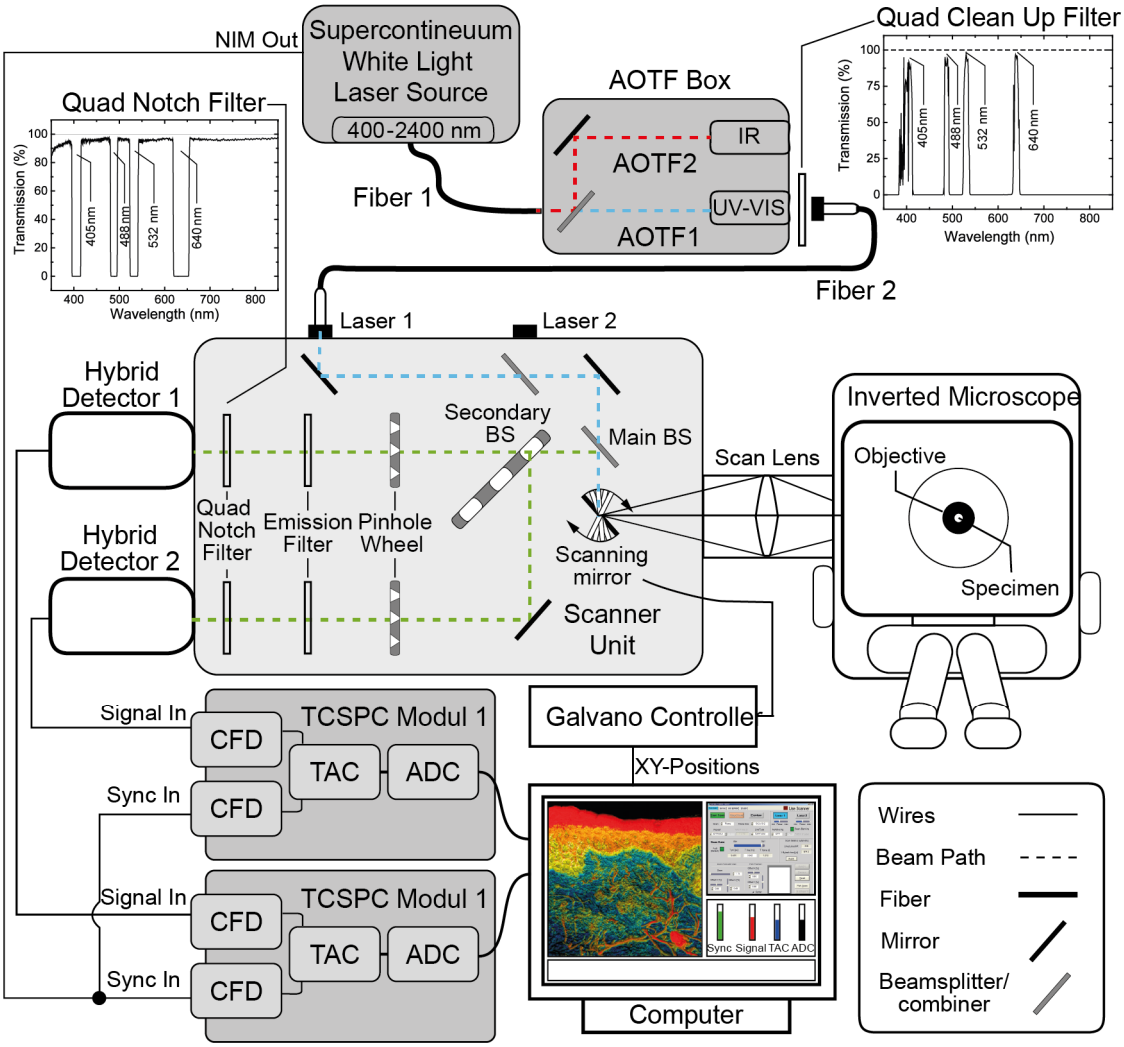

Figure 3-4. Fluorescence lifetime imaging microscopy setup, scheme adapted from [149].

unit houses the complete set of optics for beam deflection and detection. Here, it passes the main dichroic mirror (z405/473, Becker & Hickl, Germany), hits the 2-axes galvanometer scanning mirror and is finally directed into the inverted microscope (IX71, Olympus, Japan) where a scanning lens focuses the excitation light onto the sample. The scanning mirror is driven by the galvano controller (GVD120, Becker & Hickl, Germany). One Frame (512x512 px) is typically scanned with pixel dwell times of 5 µs leading to an acquisition time of 1.3 s/frame. The field of view (FOV) is mainly determined by the objective. A 60x objective (UPLSAPO60XW, Olympus, Japan) for example leads to a FOV of maximal 300x300 µM. Accordingly, lower magnification relates to a bigger FOV. The sample is illuminated with a laser power of up to 0.22 mW at 530 nm with a repetition rate of 19.5 MHz, usually low enough to avoid phototoxicity in live specimen. The fluorescence photons are collected again by the objective, focused by the scanning lense and descanned by the scanning mirror. In the DCS120, a secondary beam splitter wheel allows for the simultaneous use of two detectors. The wheel has options for '100 % detector 1', '100 % detector 2', '50 % to both detectors' and 2 polarization filters. Each detector path has its individual set of pinholes and emission filters.

The pinhole wheel facilitates the fast switch between pinholes ranging from 0.25 -2.5 airy units (AU). One AU is the diameter of a pinhole transmitting only the airy disc, the 0th order diffraction maximum, of the diffraction limited spot scanned over the focal plane (sample). So, the pinhole effectively increases resolution by blocking any out-of-focus photons. The two filter slots in the DCS120 are typically used for one suitable long pass filter and a quad-notch filter to block any scattered excitation photons and produce a pristine fluorescence signal. The detectors are GaAsP hybrid photo multiplier tubes (HPM-100-40, Becker & Hickl, Germany) with an IRF of 120 ps FWHM and quantum efficiency of 45 % at 500 nm. Detected fluorescence signal as well as the laser sync are further processed in the TCSPC module (SPC-160, Becker & Hickl, Germany). For details on TCSPC electronics, see previous section. Decay traces are recorded into 1024 time channels with a channel width of 19.5 ps. We used the SPCM software (SPCM 9.82, Becker & Hickl, Germany) to display the initially recorded FLIM data and control detector voltages as well as the scanning mirror.

3.5 Data analysis

3.5.1 Analysis of FLIM data using Cluster-FLIM

In FLIM, special attention has to be given to photon statistics as spatially resolved lifetime data is notoriously starved for photon counts in particular when compared to ensemble measurements. Not only is the brightness of a sample divided laterally into 512x512 pixels but also temporally into 1024 time bins. Therefore, it follows a short digest of photon numbers needed for a desirable signal-to-noise ratio (SNR). For a mono-exponential decay under background free measuring conditions, the σ is given just given by the inverse square root of photons N recorded, assuming Poisson statistics[150]:

$$\sigma = 1/\sqrt{N} \text{ or } N = 1/\sigma^2 \tag{28}$$

so, determined with the same accuracy as fluorescence intensity. Considering a frame with $p_x \times p_y$ dimensions and a count rate R, the acquisition time T can be calculated from:

$$T = \frac{p_x \cdot p_y}{\sigma^2 \cdot R} \tag{29}$$

achievable count rates for sufficiently bright samples are on the order of $10^5/s$ to $10^6/s$. Higher count rates are possible but lead to pile up and might cause photobleaching or even phototoxicity in the sample. So, best case scenario for a $\sigma = 10\%$ measurement would be an acquisition time of 26 s but already 44 min for $\sigma = 1\%$. Its even worse for multi-exponential decays. For just a bi-exponential decay function, Poisson statistics leads to an unattainable photon number of $N = 400000$ per pixel[151], completely out of reach for any biological sample. Under favorable ratios of

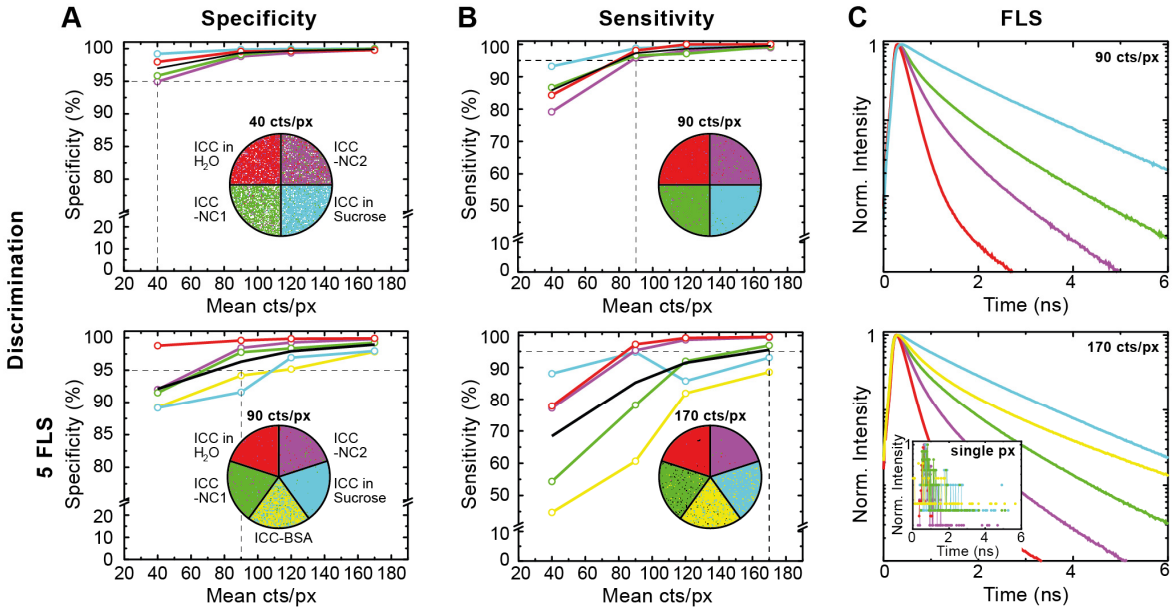

Figure 3-5. Validation of Cluster-FLIM for the fluorophore ICC in 4 and 5 different environments. (A) Specificity (correct rejection rate) and (B) sensitivity (hit rate) is calculated from experimental data as a function of mean pixel counts (40, 90, 120, 170 cts/px). Samples: ICC in H2O (red), in 69% sucrose (w/w) (cyan), attached to NC1 (CMS-ICC, green), to NC2 (dPGS-ICC, magenta), and to bovine serum albumin (BSA) (yellow). Cluster-FLIM images for the respective mean pixel counts to obtain either 95% specificity or 95% sensitivity (indicated as the intersection of the horizontal and vertical dashed lines) are shown. White pixels in (A) are below a threshold of 10 cts/px and do not contribute to the Cluster-FLIM analysis. (C) Fluorescence lifetime signatures (FLS) for mean pixel counts at 95% sensitivity. Inset: Fluorescence decay in a single pixel at 170 cts/px for comparison. Table A1 summarizes the different fluorescence lifetimes (mean fluorescence lifetime varies between 0.20 ns and 1.53 ns). Experimental conditions for ICC: λ_{ex}=530 nm,λ_{em}=545-600 nm. The measurements were performed together with Pierre Volz-Rakebrand. Figure adapted [152].

the lifetime components this number can be brought down to 10000 but this relates still to an acquisition time of almost an hour. The conventional approach to this problem is local binning during analysis, integrating photon counts not just over one pixel but also over its neighbors, under the assumption that fluorophores in lateral proximity also share fluorescence decay behavior and that the airy disk comprises several pixels anyway. The latter does not necessarily hold true for high numerical apertures and sub 1 AU pinholes, so this approach effectively reduces acquisition time at the cost of resolution. We circumvent the problem of extracting the potentially multicomponent fluorescence decay characteristics with superimposed Poisson distributed noise from a single pixel by sorting all the pixels into meaningful groups with shared decay characteristics first and -if needed- extract their multicomponent decay afterwards. This multivariate analysis method, which we call Cluster-FLIM, was developed by Robert Brodwolf in the group of Prof. Alexiev (Physics Department, FU Berlin, Germany).

Clusters in the feature space comprise pixels containing a shared fluorescence decay characteristic originating in a common microenvironment of the fluorophore, thus, forming the unique fluorescence lifetime signature (FLS) of this microenvironment. Based on this supposition, it is justified to treat all members this cluster as one, which massively increases photon statistics. Note that cluster members are not necessarily sourced from one FLIM measurement only. It is rather instructive to include several reference measurements into the data set to find better cluster center for a FLS and further increase photon statistics. The problem of identifying the correct decay behavior in one pixel has thus shifted to assigning that pixel to the correct cluster, which is a much simpler problem and backed up with much better statistics. A validation of the method can be found in [152]. In particular, I evaluated Cluster-FLIM with regard to sensitivity and specificity (Figure 3-5[152]). For this purpose, ICC has been measured in four or five different microenvironments. Subsequently, all measurements were analyzed together. Sensitivity and specificity have been calculated for the analysis using:

$$sensitivity = \frac{number\ of\ true\ positives}{number\ of\ true\ positives + number\ of\ false\ negatives} \tag{30}$$

$$specificity = \frac{number\ of\ true\ negatives}{number\ of\ true\ negatives + number\ of\ false\ positives} \tag{31}$$

Where the truth value is based on whether the correct fluorescence cluster of a pixel was assigned to the microenvironment in which the fluorophore was measured (Figure 3-5 circular insets). 95% specificity (Figure 3-5A) and 95% sensitivity (Figure 3-5B) for the discrimination of four microenvironments (Figure 3-5 top row) was achieved by Cluster-FLIM with photon numbers as low as 40 and 90 counts per pixel, respectively. For the discrimination of 5 microenvironments (Figure 3-5 bottom row) 90 and 170 counts per pixel were necessary. Figure 3-5C shows the resulting fluorescence decay curves of the respective clusters. The inset in Figure 3-5C conveys an impression of what the decay curves in one pixel would look like when using conventional analysis software with 170 counts per pixel, no separation of between fluorescent species would be possible based on these data. This demonstrates the advantages of Cluster-FLIM for the extraction of multiexponential fluorescence decay curves from FLIM data even with low photon counts.

3.5.2 Lifetime fitting and exhaustive error analysis

Fluorescence decay traces recorded in the TCSPC cuvette setup were analyzed using the program Global Unlimited V2.2 (Laboratory for Fluorescence Dynamics, University of Illinois, USA). The goodness of the fit was judged from the reduced χ^2. In most cases, measurements were considered satisfactory if a $\chi^2 < 1.6$ was reached. Each measuring day a standard sample of fluorescein sodium salt in TRIS buffer pH 8-9 was measured to check the alignment and calibration of the setup (Figure 3-6). This sample exhibits a monoexponential decay with $\tau = (4.10 \pm 0.05)\, ns$, which should be result in a fit with $\chi^2 = 1.0$, or else the setup had to be realigned.

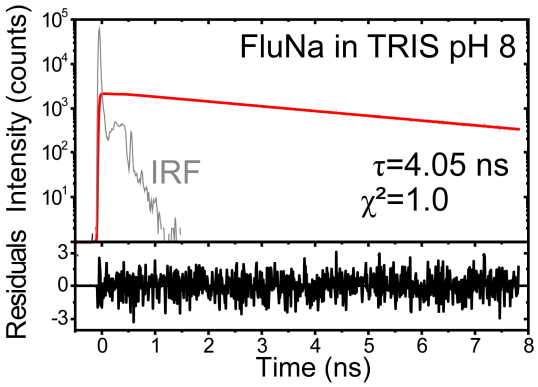

Figure 3-6. Exemplary fit (red line) of the standard sample fluorescein sodium salt (FluNa) in TRIS buffer at pH 8. The instrument response function (IRF) is shown in grey, the fit residuals in black in the bottom panel. A successful fit with a single exponential decay with τ=4.1 ns and χ²=1.0 is used as a quick check for the setup alignment.

Lifetime data from the FLIM setup was analyzed using a self-written pearl script (by Robert Brodwolf, Prof. Alexiev, FU Berlin, Germany). Again, the χ^2 value served as indicator for fit quality. Though, clustering of many pixels into one combined decay curve resulted in much higher photon statistics which leads to an artificially increased χ^2. Although typically the χ^2 was below 2, occasionally higher values had to be accepted. The accuracy of the fits was determined by 5 repetitions of fitting the same data set. The standard deviation (SD) of these repetitions is indicated as error in the later presentation of lifetime fits.

To precisely assess the accuracy of the fit in specific cases, we conducted an exhaustive error analysis. For this purpose, a normal fitting procedure is carried out, minimizing χ^2. Subsequently, all parameters a_i of this fit are examined for their confidence interval. Here, 10 different values in an interval ±20% around the optimal value for the parameter a_i are assumed and fixed for the following fitting. The resulting χ^2 is then plotted over the fixed value of a_i. From the cumulative χ^2 distribution $F(x,k) = P\left(\frac{k}{2}, \frac{x}{2}\right)$, where P is the incomplete gammafunction, with the degree of freedom (k=1), the interval can be calculated in which a_i can be found with the probability p. In

analogy to the Gaussian distribution, the probabilities of the confidence levels of the standard deviation are applied, i.e. $p = 68.27\%\ (1\sigma), p = 95.45\%\ (2\sigma), and\ p = 99.73\%\ (3\sigma)$. The confidence levels are calculated from:

$$\chi^2_{confidence\ level}(p,x) = \chi^2_{min} + \frac{\Delta\chi^2(p,x)}{N} \tag{32}$$

Finally, the intercepts of the confidence levels with the plot of χ^2 over a_i defines the error interval.

3.6 Parallax method for determination of dPGS-ICCs membrane incorporation

Fluorescent spectra of dPGS-ICC after excitation with $\lambda_{ex} = 530\ nm$ were recorded in the range of $\lambda_{em} = 550 - 750$ nm as a function of addition of different spin-labeled lipids. As spin-labeled lipids we used 1-palmitoyl-2-stearoyl-(5-doxyl)-sn-glycero-3-phosphocholine, 1-palmitoyl-2-stearoyl-(7-doxyl)-sn-glycero-3-phosphocholine and 1-palmitoyl-2-stearoyl-(12-doxyl)-sn-glycero-3-phosphocholine (16:0-5 Doxyl PC, 16:0-7 Doxyl PC, and 16:0-12 Doxyl PC) (Avanti Polar Lipids, Alabaster, Alabama, USA). Each lipid was mixed with DMPC with a molar fraction of 0.1 and 0.25 and consequently processed into large unilamellar vesicles (see below). The estimated distances from the spin-label to the bilayer center for the 5, 7, and 12 spin-labeled lipids are 12.15, 10.35, and 5.85 Å, respectively (0.9 Å per carbon and 0.45 Å from the final carbon of the fatty acid chain to the lipid bilayer center[43]).

3.7 Lipid vesicle preparation

Large unilamellar vesicles (LUV) were produced based on a two stages process. First, multilamellar vesciles (MLV) based of the desired lipid mixture were produced. We used the thin film method for this stage[153]. Here, 1mg DMPC/DOPC is placed into a glass test tube and dissolved in chloroform to a concentration of 1.5 mM. If desired, additional membrane components like spin-labeled lipids or cholesterol are added in required molar ratios at this point. Consequently, the chloroform is evaporated under a steady nitrogen stream, leaving a thin film of stacked lipid membranes clinging to the glass wall of the test tube. The lipid film is then rehydrated with 5 mL H_2O-MQ at 90°C for 30min and occasional vigorous shaking forming MLV with a diameter of 0.2-2.1 µm[20]. These MLV need to equilibrate for at least 8 h at 65°C before further use.

In the second step, MLV were processed into LUV by extrusion through a track etched polycarbonate membrane with 100 nm pore size. For the vesicles to be able to pass through the membrane, it is important to keep the temperature above the phase transition temperature of the respective lipid, so the extruder setup is placed into a heating block and heated to about 60°C. According to manufacturer's protocol (Extruder Set by Avanti Polar Lipids, Alabaster, Alabama,

USA), 11 passthroughs of the MLV solution through the membrane should yield LUVs with a narrow monodisperse size distribution around 100 nm.

3.8 Determination of apparent binding affinity of WGA-ICC

Half-maximum binding constants K_{50} (apparent binding affinity) of WGA-ICC to mucins were determined based on changes in ICCs mean fluorescence lifetime $\bar{\tau}$ in presence of mucin. The fractional saturation of mucin-binding is calculated by:

$$fractional\ saturation\ ([\mathrm{BP}]) = \left(\frac{\bar{\tau}_{pop}([\mathrm{BP}]) - \bar{\tau}_{pop,0}}{\bar{\tau}_{pop,max} - \bar{\tau}_{pop,0}}\right), \tag{33}$$

where $\bar{\tau}_{pop}$ is ICCs mean fluorescence lifetime (eq. (6)) at specific concentration of the binding partner [BP] mucin. $\bar{\tau}_{pop,0}$ is ICCs mean fluorescence lifetime in the absence of mucins and $\bar{\tau}_{pop,max}$ its lifetime at theoretical infinite mucin concentration an fully saturated binding[16]. K_{50} is obtained when plotting fractional saturation over ratio [BP]/[WGA-ICC] and fitted with the Hill-equation:

$$fractional\ saturation\ ([\mathrm{BP}]) = \frac{S \cdot [\mathrm{BP}]^n}{({K_{50}}^n + [\mathrm{BP}]^n)}, \tag{34}$$

where S is the saturation level of the binding process and n is the cooperativity factor. Binding experiments were carried out with murine colon mucus with fixed but unknown mucin concentration. This has the implications that [BP] is actually the concentration of WGA-ICC, fractional saturation is plotted over inverse WGA-ICC concentration and $\bar{\tau}_{pop,max}$ needed to be a fitting parameter. Also, since fractional saturation is normalized to 1, also the saturation level S needs to be fixed to 1.

3.9 Rotational viscometer

Viscosity measurements of bulk solutions of sucrose/water mixtures and mucin solutions were carried out on the PCE-RVI1 (PCE, Germany) rotational viscometer. For this purpose, a rotor is submerged into the solution and driven by a motor with constant rotational speed. The torque needed for the rotation is measured by a spring and converted into a viscosity value on a scale. To ensure accurate measurements, a cylindrical volume with 70 mm in diameter and 130 mm in height is needed with the rotor positioned in the center. Rotor size and rotational speed can be adjusted to capture a greater range of viscosity.

3.10 The fluorescence-EPR dual label

Synthesis of the dual-label was carried out in the Chemistry Department by the group of Prof. Calderón (FU Berlin, Germany). The four compounds shown in Figure 3-7, representing the final dual labels and its precursors, were handed for further analysis in the FLIM experiments.

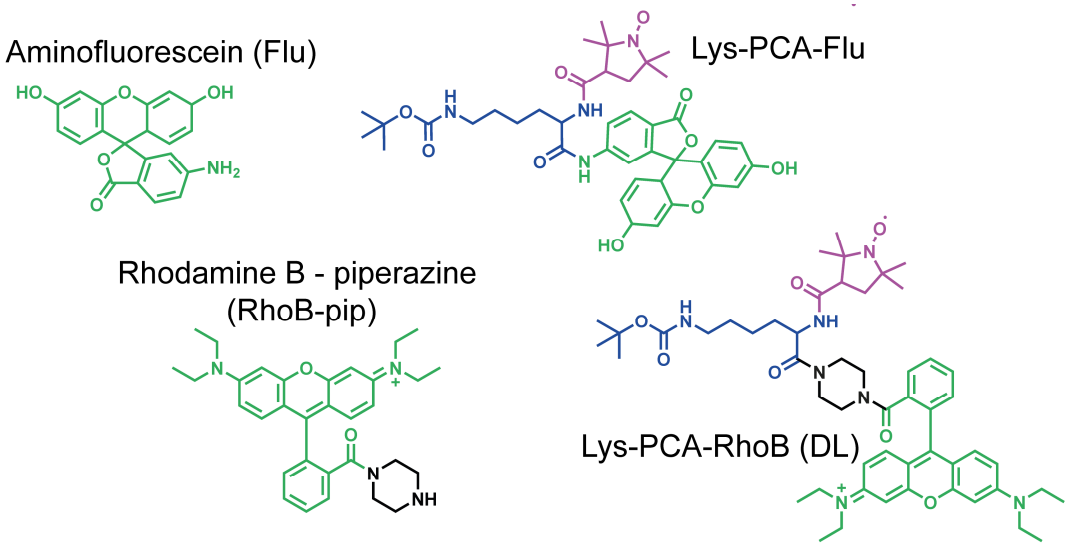

Figure 3-7. Structural formula of fluorescence-EPR dual labels based on 6-aminofluorescein and Rhodamine B (Rho B). The fluorescent label is depicted in green, the EPR label PCA in magenta and the tri-functional lysine linker in blue.

3.11 Partition coefficient (n-octanol/water) determination of RhoB and DL

The logP- value of RhoB and DL has been determined using the "shake flask method" according to OECD guideline 107[154]. Here, n-octanol and water need to be mutually saturated at room temperature. Mutually saturated water and octanol were mixed in the ratios 3:1, 6:1, and 3:2 in duplicate samples. RhoB and DL were dissolved in the octanol/water mixtures and were shaken for 2 h. Phase separation of octanol and water was achieved using a centrifuge at room temperature, 16.000 g for 20 min. The concentrations in both phases were determined by absorption spectroscopy. The LogP value is the decadic logarithm of the concentration ratio in both phases:

$$LogP = Log\left(\frac{c_{RhoB/DL}(octanol)}{c_{RhoB/DL}(water)}\right) \quad (35)$$

Molar extinction coefficients of RhoB and DL in 1-octanol and water have been determined by diluting RhoB or DL in ethanol, 1-octanol, and water from the same stock solutions, taking absorbance spectra each, and calculating $\epsilon_{OctOH/H2O} = \epsilon_{EtOH} * OD_{OctOH/H2O}/OD_{EtOH}$. ϵ_{OctOH}(RhoB)=

(99000±17000) M^{-1} cm^{-1}, ϵ_{H2O}(RhoB)= (85000±4000) M^{-1} cm^{-1}, ϵ_{OctOH}(DL)= (77000±5000) M^{-1} cm^{-1}, and ϵ_{H2O}(DL) = (64000±10000) M^{-1} cm^{-1}.

3.12 Skin sample preparation for dual label penetration

The utilization of human abdominal skin from healthy female (*n* = 3) and male (*n* = 1) volunteers undergoing plastic surgeries was approved by the institutional review board of Charité-Universitätsmedizin Berlin (EAI / 025/ 13). Informed written patient consent was obtained from all participants. Skin sample preparation was performed by Pin Dong of the AG Prof. Meinke at Charité Berlin. Excised human skin without injuries, scars or stretch marks was used within 24 h post-surgery. After removing subcutaneous adipose tissue and cleaning with PBS, the *stratum corneum* of skin samples was removed by performing cyanoacrylate skin surface stripping four times to obtained barrier-disrupted skin, as described here[155]. Subsequently, the DL solution (400 µM) in PBS-dimethylsulfoxid 95/5 (v/v) was applied to skin samples within an area of 1 × 2 cm^2 (20 µl/cm^2). Safety margins of 1 cm to the edge of the skin sample were left untreated to avoid lateral penetration. After 2 h exposure at 32°C in a humid chamber, supernatant on the skin surface was removed with cotton swabs and then a single tape stripping was performed to remove unabsorbed DL.

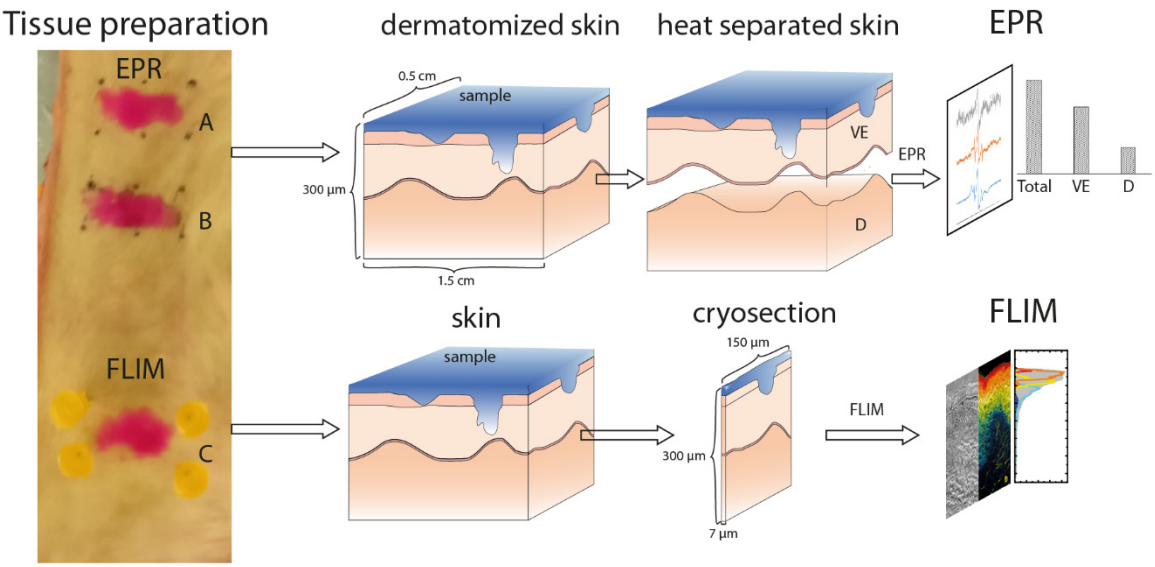

Figure 3-8. Preparations of skin biopsies for EPR and FLIM.

Three skin samples (A, B, and C) were prepared from each donor (Figure 3-8). Sample A and B were measured in the EPR spectrometer and C in FLIM. For sample A, the skin with a thickness of 300 µm (including viable epidermis and dermis, VE & DE) was obtained by using a dermatome (Aesculap®, Germany) and sized into 0.5 × 1.5 cm^2. For sample B, the VE of the skin sample (0.5 × 1.5 cm^2 in size) was separated by the heating method. Firstly, a piece of adhesive tape was applied onto the

skin surface and pressed under 8 N for 1 min. Then the skin biopsy was placed on a heating plate for 1 min at 60 °C. With the support of the tape, the VE was carefully separated from the DE by tweezers. For sample C, the skin sample were punched 6 mm in diameter, before frozen in liquid nitrogen and stored at -80°C until use. The biopsy was embedded in tissue freezing medium and cryo-sectioned into 7 µm thick slices from DE to VE. Four slices from each donor were obtained at intervals of about 100 µm. Besides, untreated skin samples were prepared for the control measurements of EPR and FLIM.

3.13 Loading of pH-sensitive nanoparticle and treatment of skin sections

Eudragit® L100 nanoparticles were prepared using the nanoprecipitation technique[156]. Loading of Eudragit® nanoparticles was done as described[157], yielding an average particle diameter of 786 nm. For penetration experiments of NR in glabrous skin, 100 µM of NR in aqueous solution was applied to skin with 20 µL/cm² and incubated for 30 min, 240 min, and 960 min at 32°C.

For follicular penetration experiments, a skin area of 2x3 cm was treated with 20 µL/cm² aqueous solutions containing 2% (w/v) Eudragit® L100 loaded with 50 µg/ml NR. The skin area was massaged for 2 min and followed by incubation for 30 min at 32°C.

3.14 Cell lines

3.14.1 HT29-MTX / Caco2

For measurements of the extracellular mucus layer HT29-MTX and Caco2 were cultured in the Lab of Prof. Marie Weinhart by Laura Elomaa. HT29-mtx is a colon carcinoma cell line treated with methotrexate, which now behaves like mucus-secreting goblet-cells found in the intestine[158]. Caco-2 is a cell line derived from large intestine carcinoma which's phenotype closely resembles the enterocytes in the small intestine[159]. Both cell lines are commonly co-cultured in efforts to produce a more physiological representation of the small intestine[160]. For our experiments, Monocultures of both cell lines as well as a 1:1 co-culture was produced. We additionally produced a set of cell cultures, which were cultured on a shaker at 60 rpm. The sheer stress introduced by the shaking are again meant to mimic physiological forces in the small intestine. Cells were seeded with a density of 6.4 x 10^4 cells/cm² into 35 mm Ibidi micro-dishes (81158, Ibidi, Germany) and cultured for 4 weeks before measurement. HT29-mtx were in passage 20 and Caco-2 were in passage 25. Culture medium during 4 week growth phase contained DMEM with GlutaMAX, phenol red, 4.5 g/l glucose and Pyruvate (31966021, Thermo Fischer Scientific, Germany), 10 % fetal bovine serum (S181B, Biowest, Germany), 1 % non-essential amino acid solution (M7145, Sigma-Aldrich, Germany) and 1 % Penicillin-Streptomycin solution (DE17-602E, Biozym Scientific GmbH, Germany). Directly prior to FLIM measurements and during incubation with ICC-labeled lectins the cell culture

medium was switched to DMEM +4.5 g/l glucose without phenol red (BE12-917F, Biozym Scientific GmbH, Germany), 10 mM HEPES (15630080, Sigma-Aldrich, Germany), 1 % GlutaMAX (100x) (35050061, Sigma-Aldrich, Germany), 10 % fetal bovine serum (S181B, Biowest, Germany), 1 % non-essential amino acid solution (M7145, Sigma-Aldrich, Germany) and 1 % Penicillin-Streptomycin solution (DE17-602E, Biozym Scientific GmbH, Germany). For experiments with triggered mucus discharge, 100 µM ATP was used (A6419, Sigma-Aldrich, Germany)[161]. During measurements, cell dishes were kept at a steady 37°C by a water heated brass plate.

3.14.2 Human oral keratinocytes and squamous cell carcinoma (SCC-25, UM-SCC-22B)

Human keratinocytes were cultured in oral keratinocyte medium. SCC-25and UM-SCC-22B cell lines were grown in DMEM/F-12 Ham medium, supplemented with 9% fetal calf serum, 0.9% L-glutamine, and penicillin/streptomycin. All cell lines were cultured at 37°C in a humidified atmosphere with 5% CO_2. The medium was changed three times a week, and cells were passaged after reaching confluency of 80%. Cell culture was performed according to standard operating procedures referred to good cell culture practice. From the cell cultures multi-layered tumor oral mucosa models were built[141]. The cells were cultured and built into tumor models in the lab of Prof. Schäfer-Korting (Institute of Pharmacy, FU Berlin, Germany). Cryosections after penetration experiments were handed over to me for analysis.

3.15 Murine mucus samples

Animal care and processing was handled by Kira van Vorst of the working group of Marcus Fulde (Veterinary Medicine, FU Berlin, Germany). Experiments were conducted with principles of “the three Rs” (Replacement, Reduction, and Refinement) in mind. Murine mucus samples from 10 male mice of the same litter were collected (approval G 0167/18). Mice were divided into two groups of 5 and treated with two combinations of antibiotics on the 6th and 7th day after birth with at least 24 h in between treatments. The first group was treated with Ampicillin (orally, 150 mg/kg) and Gentamicin (orally, 150 mg/kg), the second group received Meropenem (subcutaneous, 90 mg/kg) and Vancomycin (orally, 150 mg/kg). No probiotic was administered after antibiotic treatment. Small intestines, cecum and colon were immediately dissected and rinsed with PBS. Secreted mucus was removed with a cell scraper and collected in Eppendorf tubes. Samples were received for measurements from the group of Prof. Marcus Fulde and stored at -20°C between measurements.

3.16 Labeling of cetuximab with FITC

Cetuximab was labeled with fluorescein isothiocyanate (FITC) yielding Cetuximab-FITC. 1.7 mM FITC was added to 17 µM Cetuximab and allowed to incubate for 60 min in 100 mM sodium bicarbonate

buffer pH 9.5. Excess dye was removed by gel chromatography with Sephadex G25 (GE Healthcare, USA). For the determination of the labeling stoichiometry, the UV absorbance contribution of the FITC spectrum needs to be subtracted from the protein absorption peak at 280 nm of the FITC-labeled cetuximab. FITC contribution to absorbance at 280 nm was determined to be 43.1% (Figure 4-24B) of the total cetuximab-FITC absorbance at 280 nm. For the concentration determination of FITC and cetuximab, I used Lambert-Beers law (eq. (27)) with a cuvette diameter $d = 1\ cm$ and the molar extinction coefficients ε_{FITC}(495 nm)=73000 $M^{-1}cm^{-1}$ and $\varepsilon_{Cetuximab}$(280 nm)=200583 $M^{-1}cm^{-1}$. The labeling stoichiometry n of FITC and cetuximab can now be calculated by:

$$n = \frac{OD_{495}}{\varepsilon_{\mathrm{FITC}} * d} \Big/ \frac{OD_{280} - (OD_{280} * 0.431)}{\varepsilon_{\mathrm{cetuximab}} * d} \tag{36}$$

where $OD_{495/280}$ is the absorbance of the eluded fractions at 495 and 280 nm. The labeling stoichiometry of the main fractions F8 and F9 was determined to be about 6 FITC labels per cetuximab molecule (Figure 4-24C).

4 Results and Discussion

4.1 ICC as a nanoviscosity probe in cell membrane and native mucus

In the following chapter, I will use the fluorescent molecular rotor ICC, as the free dye or labeled to dPGS or WGA, to investigate the viscosity of various systems. Here, the fluorescence lifetime will be the primary read-out parameter. Hence, I want to start by introducing a basic characterization of the fluorophores absorption and emission features (Figure 4-1 and Table 2). Note, the ICC fluorescence lifetime in aqueous solution is very short with ~150 ps (Table 2). I will also use the opportunity to assess the precision of the fit algorithm used to determine the fluorescence decay components and by extension the mean fluorescence lifetime of the fluorophores in different environments. For this purpose, I executed an exhaustive error analysis (chapter 3.5.2) of the decay curves shown in Figure 4-1. The results are shown in Figure 4-1E, G, and I, yielding the confidence intervals for the fit values shown in Table 2. Note that the relative errors are very low, which indicate very high precision of the fit algorithm. For simplicity, I will perform repeated fits of the same fluorescence data to evaluate the fitting error instead of the exhaustive error analysis in future analysis. In order to fully assess the accuracy of my measurements, I would need to average repeated independent measurements. Due to scarcity of sample material or uniqueness of the experiment, repetition of the measurements was not always possible.

Table 2. Exhaustive error analysis of the fit of the fluorescence decay of ICC, dPGS-ICC, and WGA-ICC measured in the TCSPC cuvette setup (Figure 4-1). $\alpha_i(\%)$ are relative amplitudes, $\tau_i(\mathrm{ns})$ are the respective fluorescence lifetime components, and χ^2_{red} is the reduced chi square of the fit. Experimental conditions: ICC and dPGS-ICC measured at 20°C, WGA-ICC at 37°C, λ_{ex}=488 nm, λ_{em}>515 nm.

Sample	$\boldsymbol{\alpha_1}(\%)$	$\boldsymbol{\alpha_2}(\%)$	$\boldsymbol{\alpha_3}(\%)$	$\boldsymbol{\tau_1}(\mathrm{ns})$	$\boldsymbol{\tau_2}(\mathrm{ns})$	$\boldsymbol{\tau_3}(\mathrm{ns})$	$\boldsymbol{\chi^2_{red}}$
ICC	50.1 ±1.9	49.9 ±2.5		0.097 ±0.004	0.180 ±0.004		0.6
dPGS-ICC	55.1 ±0.8	37.9 ±1.2	7.0 ±0.5	0.124 ±0.005	0.374 ±0.014	0.996 ±0.023	0.8
WGA-ICC	95.9 ±0.2	3.9 ±0.4	0.17 ±0.01	0.147 ±0.001	0.453 ±0.019	3.156 ±0.106	2.3

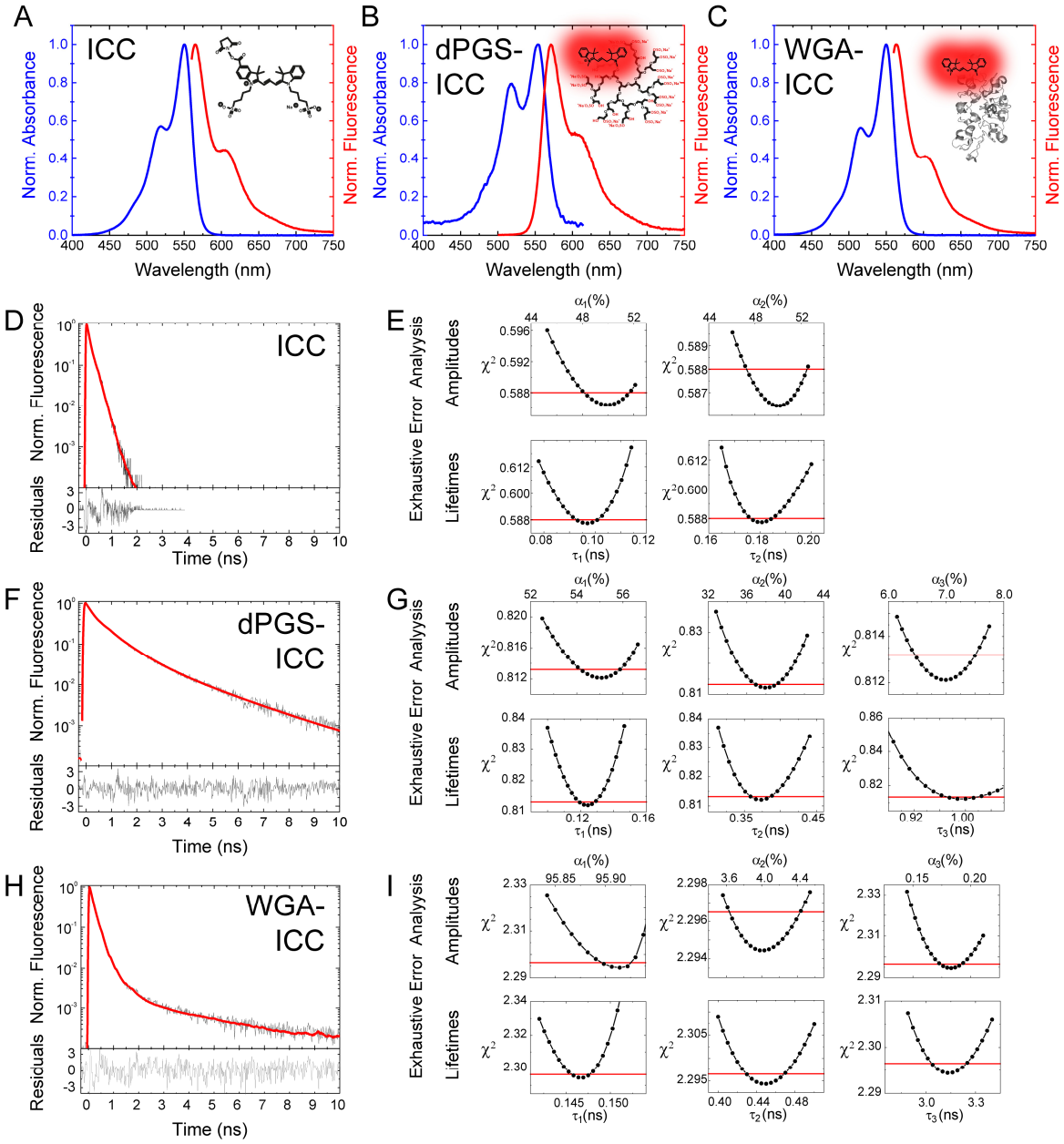

Figure 4-1. Characterization of the fluorescent molecular rotor ICC. (A-C) Normalized absorbance (blue) and emission spectra (red) of the free dye ICC (A) and labeled to dPGS (B) or WGA (C). (D, F, H) Fluorescence decay of the three compounds in water measured in the TCSPC cuvette setup. ICC and dPGS-ICC at 20°C, WGA-ICC at 37°C. TCSPC data in grey, multi-exponential fit of the data in red. The residuals of the fit are shown below. Fit values are presented in Table 2. (E, G, I) Exhaustive error analysis of the fits shown in (D), (F), and (H) respectively. This analysis yields the error of the fits for each parameter (Table 2). The line in red marks a confidence interval of 1 σ (64.8%). Experimental conditions: λ_{ex}=488 nm, λ_{em}>515 nm.

4.1.1 Interaction of dPGS-ICC with spin-labeled lipids in MLV to facilitate sensing of lipid phase transitions and nanoviscosities in lipid membranes

In living cells, membrane viscosity is tightly regulated by a complex lipid composition, incorporating fatty acids of varying chain length and different stereochemical properties. Cholesterol further stabilizes the membrane and prevents phospholipids from clustering. Homeostasis of those physical properties is imperative for proper function of membrane bound proteins and facilitates vesicle mediated transport through the cell. Naturally, various diseases are linked to an altered membrane fluidity and lipid phase transitions[6,7]. In addition, many viruses, drugs but also nanoparticles have been found to affect membrane fluidity[8-12]. To advance research in these topics it is essential to characterize any effects on membrane fluidity. Therefore, in this section, we were interested in developing the means to investigate membrane viscosity of biological samples.

Fluorescence techniques have been extensively used to report on membrane viscosity. Besides fluorescence depolarization, fluorescence recovery after photobleaching and fluorescence correlation spectroscopy[24-26] also the excited state lifetime of fluorescent molecular rotors, can be used to elucidate dynamic properties of lipid membranes. We chose the fluorophore ICC (also known as Cy3) as it is part of the family of molecular rotors, which generally dissipate energy of their excited electronic state into intramolecular twisting around their methine linker but will populate a radiative pathway of deexcitation (i.e. fluorescence) as this twisting motion is sterically hindered or impeded in a highly viscous solvent. Kai Licha (AG Prof. Haag, FU Berlin, Germany) coupled this fluorophore to a small dendritic polyglycerol sulfate nanoparticle (dPGS), which was previously characterized in terms of nanodynamics, size, liver localization, serum protein as well as lipid membrane interaction[16,162,163]. The final construct dPGS-ICC was provided by the AG Haag for us to further analyze. It was originally introduced as an inflammatory inhibitor[144,162,164], so in this work we extend its pharmaceutical properties by a reporting functionality.
Before the fluorescence molecular rotor probe can be used to measure membrane viscosity, I needed to determine where exactly the ICC is located in relation to the lipid membrane. Since the molecular rotor will only probe viscosity in its immediate surrounding, I needed to make sure, that it is indeed properly embedded into the membrane in order to measure its viscosity.

The membrane association of dPGS-ICC can be gathered from Figure 4-2A. While free ICC doesn't seem to interact with any vesicles in the solution and won't show a significant change in its fluorescence decay, dPGS-ICC on the other hand stains the vesicles shown in the FLIM images shown and in addition exhibits a considerable longer fluorescence lifetime when found in the vesicles.

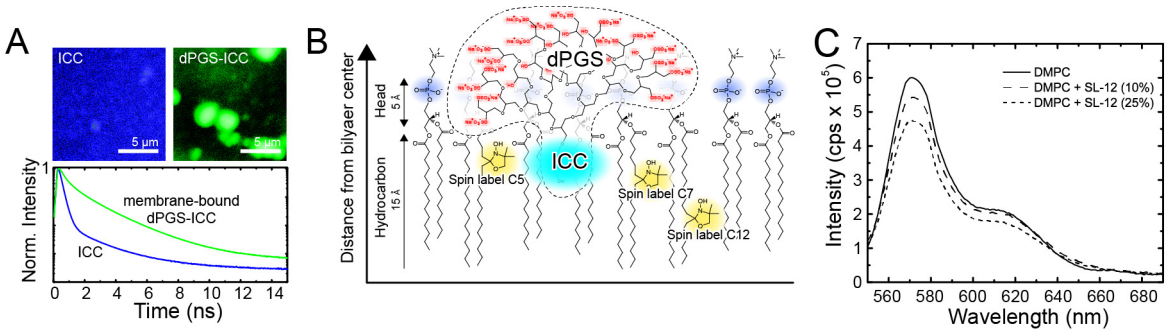

Figure 4-2. Membrane interaction and incorporation of dPGS-ICC (A) comparison of ICCs and dPGS-ICCs fluorescence decay in presence of lipid vesicles, false color images according to decay curves shown below (B) Proposed intercalation scheme of dPGS-ICC into the lipid bilayer based on results from quenching analyis of the parallax method [43] using spin-labels at carbon position 5, 7 and 12 of the fatty acid tail. (C) Quenching of dPGS-ICCs fluorescence intensity in DMPC MLV with 10% and 20% spin-labeled phospholipids (C12).

Hence, Figure 4-2A shows that dPGS facilitates ICC binding to lipid vesicles. To assess the insertion depth of ICC into the bilayer, I employed the parallax method by Chattopadhyay and London (chapter 3.6)[43]. Here, I observed dPGS-ICCs fluorescence intensity when interacting with DMPC LUV doped with spin-labeled DMPC. I considered 3 different samples of DMPC vesicles, each including spin-labels at one of three different labeling sites of the carbon chain of DMPCs fatty acid residues (i.e. C5, C7 or C12; see Figure 4-2B). Quenching of ICC fluorescence intensity in presence of the spin-labels at different depths then allows the determination of ICCs relative position according to eq. (22). I also varied molar ratio of spin-labeled lipids to modulate this effect (Figure 4-2C). We found an average distance of 11.9 ± 3.2 Å from the bilayer center (average of 2 independent experiments with 3 data points for each of the three spin-labeled lipids). Structural data for DMPC membranes suggest a total thickness of 30 Å for the hydrocarbon region and 5 Å[44]. So, the ICC label will be located about 3 Å below the polar headgroups, and hence will report local viscosity of the upper lipid tail region. In this picture, the flexible structure of the dPGS dendrimer most likely will reorient itself such that its charged end-groups will interact with the polar lipid head region (see Figure 4-2B).

But before this dPGS-ICC conjugate can be used in biological membranes, the relationship between its mean fluorescence lifetime and the viscosity of its immediate environment, the nanoviscosity of the solvent, must be determined. This work was done by Katja Ober (Bachelor thesis, AG Alexiev, FU-Berlin, Germany) and is shown in Figure 4-3. Solutions of varying viscosity were produced by different temperatures and sucrose-water mixtures.

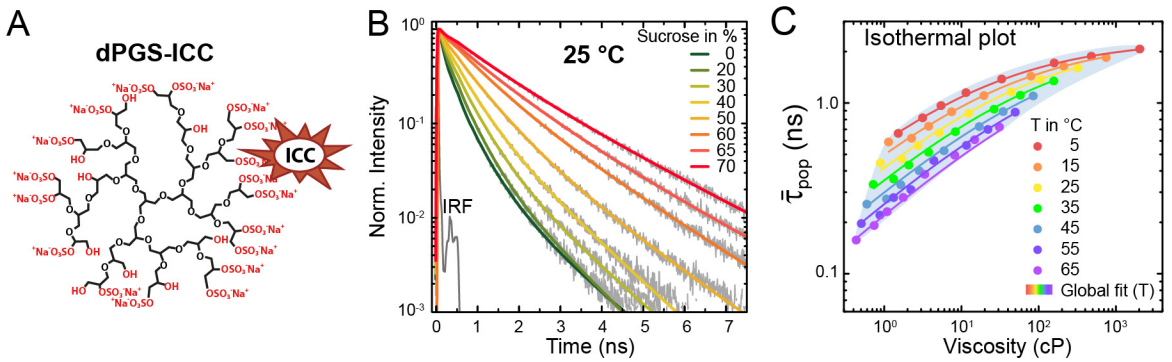

Figure 4-3. Viscosity calibration of dPGS-ICCs fluorescence lifetime (A) structural formula of dPGS-ICC (B) fluorescence decays of dPGS-ICC at 25 °C for varying sucrose-water mixtures, experimental data in grey, multiexponential fits in colored lines, IRF: Instrument response function (C) Förster-Hoffmann plot of dPGS-ICCs mean fluorescence lifetime as a function of viscosity achieved by different sucrose-water mixtures and temperatures. Viscosity values of the sucrose/water-mixtures were taken from [36]. Temperature dependent global fit according to eq. (16). Experimental conditions: 0.3 µM dPGS-ICC, Excitation: λ_{ex} = 486 nm, Emission filter: λ_{em} > 570 nm. Experiments by Katja Ober.

Time-resolved fluorescence of dPGS-ICC in those solutions was recorded in our TCSPC cuvette setup and each decay was fitted with the sum of three exponentials (eq. (5)). The mean fluorescence lifetime was calculated according to eq. (6) and plotted over solution viscosity in a Förster-Hoffmann plot (Figure 4-3C). Global analysis of the viscosity and temperature dependent mean fluorescence lifetime was accomplished by fitting each isothermal data set in Figure 4-3C with eq. (16). Besides α, also the activation energy E_α is a fitting parameter and was determined to be $E_\alpha = (15.5 \pm 0.3)\ kJ/mol$, which is on the order of what was found in the literature for ICC attached to DNA ($6 - 14\ kJ/mol$)[165]. Note that the slope of the isothermal plots shown in Figure 4-3C significantly flattens in the range of 1000-2000 mPa s, meaning that the fluorescence lifetime only slightly changes despite significant viscosity increase. Thus, this viscosity sensing probe is most reliable in the region of 0.1-1000 mPa s.

We now go on and explore dPGS-ICCs capabilities in detecting subtle changes in membrane composition and fluidity. As a first example, we looked at DOPC vesicles with varying cholesterol content. As mentioned earlier, cholesterol is one of the main pathways for a cell to regulate membrane fluidity and should be a major focus point for any study regarding pathologic changes is membrane composition. As shown in Figure 4-4A, dPGS-ICC reliably reported a significant increase in fluorescence lifetime of $\bar{\tau}_{pop,90:10} = 0.54\ ns$ to $\bar{\tau}_{pop,80:20} = 0.99\ ns$ caused by an increase in cholesterol content by only 10%.

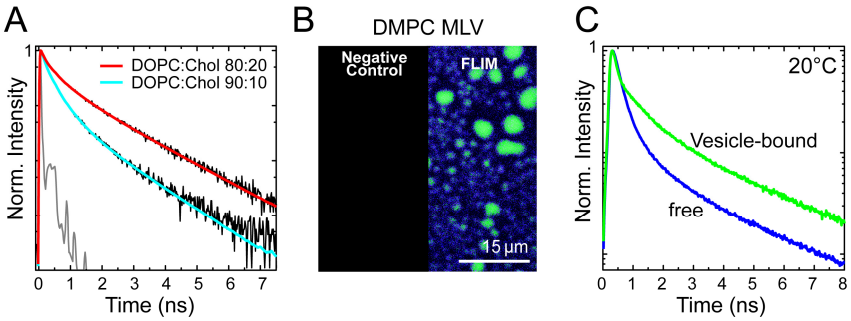

Figure 4-4. Sensitivity of dPGS-ICC to changes in membrane fluidity (A) Fluorescence decay curves of 0.8 µM dPGS-ICC at 22°C in DOPC:Chol 90:10 and DOPC:Chol 80:20 vesicles measured in the cuvette setup (B-D) 0.1 µM dPGS-ICC interacting with DMPC MLV (B) confocal microscopy images of dPGS-ICC in MLV, false color image according to the two distinct fluorescnece decay clusters shown in (C). Experimental conditions: λ_{ex}=530 nm, emission filter: λ_{em} > 570 nm**.** Measurements and data analysis of dPGS-ICC in DMPC MLV were performed in cooperation with Pierre Volz-Rakebrand. Figure adapted [20].

Confident in dPGS-ICCs proper membrane incorporation and its potential to detect local nanoviscosity, we started to investigate membrane fluidity in DMPC MLV and their temperature driven phase transition from the gel- to the liquid disordered phase. Results are shown in Figure 4-4B-C. The measurements and data analysis of dPGS-ICC in DMPC MLV was done in cooperation with Pierre Volz-Rakebrand (AG Alexiev, FU-Berlin, Germany). In FLIM images (Figure 4-4B), membrane bound dPGS-ICC (green) can easily be discriminated against background fluorescence of free dPGS-ICC (blue) by its significantly increased fluorescence lifetime (Figure 4-4C). In contrast to conventional ensemble measurements in cuvettes, we are now free to only look at the relevant lipid viscosity sensing fraction of our reporting nanoparticle. dPGS-ICC time-resolved fluorescence in DMPC MLV was recorded at temperatures ranging from 5 °C to 45 °C and mean fluorescence lifetime of the green decay cluster were converted into apparent viscosity based on the temperature resolved viscosity calibration (Figure 4-3C) and plotted over inverse temperature in an Arrhenius plot[20]. The phase transition at 24 °C is nicely reproduced. While we see a considerable heterogeneity in the reported viscosities below the phase transition temperature corresponding to 1000-92 mPa s, we see a near perfect linear dependence above 24 °C. We find 92-40 mPa s in the liquid-disordered phase of DMPC MLV, well in accordance to previous publications which used BODIPY as molecular rotor[34].

Finally, we used dPGS-ICC to spatially resolve membrane domains of different viscosity inside of living HeLa cells in the FLIM setup. For this purpose, HeLa cells were incubated with dPGS-ICC dissolved in PBS for 15 min at 37 °C. Results of FLIM measurements are shown in Figure 4-5. We found two distinct lifetime cluster (cyan and yellow) which can be assigned to distinct

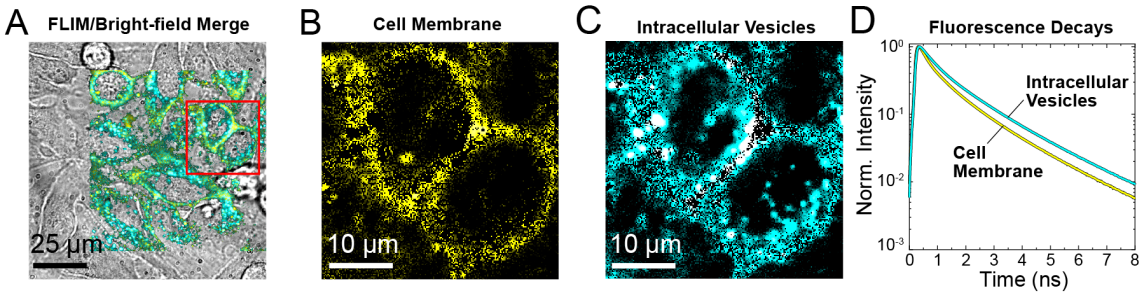

Figure 4-5. FLIM images of HeLa cells incubated with dPGS-ICC for 15 min at 37°C. (A) Overlay of fluorescence data with brightfield image (B,C) Two distinct membrane domains i.e. the outer cell membrane (B) and intracellular vescicles (C) characterized by unique fluorescnence decay signatures (yellow and cyan respectively) (D) Fluorescnence decays found in HeLa cells. Experimental conditions: λ_{ex}=530 nm, emission filter: λ_{em} > 570 nm. Figure adapted from [20].

morphological features reasonably well. While the faster fluorescence decay (yellow cluster, Figure 4-5B) is found predominantly in the outer cell membrane, a slightly higher viscosity in the intracellular vesicles is signaled by the slower cyan decay cluster (Figure 4-5C). The mean fluorescence lifetime in HeLa cell membranes was determined to be $\bar{\tau}_{pop} = 1.37\,ns$ (yellow cluster) and $\bar{\tau}_{pop} = 1.54\,ns$ (cyan cluster), which would translate to an apparent nanoviscosities of 187 mPa s and 404 mPa s respectively.

In this study, we looked at the nanoparticle dPGS, which was previously shown to reduce inflammation by binding to P- and L-selectin of leukocytes and the endothelium. We expanded the therapeutic properties of dPGS by covalently attaching the molecular rotor ICC which adds the capability of sensing local viscosity. Viscosity calibration of ICCs fluorescence lifetime was done in mixtures of sucrose and water at different temperatures from which also a temperature dependency of the lifetime-viscosity relation emerged (Figure 4-3C). This behavior can be modelled by the assumption that the proximity of dPGS to ICC introduced a higher activation energy for the photoisomerization, which we determined to be $E_\alpha = (15.5 \pm 0.3)\,kJ/mol$, comparable to ICC attached to DNA $(6 - 14\,kJ/mol)$[165]. The calibration curve was used in later studies where we analyzed temperature driven viscosity changes in lipid membranes of DMPC MLV and live HeLa cells[20].

We acknowledge that, regarding the fact that ICC is charged and the nanoparticle dPGS is hydrophilic, it seems counterintuitive that the dye will be incorporated into the lipid bilayer and report local nanoviscosity of the membrane. But recent studies have shown that dPGS-ICC clearly accumulates in the membrane of giant unilamellar vesicles[162] and that it is not at all uncommon for charged fluorophores to strongly interact with lipid membranes[166]. In order to accurately pinpoint

exactly what region of the lipid bilayer we are monitoring, we determined insertion depth of ICC into DMPC membranes via its fluorescence quenching in the presence the spin-label doxyl, covalently bound to the fatty acids at different depths. We found ICC to be located 11.9 Å from the bilayer center, corresponding to about 3 Å below the polar head groups, inside of the hydrophobic core of the bilayer. Thus, viscosity values reported by dPGS-ICC will refer to the upper lipid tail region.

In MLV, we found the phase transition temperature $T_c = 24\ °C$ of DMPC impeccably reflected in our data with viscosity values matching previous findings[34,167]. High heterogeneity in viscosity below phase transition lends support to the idea of coexistence of multiple lipid domains of different viscosity, each undergoing cooperative phase transition individually until above T_c all domains fuse to form a homogenous liquid disordered phase [10,167,168], which is in agreement with the near perfect linear trend at $T > 24\ °C$ in our Arrhenius-plot.

With this coherent data from DMPC-MLV, we had confidence in dPGS-ICCs as mentioned earlier, cells generally adjust membrane fluidity by cholesterol levels and lipid composition to be constant for optimal function. Hence, for the physiologically relevant case, one wouldn't expect significant variety in membrane fluidity among one cell type. Nonetheless, membrane fluidity is one of the defining features in tumor development, where higher fluidity tends to have a worse prognosis. In literature, we find for HeLa cell membrane viscosity values of 155 and 331 mPa s, determined by steady-state fluorescence anisotropy of DPH (diphenylhexatriene)[169] and photoisomerization of BODIPY[170]. In SK-OV3 cells, an ovarian cancer cell line, one study also used BODIPY to determine viscosity values of 20-450 mPa s [35,171]. Since we found 187 mPa s in the outer membrane, we are in good agreement with previously found values. The higher intracellular membrane viscosity of 404 mPa s might well be explained by a higher surface curvature of the small vesicles and not per se be a morphological feature necessary to facilitate cell function. We also must acknowledge that literature as well as our findings display a large variety in viscosity values in cell membranes, especially when compared to well defined lipid vesicles, comprised of only one lipid species. Of course, living cells are a much more complex system and a certain margin for differences are to be expected. But it also shows the need for further development of viscosity sensing methods to reduce any additional uncertainties in order to paint a more comprehensive picture of cellular membrane fluidity in physiological conditions and in particular for pathological cases.

4.1.2 Characterization of ICC excited state parameters and lifetime calibration for the complex mucus viscosity

This Results chapter describes the work we have done to elucidate the nanoviscosity of mucus *in vivo*. Biological samples were obtained from AG Prof. Weinhart (Chemistry Department, FU Berlin, Germany) and Prof. Fulde (Department of Veterinary Medicine). I start with briefly introducing mucus and which factors contribute to the viscoelastic properties of mucus as well as the importance of the knowledge over these factors in health and disease. In the Fundamentals section (chapter 2), one can find a detailed description of mucus, its production in the organism, and its constituents.

Cells in the airway, gastro-intestinal tract, and urogenital system, among others, produce mucus with a multitude of functions. The mucus layer facilitates the exchange of gases and nutrients while protecting against pathogens and mechanical insult, provides lubrication and prevents dehydration. All of those tasks put a range of demands on the viscoelastic qualities of the mucus layer. The details on how the mucus can combine all these seemingly contradictory properties are poorly understood.

In the healthy state, the characteristics of mucus is determined by a list of factors. The mucin mesh itself plays a big role due to its degree of entanglement and crosslinking but also the inter mesh solvent as well as secondary polymers like DNA and other proteins affect the viscosity (Figure 4-6). In the disease case, the presence of pathogens, cellular debris and upregulation of atypical mucins additionally complicate the situation, multiplying the current lack of understanding such as in the case of the lung disease cystic fibrosis[172].

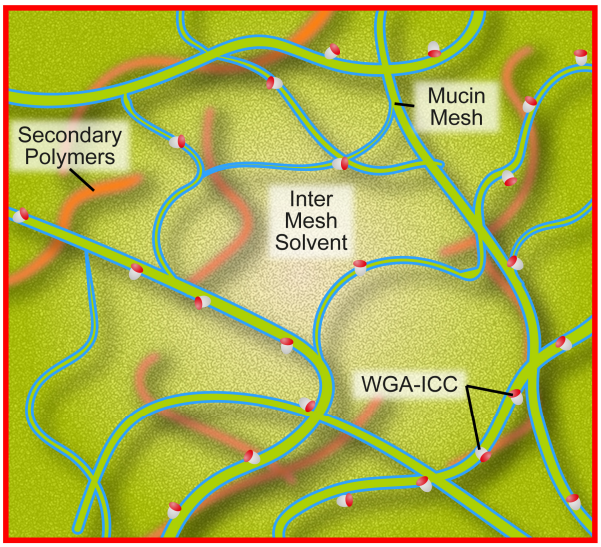

Figure 4-6. Structures of mucus that affect viscosity in the mucus layer. In addition, the location of the nanoviscosity probe WGA-ICC in the mucus is indicated (see text).

The goal in this chapter is to directly determine the spatially resolved viscosity properties of mucus attached to living cells. Usually, bulk samples are used to assess the viscosity of mucus by techniques such as rotational rheometry, cone-plate rheometry, capillary rheometry, particle tracking rheometry and magnetic microrheometry[173]. Since the measurements of bulk samples often fail to replicate the *in vivo* complex mucus network, I utilized the nanosized fluorescence molecular rotor ICC to investigate the spatial distribution of mucus viscosity in living cells using FLIM. To attach ICC directly to the mucus mesh, wheat germ agglutinin (WGA) labeled with ICC was used, since WGA has a high affinity to the o-glycan sidechains and sialic acids of the mucins[145] (Figure 4-6).

To clarify the different usage of the terms macroviscosity, microviscosity, and nanoviscosity, we define these terms as follows. The macroviscosity is the bulk viscosity as determined by e.g. rotational viscometer. The microviscosity is determined from microsized tracers as usually in microrheology. The nanoviscosity is the viscosity sensed by a small nanosized probe. Thus, for homogeneous small molecule solutions, such as sucrose, nanoviscosity as measured by the nanoprobe is equal to the macroviscosity. However, for complex samples such as mucus, the situation will be different[13].

In the following, I will first present the methodology how to determine viscosity from Förster-Hoffmann plots (eq. (13)) using ICC. From that, I will deduce which viscosity domain is accessible in the complex mucus system using the fluorescence molecular rotor ICC, i.e. nano-, micro-, or macroviscosity. Then I will show the viscosity gradient in the mucus layer on live cells from FLIM measurements, followed by the evaluation of the mucus viscosity alteration due to bacterial challenge in the digestive tract of mice.

Traditionally, when using fluorescence molecular rotor dyes, viscosity is determined from a plot of the fluorescence lifetime of the fluorophore vs. the bulk viscosity as measured by e.g. a rotational viscosimeter yielding the Förster-Hoffmann plot (eq. (13)) as a calibration curve. Here, sucrose (or similar homogeneous small molecule) solutions at varying temperatures and concentrations were used for viscosity calibration. Mucus is known to form heterogeneous gels comprising areas with a pore size of few hundred nanometers but also voids with several micrometers in diameter[174,175]. To mimic the complex mucin microenvironment for viscosity calibration and to decouple all the contributions to its viscosity, it is necessary to separately address the influence of the inter mesh solvent, the mucus mesh, and secondary polymers (Figure 4-6).

While the rigidity of the polymer mesh predominantly affects the macroscopic viscoelastic properties of the mucus, the nanoscopic viscosity encountered by the viscosity sensor probe WGA-ICC in a mucin network will be dictated by both the flexibility of the o-glycans of the mucins it is

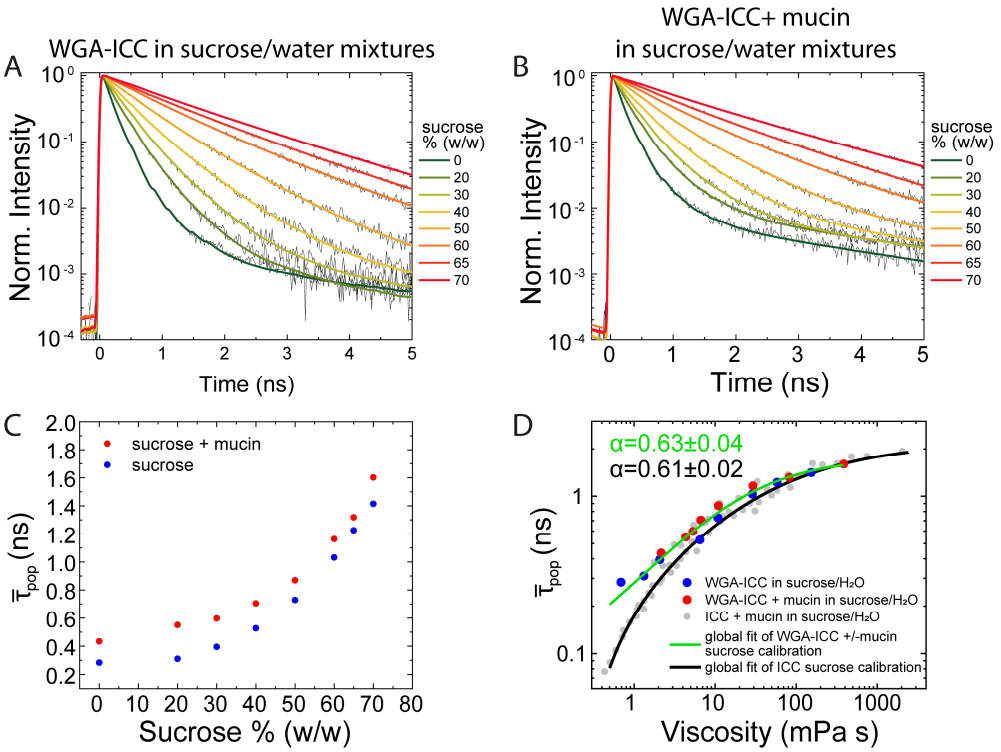

Figure 4-7. Influence of viscosity changes and mucin binding to WGA-ICC's fluorescence lifetime. (A) Fluorescence decays (gray lines) and multiexponential fits (colored lines) of WGA-ICC in different sucrose/water-mixtures (B) Fluorescence decays (gray lines) and multiexponential fits (colored lines) of WGA-ICC in different sucrose/water-mixtures with added 1 mg/ml mucins each. Fit values for (A) and (B) are summarized in Table A2 (C) Mean fluorescence lifetime of WGA-ICC in the solutions shown in (A) and (B), determined by eq. (6). (D) Förster-Hoffmann plots, showing the dependency of the mean fluorescence lifetime ($\bar{\tau}_{pop}$) on viscosity. A global Förster-Hoffmann fit (eq. (16)) was used to fit ICCs and WGA-ICCs fluorescence lifetime in dependence of bulk viscosity (green and black line); the obtained slopes (α) are indicated. Lifetime dependency of ICC (grey dots) on bulk viscosity are shown for comparison. Decay curves were recorded in the TCSPC cuvette setup: λ_{ex}=488 nm, λ_{em}>515 nm, T=37°C.

attached to and the viscosity of the inter mesh solvent. To investigate the contribution of the inter mesh solvent viscosity, the solvent molecules causing the increase in viscosity should be small, i.e. similar in size in comparison to ICC, so the experienced viscosity will be homogenous. Hence, the influence of solvent viscosity and binding to mucins on the excited state lifetime of WGA-ICC is calibrated using sucrose/water mixtures (sucrose molecular weight = 342 Da) with and without the presence of 1 mg/ml mucin type II (obtained from Sigma-Aldrich, Germany) (Figure 4-7). The presence of mucin mimics the natural location of WGA-ICC in mucus samples.

Viscosity of the calibration solutions was determined by a rotational viscometer (Figure A1A). Solutions with 30 % sucrose content and below had too low viscosities for accurate reading on the viscometer and where thus taken from [36].

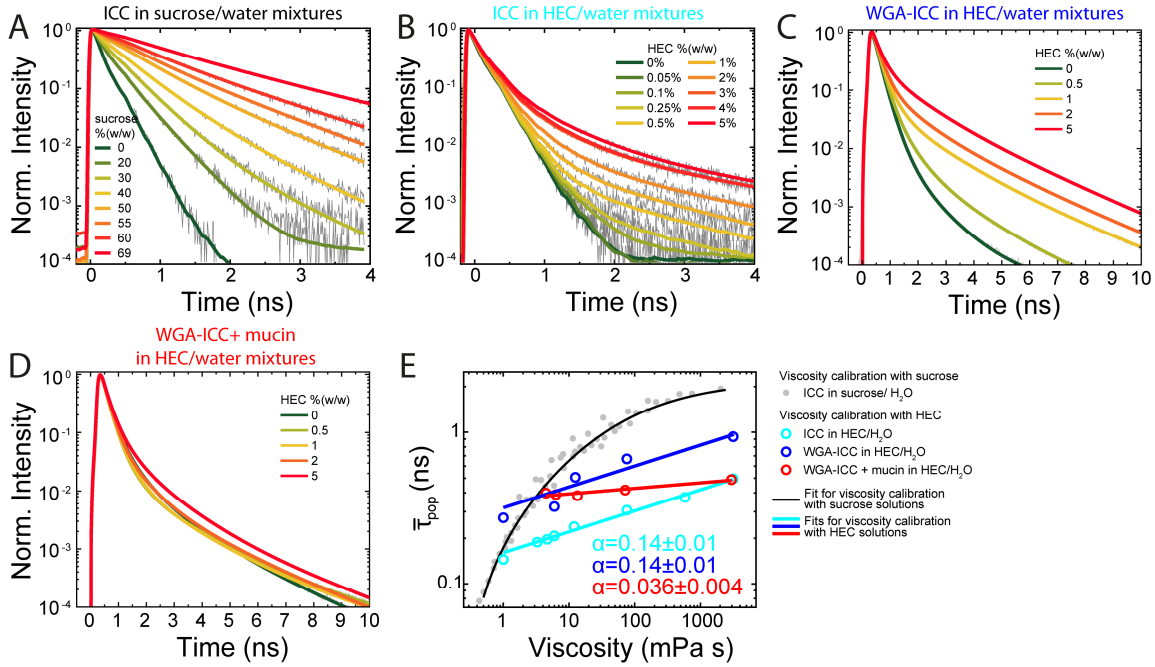

Figure 4-8. Influence of viscosity changes and mucin binding to WGA-ICC's fluorescence lifetime. (A) Fluorescence decays (gray lines) and multiexponential fits (colored lines) of ICC in different sucrose/water-mixtures (B) Fluorescence decays (gray lines) and multiexponential fits (colored lines) of ICC in different HEC/water-mixtures. (C) Fluorescence decays (gray lines) and multiexponential fits (colored lines) of WGA-ICC in different HEC/water-mixtures. (D) Fluorescence decays (gray lines) and multiexponential fits (colored lines) of WGA-ICC in different HEC/water-mixtures with 1 mg/ml mucin added. ICC was measured in the TCSCP cuvette setup, WGA-ICC in the FLIM setup. Fit values for (A-D) are summarized in Table A3 and Table A4. (E) Förster-Hoffmann plots, showing the dependency of the mean fluorescence lifetime ($\bar{\tau}_{pop}$) on viscosity. A global Förster-Hoffmann fit (eq. (13) and (16)) was used to fit ICCs and WGA-ICCs fluorescence lifetime in dependence of bulk viscosity; the obtained slopes (α) are indicated. Experimental conditions as indicated in Table A3 and Table A4.

The fluorescence lifetimes measurements of WGA-ICC in solutions with increasing sucrose content were conducted in the cuvette TCSPC setup and show a steady increase of WGA-ICC's fluorescence lifetime in dependence of solvent viscosity (Figure 4-7A,C), similar to dPGS-ICC's behavior (Figure 4-3). As one can see by comparing Figure 4-7A and B, WGA-ICCs mean fluorescence lifetime is consistently higher in the presence of mucins (Figure 4-7C), but since also the bulk viscosity is increased by the mucins, the Förster-Hoffmann plot (Figure 4-7D) appears identical with or without mucins present. But most importantly, WGA-ICCs fluorescence lifetime is not responding differently to the increased viscosity regardless of whether or not it is bound to mucins or rather if the viscosity increase is caused by the sucrose or the mucins. Both data sets have been fitted together globally with eq. (16), which resulted in a slope of $\alpha = 0.63 \pm 0.04$.

The second major contribution to a holistic picture of mucus viscosity properties are the mucins themselves, i.e., WGA-ICCs interaction with the mucin protein backbone forming a mesh. To

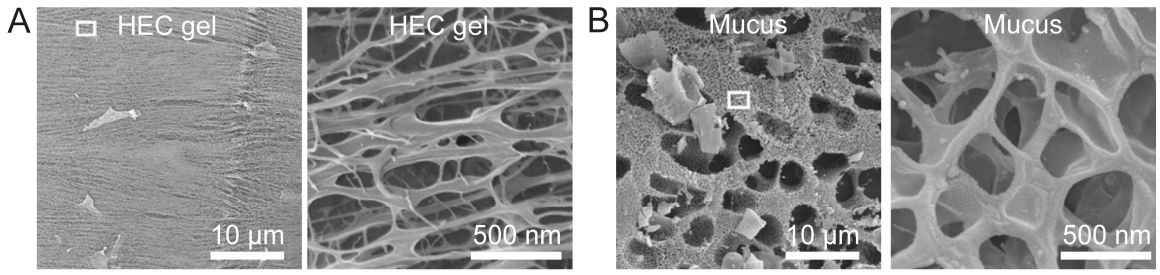

Figure 4-9. Representative cryo-SEM images of HEC gel (A) and mucus (B) While similarities in structure and pore size can be found on the nanoscale, mucus presents itself much more heterogenous than HEC-gel on the microscale. Permission for reprint of these images was kindly granted by PNAS [175].

account for these phenomena, a second calibration is necessary. For this purpose, I investigated fluorescence lifetime response of ICC and WGA-ICC to an increased viscosity, achieved by increasing hydroxyethyl cellulose (HEC) content in water (Figure 4-8). HEC forms hydrogels with mesh sizes depending on concentration (Figure 4-9). Here, the mesh of the HEC hydrogel as well as the inter mesh solvent contribute to the macroscopic viscosity. HEC solutions have been used as a reference hydrogel in the literature to investigate the movement of particles through mucus[175]. The pore size of HEC gels as well as their elastic and viscous modulus can be tuned to fit these parameters found in mucus (Figure 4-9)[175], for a deeper understanding of the natural situation in mucus. Though, it has been suggested that an observed discrepancy in particle mobility in mucus and HEC gel might result from a difference in rigidity of the polymer scaffold.

In my results, the most interesting feature is the different viscosity dependence of WGA-ICC in sucrose and HEC gels. In contrast to the steep curved global fit of ICC in sucrose (Figure 4-7D) , the fluorescence lifetime of ICC in dependence on HEC concentration, i.e. bulk viscosity, shows a linear behavior (eq. (13)) with a reduced slope of $\alpha = 0.14 \pm 0.01$ compared to $\alpha = 0.61 \pm 0.02$ of ICC in sucrose solutions (Figure 4-8A,B,E). Note that in Figure 4-8E, the viscosity of ICC in aqueous sucrose solution was determined from the bulk viscosity of sucrose solutions, while the viscosity in aqueous HEC solutions was determined from bulk viscosity of HEC solutions. The comparison to the ICC Förster-Hoffmann plot in sucrose solution clearly shows a deviation from the 2/3 power viscosity dependence from the Förster-Hoffman equation for an intermediate viscosity range in homogeneous solutions[38]. Similar results were obtained for WGA-ICC in aqueous HEC solutions with an $\alpha = 0.14 \pm 0.01$ (Figure 4-8C,E). I would like to point out that ICC exhibits a substantially faster fluorescence decay in aqueous HEC solutions (Figure 4-8B, E (cyan curve)) than in aqueous sucrose solutions with identical bulk viscosity (Figure 4-8A, E (black curve)). This behavior can be used to describe the different viscosity domains in the HEC gels (Figure 4-10), i.e., the inter mesh solvent constituents and the contribution of the mesh to the hydrogel.

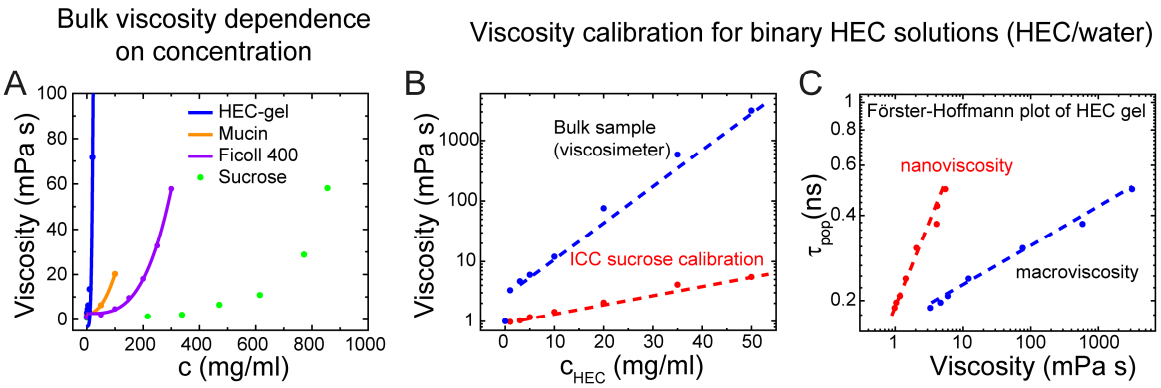

Figure 4-10. (A) Bulk viscosity dependence of viscogenic compounds in aqueous solution on concentration. Viscosity for HEC-gel (blue), porcine gastric mucin (orange) and sucrose (green) where measured in our rotational viscosimeter, viscosity of Ficoll400 solutions was taken from [37]. Viscosity calibration for binary HEC solutions (B) the viscosity of aqueous solutions with increasing HEC concentration determined with a rotational viscosimeter (black line, macroviscosity) and based on the sucrose calibration of the fluorescence lifetime of ICC (red line, nanoviscosity). (C) Förster-Hoffmann plot of ICC in HEC gel based on the nanoviscosity (red) and macroviscosity (blue). Please note, (C) depicts a region of interest for ICC data described in Figure 4-8.

While the fluorescence lifetimes of the ICC sensor in HEC gels report on the nanoviscosity when using the viscosity calibration with sucrose solution, they report on the macroviscosity when using the bulk sample viscosity (Figure 4-10). The macroviscosity of a gel measured in a rotational viscosimeter is influenced not only by the polymer concentration but also by the degree of crosslinking, polymer backbone rigidity and sidechain decoration, all of which I will combine in the collective term mesh parameters. Which of these mesh parameters also influence the viscosity sensed by the fluorescent molecular rotor ICC would be speculative at this point but worthwhile to investigate in the future. Figure 4-10A depicts the marcroviscosity response of different polymer and sucrose solutions to the concentration of the respective viscogenic compound governing all the mesh parameters contribution to bulk viscosity. The functional correlation can often be described by a power law[176]:

$$\eta = \eta_0 + Ac^b \tag{37}$$

Where η_0 is the viscosity of the solvent, A, and b are constants and c is the concentration of the polymer. Fit values for HEC-gel, mucin, and Ficoll400 mixtures in aqueous solution are summarized in Table 3.

Table 3. Fit values of viscosity dependency on concentration in different viscous solutions shown in Figure 4-10A.

Sample	η_0 (mPa s)	A (mPa s)	b
HEC	(1.0±0.2)	(2.8±0.8) x10^{-4}	(4.1±0.1)
mucin	(2.6±0.2)	(6.8±6.2) x10^{-4}	(2.2±0.2)
Ficoll 400	(2.6±0.6)	(8.7±6.8) x10^{-7}	(3.1±0.1)

It is clear from the concentration-viscosity relation, that all three mixtures behave significantly different, but clearly distinct from sucrose/water mixtures. To explain the differential response of ICC lifetime to nanoviscosity and macroviscosity (Figure 4-10C), we need to look at the microscopic structure of the HEC gel (Figure 4-9). There are two domains in a HEC gel with vastly different properties: a) the mesh itself and b) the intermesh solvent, which is water in the case of the aqueous HEC gels. The HEC polymers form a mesh in solution with large pore size (100-500 nm for 0.5% HEC[175]) compared to the fluorescent probe size. In the experiments described above, more than 95% of the solution has actually a very low viscosity on the nanoscale. Only ICC molecules in the direct vicinity of the rigid mesh will actually report on a higher viscosity while most experience a local environment indistinguishable from water. The same holds true for WGA-ICC. Apart from a constant offset in mean lifetime, which originates in the binding of ICC to WGA, their slope in the Förster-Hoffmann plot for HEC/water mixtures is identical ($\alpha = 0.14 \pm 0.01$, Figure 4-8E). The picture changes when mucins are introduced to the HEC/water solutions. Here, the WGA-ICC will bind to the mucins o-glycan sidechains and report on the steric restriction imposed on the intramolecular rotation of ICC. The insensitivity of WGA-ICC bound to mucin to HEC gel concentration, as seen by the slope $\alpha = 0.036 \pm 0.004$ (Figure 4-8E), suggests that the polymer mesh itself, here mimicked by the HEC gel mesh, is contributing to the viscosity response of WGA-ICC only very slightly. Following from that, we conclude that the fluorescence lifetime of WGA-ICC in conjugation with mucins is mostly dependent on the intermesh solvent. And this, in turn, means that when using WGA-ICC as a viscosity sensing probe for mucus, macroviscosity is accessible only in a small range of fluorescence lifetimes without significant extrapolation. The nanoviscosity of the inter mesh solvent, on the other hand, can be obtained from the small molecule sucrose calibration curve in most physiologically relevant cases.

As another polymer solution besides HEC gel, I also investigated Ficoll 400 (molecular weight = 400 kDa) for comparison. Ficoll does not form gels but rather mimics a secondary polymer which contributes to macromolecular crowding[37]. Interestingly, a different behavior can be observed in

Ficoll 400 solutions. Both, for WGA-ICC in the presence and absence of mucin, a very similar behavior in the Förster-Hoffmann plot (Figure 4-11A-C) can be observed, as seen by identical fit values from the Förster-Hoffman plot (Figure 4-11C, eq. (13)). Importantly, the viscosity sensitivity to increasing Ficoll 400 concentrations is not abolished by the attachment of WGA-ICC to mucin in contrast to HEC gels (Figure 4-11). Ficoll 400 is a highly branched polymer similar to HEC[37,175]. But Ficoll 400 does not form a rigid mesh. The branched structure rather increases inter mesh solvent viscosity by an effect called macromolecular crowding[37]. Macromolecular crowding leads to an excluded volume effect, which is dependent not only on concentration of Ficoll but also on its molecular weight. This can be seen in Figure 4-11D, where the reduction in the molecular weight (Ficoll 70: molecular weight = 70 kDa) results in an increase in the slope of the Förster-Hoffmann plot. With and without mucins, we obtain a similar Förster-Hoffmann plot for Ficoll/water mixtures (Figure 4-11C). Compared to the calibration curve in HEC gel, this is explained by the absence of a mesh structure in Ficoll solutions. Everything considered, we conclude that the WGA-ICC viscosity sensor in mucus will report on viscosity predominantly in the inter mesh solvent. Macromolecular crowding, leading to an excluded volume, also effects the rate of intramolecular rotation in WGA-ICC, regardless of its binding to mucins. This fact makes the calibration in Ficoll solutions a valuable tool in the characterization of the mucus layer since mucins are reported to also induce macromolecular crowding[177].

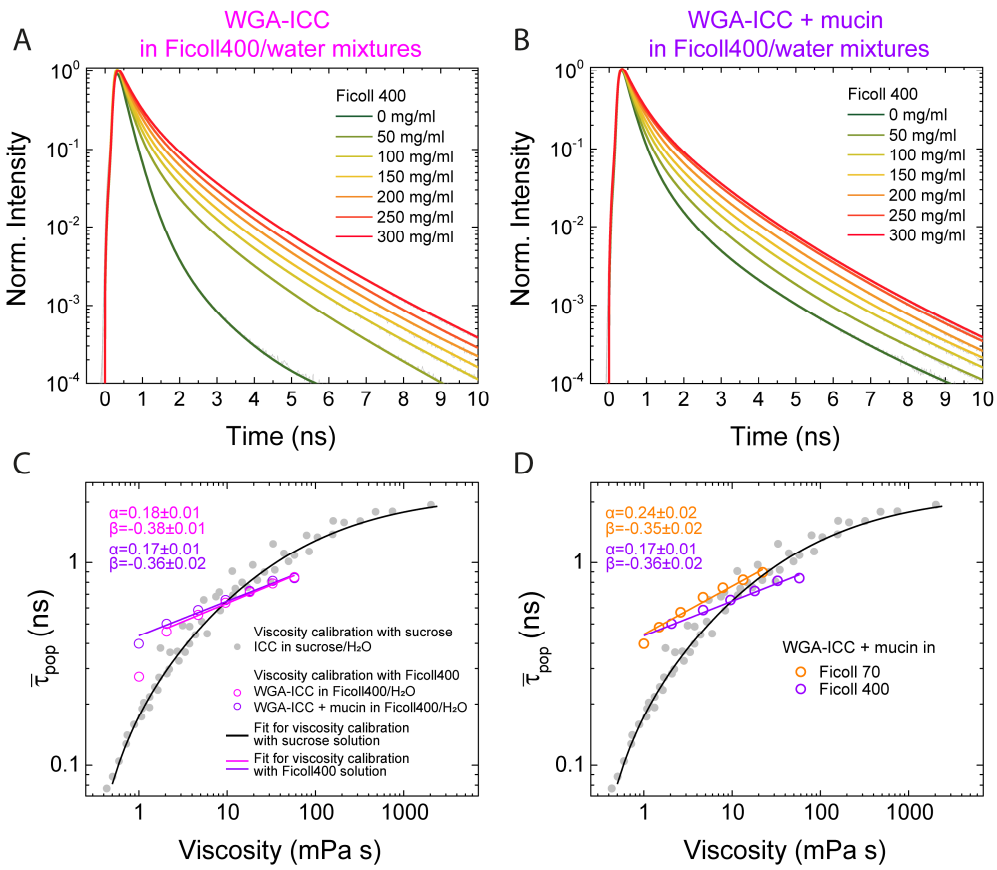

Figure 4-11. Fluorescence lifetime response of WGA-ICC to increasing viscosity achieved by Ficoll 400, a sucrose-based highly branched polymer (A) Fluorescence decays of WGA-ICC in different Ficoll 400/water-mixtures (B) Fluorescence decays of WGA-ICC in different Ficoll 400/water-mixtures with added 1 mg/ml mucin each. Fit values for (A) and (B) are summarized in Table A5 (C) Förster-Hoffmann plots, showing the dependency of the mean fluorescence lifetime ($\bar{\tau}_{pop}$) on viscosity. The coloured lines show Förster-Hoffmann fits (eq. (13)) of the linear area of the respective lifetime data set. (D) comparison of fluorescence lifetime response of WGA-ICC in Ficoll 70 and Ficoll 400 solutions, the obtained slopes (α) and offsets (β) are indicated. Fluorescence lifetime dependency of ICC (grey dots) in sucrose/water mixtures, together with a global fit (eq. (16)), are shown for comparison. Decay curves of WGA-ICC were recorded in the TCSPC FLIM setup: λ_{ex}=530 nm, λ_{em}>545 nm, T=20°C.

4.1.3 Mucus viscosity determination in live cells using FLIM

In order to apply the viscosity calibration curves to live cells, one has to first determine the autofluorescence characteristics of mucus on live cells. For that, we investigated the autofluorescence of purified mucus mucin type II from porcine stomach and collected mucus from murine colon. Autofluorescence has been described in earlier studies[178,179]. Its origin wasn't explained sufficiently but it has been suggested that collagen fragments from subjacent tissue might contribute to the observed fluorescence[180].

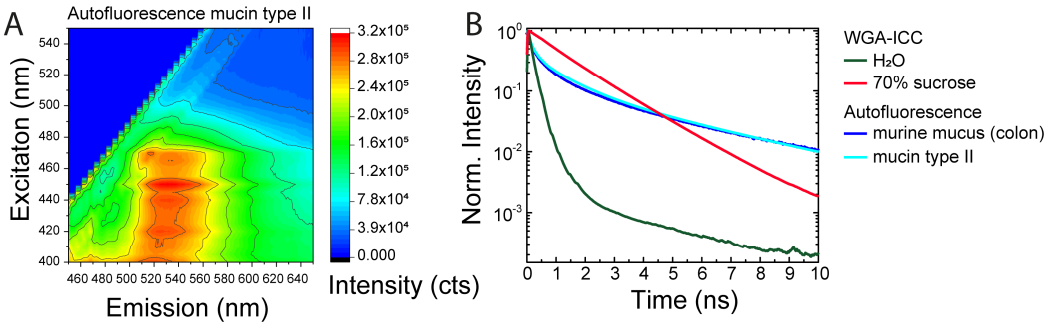

Figure 4-12. Autofluorescence of mucins and mucus. (A) Contour plot of autofluorescence in commercially available mucin type II (2 mg/ml), shown is fluorescence intensity in dependence of excitation and emission wavelength. (C) Fluorescence decay curves of murine mucus from the colon (green) and mucin type II (2 mg/ml) compared to the fluorescence decay of WGA-ICC in water and 70% sucrose. Experimental conditions for (B): fluorescence excitation of murine mucus at λ_{ex} = 530 nm, fluorescence emission at λ_{em} > 545 nm. mucin type II: λ_{ex} = 486 nm and λ_{em} > 515 nm.

Figure 4-12 depicts a contour plot of the autofluorescence found in commercially available mucins type II from porcine stomach alongside its fluorescence decay in comparison to mucus samples from murine colon. The contour plot shows steady-state fluorescence intensity in dependence of excitation and emission wavelength. It exhibits most intense fluorescence in the range of 510-560 nm while absorbing light mostly up until 470 nm and with that would be in good agreement with the proposed contribution of collagen to the fluorescence signal[180]. Figure 4-12B presents autofluorescence decay curves found in the mucin type II and murine colon mucus in comparison to the target fluorescence of WGA-ICC in water and 70% sucrose. Using Cluster-FLIM, autofluorescence can be easily recognized by its unique fluorescence lifetime signature, separated from the target fluorescence, and then disregarded during live cell Cluster-FLIM analysis. In this case, WGA-ICCs fluorescence decay covers a broad range of lifetimes, as it is dependent on the viscosity of its microenvironment which is exemplified in Figure 4-12B for WGA-ICC in water and 70% sucrose. Hence, discrimination of autofluorescence becomes more complicated. An increase in fluorescence lifetime measured in samples with increasing mucin concentration could originate either in the increasing fluorescence lifetime of WGA-ICC due to higher viscosity caused by the higher mucin concentration or just by the larger contribution of mucins autofluorescence, for which longer fluorescence lifetimes were found than those of WGA-ICC in water. Both effects would

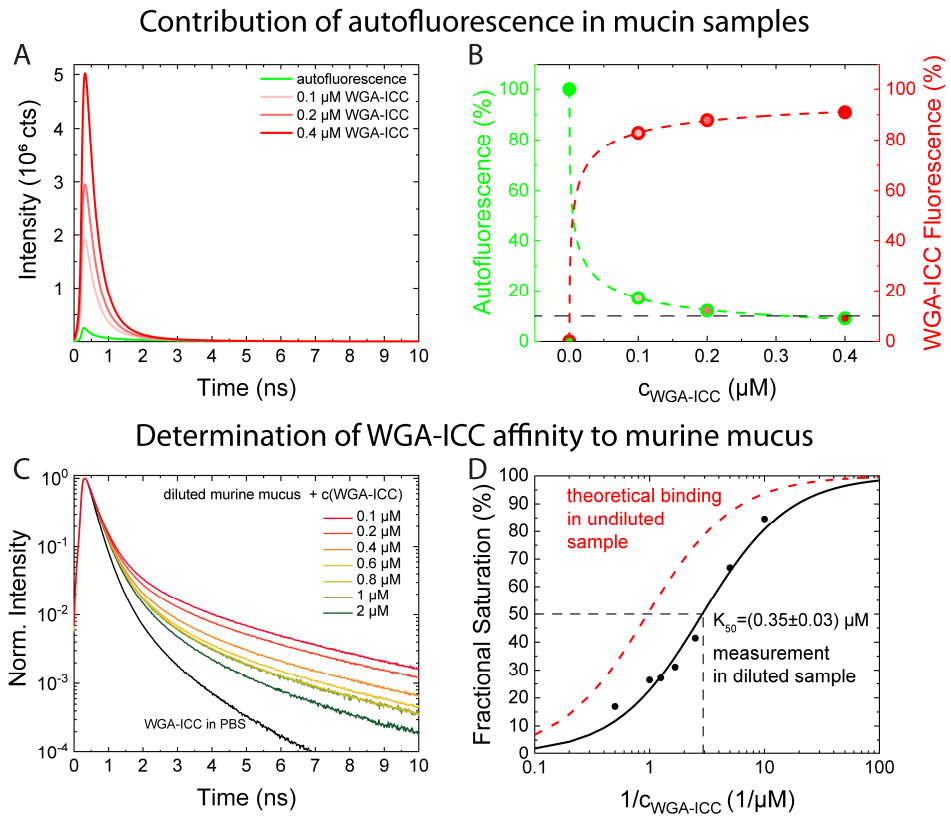

Figure 4-13. Contribution of autofluorescence in mucin and mucus experiments when using WGA-ICC as fluorescent probe. (A) Comparison of non-normalized fluorescence decays of autofluorescence found in murine colon mucus (green decay) to varying concentrations of WGA-ICC in aqueous solution (shades of red) (B) Plot of the fraction $I_{autoflu}/(I_{autoflu} + I_{WGA-ICC})$ to evaluate the percentile of autofluorescence (green) contribution to total fluorescence as a function of WGA-ICC concentration. (C) Fluorescence decays of increasing concentrations of WGA-ICC in diluted murine mucus. Mean fluorescence lifetimes were used to calculate WGAs fractional binding saturation to mucin according to eq. (33) and plotted in (D) over inverse WGA-ICC concentration and fitted to a Hill-equation (eq. (34), black line). The red dashed line indicates the Hill-fit for an undiluted mucus sample. Experimental conditions: λ_{ex} = 530 nm, λ_{em} > 545 nm, T=37°C.

probably be superimposed but indistinguishable from each other. In order to study the viscosity range in mucus samples using ICC, the autofluorescence contribution to overall fluorescence intensity should be negligible. We estimate that less than 10% autofluorescence should be sufficient for reliable discrimination of FLIM signatures[152]. For the determination of optimal experimental conditions, I titrated a mucus sample collected from the murine colon (provided by AG Prof. Fulde, Department of Veterinary Medicine) with increasing concentrations of WGA-ICC (Figure 4-13A). The relative contribution of autofluorescence or WGA-ICC target fluorescence can be calculated from the areas under the decay curve using $I_{autoflu\ or\ WGA-ICC}/(I_{autoflu} + I_{WGA-ICC})$ and is plotted over WGA-ICC concentration in Figure 4-13B. At 0.1 µM of WGA-ICC, we still see an autofluorescence contribution of 17%, whereas 0.4 µM of WGA-ICC contribute to 91% of the fluorescence in the given mucus sample, reducing the autofluorescence contribution to 9%, below

our set threshold. Next, we examined the binding affinity of WGA to the sialic acids of the glycoprotein mucin. The goal of this investigation is to have a viscosity sensor bound to the mucin mesh. The higher the ratio c_{mucin}/c_{WGA} the higher is the affinity based binding fraction of WGA-ICC. On the other hand, a high WGA-ICC concentration results in a larger fraction of unbound WGA-ICC, reporting on the solvent viscosity rather than the viscosity in mucins. The binding affinity was determined by titrating diluted murine mucus with increasing concentrations of WGA-ICC. The murine mucus had to be diluted by a factor of 1:3 simply on grounds that the sample volume from animals was sparse and experiments had to be reduced and refined when possible. Fractional binding saturations was calculated from the fluorescence lifetime of ICC (eq. (33)) and plotted over the fraction c_{mucin}/c_{WGA} in a saturation plot (Figure 4-13D)[16]. The mucin concentration in this sample is constant but unfortunately not known. Therefore, it was set to 1. The apparent binding constant in diluted mucus is then calculated from the fractional saturation data fitted with a Hill function (eq. (34)), $K_{50} = (0.35 \pm 0.03)$ µM. Recalculation for a theoretically undiluted sample, results in a binding constant of $K_{50} = (1.04 \pm 0.08)$ µM. Accounting for both, binding affinity, and low autofluorescence background, 0.5 µM WGA-ICC will be used in live cell experiments yielding an estimated target fluorescence contribution of >90% and a bound WGA-ICC fraction of more than 70%.

We next performed the live cell experiments to determine mucus viscosity under native conditions. The mucus layer produced by goblet cells in the airways and digestive tract is characterized by its simultaneous ability to enable the exchange of gases and nutrients while protecting against pathogens and mechanical insult. However, surprisingly little is known about the physical properties on the microscopic and nanoscopic scale of this layer that facilitate these seemingly contradictory qualities. Thus, I capitalized on WGA-ICCs sensitivity to the viscosity of its microenvironment in combination with our FLIM setup to compile a spatially resolved map of local viscosities in the mucus layer and evaluated gradients as well as heterogeneities thereof with so far unmatched resolution in the model cell line HT29-mtx.

HT29-mtx is an immortalized mucus producing cell line resembling the epithelium of the small intestine[181]. With the fluorescence lifetime calibration of WGA-ICC at hand, I investigated spatially resolved viscoelastic properties of HT29-mtx cells and the mucus layer they produce. Figure 4-14 shows HT29-mtx cells, incubated with WGA-ICC. WGA-ICC clearly stains cell membranes of the HT29-mtx cells as well as some intracellular vesicles (Figure 4-14B, magenta and blue). Presumably, these are membrane bound mucins and secretory mucin filled vesicles. Here, we find a mean fluorescence lifetime of $\overline{\tau}_{pop}(magenta) = (1.00 \pm 0.01)\ ns$ and $\overline{\tau}_{pop}(blue) = (1.48 \pm 0.01)\ ns$. On the apical side, one finds a homogeneous mucus layer, evenly stained by WGA-ICC

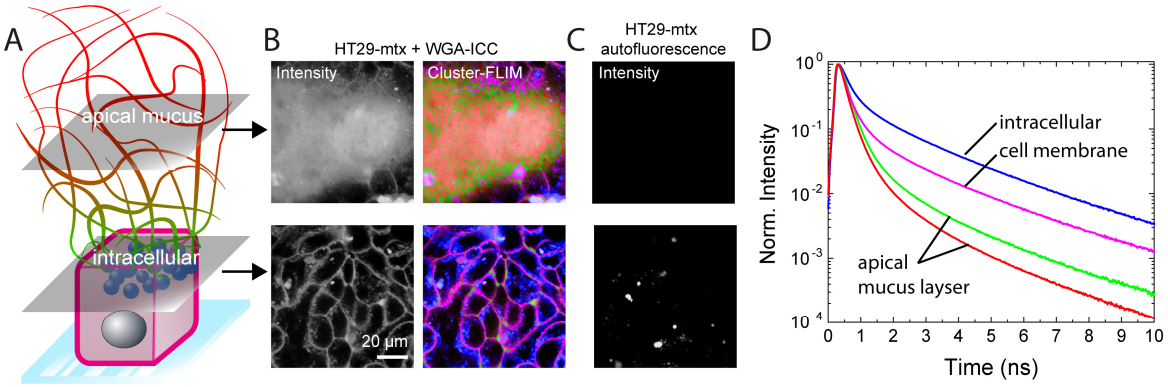

Figure 4-14. Fluorescence lifetime imaging of mucus producing HT29-mtx cells (A) schematic of depth at which FLIM measurements were taken (B) HT29-mtx incubated with 0.5 µM WGA-ICC for 30min. morphological features are visible as indicated in (A) i.e. showing the stained mucus layer and the subjacent cellular monolayer. (C) Autofluorescence of HT29-mtx cells and the apical mucus layer on top of them. Cluster FLIM false-color images according to fluorescence decay curves shown in (D). Experimental conditions: λ_{ex} = 530 nm, λ_{em} > 545 nm, T=37°C.

and characterized by the green ($\overline{\tau}_{pop}(green) = (0.49 \pm 0.01)\, ns$) and red ($\overline{\tau}_{pop}(red) = (0.38\, ns \pm 0.01)$) lifetime cluster (see Table 4). With identical settings, one finds only residual autofluorescence in the untreated HT29-mtx cells and only in the secretory vesicles with highest mucin concentration (Figure 4-14C, bottom row). In the apical mucus layer, the mucin concentration seems to be too low to produce any detectable autofluorescence. In other words, any fluorescence in the mucus layer will be 100 % target WGA-ICC sensor fluorescence. I have presented a number of calibration curves for WGA-ICC above. In order to calculate an apparent viscosity from the lifetime data found in HT29-mtx cells, it is instructive to first consider which calibration is actually most representative of the physiology of the mucus layer. The sucrose calibration mimics a homogeneous increase of the local viscosity reported by WGA-ICC, which is the nanoviscosity ($\eta_{solvent}$). HEC gel solutions increase the bulk viscosity by the formation of a rigid mesh to which WGA-ICC responds only weakly when bound to mucin (Figure 4-8E). This calibration lets us estimate the macroscopic viscosity produced by a polymer mesh or protein backbone (η_{mesh}). The Ficoll 400 calibration, on the other hand, reflects WGA-ICCs lifetime response to the excluded volume in the inter mesh solvent, providing a measure for an apparent viscosity based on macromolecular crowding (η_{mc}).

Therefore, dependent on which calibration curve is used, $\eta_{solvent}$, η_{mesh}, as well as η_{mc} can be evaluated on the basis of the Cluster-FLIM analysis. Fit parameter of the fluorescence decays shown in Figure 4-14D as well as viscosity values calculated are summarized in Table 4.

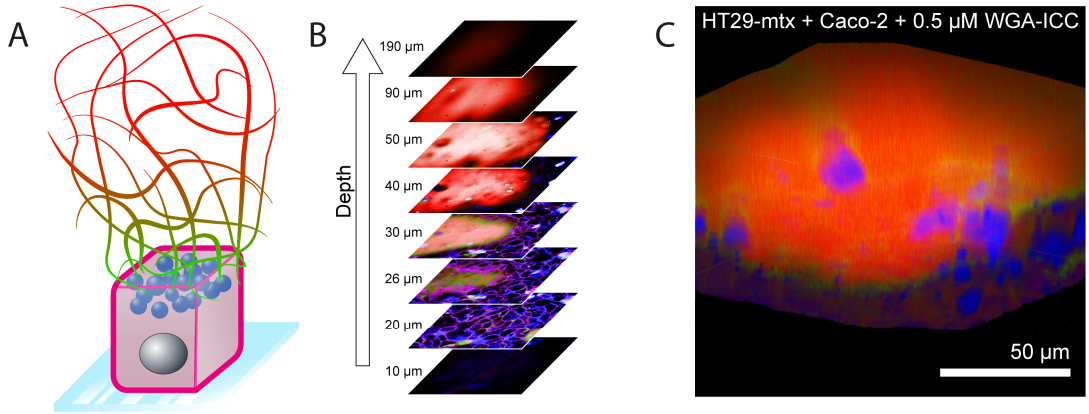

Figure 4-15. 3D representation of apical mucus layer of HT29-mtx cells. (A) Schematic representation of cluster distribution amongst intra- and extracellular mucus (B) z-stack of FLIM images of HT29-mtx cells in co-culture with Caco-2 cells. False-color images based on WGA-ICCs fluorescence lifetime reporting on domains with different viscosity (C) 3D tomographic reconstruction of z-stack depicted in (B) showing the heterogeneity of the apical mucus layer. Experimental conditions: λ_{ex} = 530 nm, λ_{em} > 545 nm, T=37°C.

Table 4. Fit parameter of WGA-ICC in HT29-mtx and Co-cultures shown in Figure 4-14 and Figure 4-15. τ_i: fluorescence lifetime of the *i*-th decay component in ns, α_i the corresponding relative amplitude in %, $\bar{\tau}_{pop}$: mean fluorescence lifetime and χ^2_{red}: reduced chi square. $\eta_{solvent}$ apparent nanoviscosity based on the calibration in sucrose (Figure 4-7), η_{mc} the apparent viscosity caused by macromolecular crowding based on the Ficoll 400 calibration (Figure 4-11), and η_{mesh} the apparent viscosity based on the HEC calibration (Figure 4-8). Experimental conditions: λ_{ex} = 530 nm, λ_{em} > 545 nm, T=37°C.

Cluster	α_1 (%)	α_2 (%)	α_3 (%)	α_4 (%)	τ_1 (ns)	τ_2 (ns)	τ_3 (ns)	τ_4 (ns)	χ^2_{red}	$\bar{\tau}_{pop}$ (ns)	$\eta_{solvent}$ (mPa s)	η_{mc} (mPa s)	η_{mesh} (mPa s)
blue	75.2 ±0.6	16.2 ±1.2	7.9 ±1.6	0.6 ±0.5	0.26 ±0.01	1.16 ±0.13	2.54 ±0.27	4.83 ±0.63	2.4 ±0.5	1.48 ±0.01	179 ±7	1282 ±32	n.d.
magenta	84.8 ±1.4	10.3 ±0.8	4.6 ±0.6	0.3 ±0.1	0.21 ±0.01	0.69 ±0.11	2.06 ±0.17	5.00 ±0.45	1.6 ±0.6	1.00 ±0.01	22.8 ±0.4	131 ±4	n.d.
green	88.7 ±2.8	9.5 ±2.5	1.6 ±0.3	0.16 ±0.1	0.20 ±0.01	0.52 ±0.08	1.60 ±0.34	4.40 ±1.08	1.4 ±0.1	0.49 ±0.01	3.3 ±0.1	1.9 ±0.2	3700 ±1400
red	88.0 ±2.8	10.4 ±2.4	1.4 ±0.4	0.2 ±0.1	0.20 ±0.01	0.46 ±0.08	1.28 ±0.37	3.48 ±1.53	3.2 ±1.8	0.39 ±0.01	2.0 ±0.1	n.d.	8.0 ±5.8

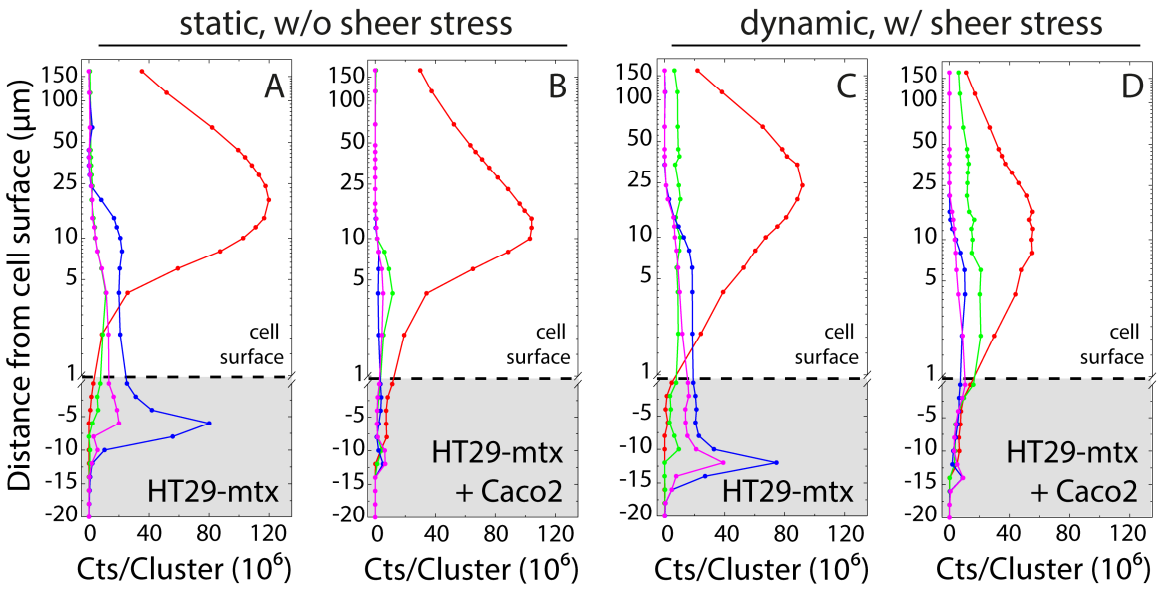

Figure 4-16. Distribution of fluorescence lifetime clusters found in in HT29-mtx cell cultures and the superjacent mucus layer in dependence of the distance to the cell surface. 30 FLIM measurements as z-stacks from the glass surface of the cell dish up to a depth of 190 µm of the same ROI were taken from (A) HT29-mtx in monoculture and static growing conditions, (B) HT29-mtx and Caco-2 in co-culture and static growing conditions, (C) HT29-mtx in monoculture and dynamic growing conditions, and (D) HT29-mtx and Caco-2 in co-culture and dynamic growing conditions. Colors according to fluorescence decays shown Figure 4-14D.

In a next step, I was interested in compiling a depth dependent viscosity profile of the HT29-mtx cells and its mucus layer based on WGA-ICC's fluorescence lifetime. For that purpose, I collected a z-stack of FLIM data of one region of interest (ROI) (Figure 4-15B) for HT29-mtx cells in different culture conditions. The culture growth conditions are as follows: HT29-mtx in a monoculture and a 1:1 co-culture with Caco-2 cells, both with static and dynamic growth conditions, yielding four different cell cultures. Caco-2 cells are a human colon carcinoma cell line resembling the phenotype of enterocytes of the small intestine. Caco-2 and HT29-mtx are often cultured together in an effort to create a physiologically more relevant model culture[181,182]. In the dynamic case, culture flasks where placed on an orbital shaker during the entire growing period to simulate sheer forces exerted onto the epithelium during physiological function of the small intestine. The mucus secretion from HT29-mtx cells was triggered by the addition of 100 µM ATP[183]. 30 measurements were taken, ranging from the glass surface of the cell dish, where the cells are attached to (Figure 4-15A), to 190 µM deep into the cell culture sample. The focal plane where cells were visible first, were set to z=0 µm. The z-resolution from -20 µm to 20 µm was 2 µm, but wider spaced with increasing depth. In these stacks, cells are visible in the focal plane approximately from a depth of 0 µm to 16 µm. Above 16 µm, the frame is mostly dominated by the diffuse mucus layer secreted by the HT29-mtx cells. The z-stacks of the four different culture growth conditions are shown in Figure 4-16 and

compare the depth dependent distribution of the discovered fluorescence lifetime species. In the FLIM data, four distinct fluorescence decay clusters were found and assigned to distinct morphological features of the cells as stated above. Figure 4-16 shows photon counts for each of the identified fluorescence decay clusters plotted as a function of depth. The blue and magenta decay cluster (secretory vesicles and membrane bound mucins) are almost exclusively found in the cell layer, in a depth of up to 16 µm. The HT29-mtx monoculture expresses notably more secretory vesicles and are characterized by a stronger staining of the membrane bound mucins, signaled by more intense blue and magenta fluorescence decay clusters, which is to be expected, as Caco-2 should not secret mucus at all. Directly on top of the cells one finds a several micron thick layer of mucus assigned to the green cluster but the bulk part of the mucus layer shares the red decay cluster (Figure 4-15 and Figure 4-16).

A depth dependent viscosity profile can be calculated from the mean fluorescence lifetime $\overline{\tau}_{frame}$ at each depth and the rearranged Förster-Hoffmann equation (eq. (13)):

$$\eta = 10^{\left(Log_{10}(\overline{\tau}_{frame} - \beta)/\alpha\right)} \tag{38}$$

Equation (16), as used in sucrose calibrations, yields:

$$\eta = Exp\left(ln\left(\left(\frac{e^{-\frac{E_a}{k_b T}}}{1/\overline{\tau}_{frame} - k_r - k_x} - \frac{1}{A_{max}} \right) C^{-1} \right) \alpha^{-1} \right) \tag{39}$$

With $\overline{\tau}_{frame}$ calculated as the cluster member weighted mean fluorescence lifetime:

$$\overline{\tau}_{frame} = \sum_{cluster} \frac{\overline{\tau}_{pop}(cluster) * \#pixel_{cluster}}{total\ \#pixel\ in\ frame} \tag{40}$$

In section 4.1.2, I established 3 different calibration curves, each representing a different contribution to the viscosity properties of mucus. The calibration with WGA-ICC bound to mucin in sucrose solutions can be used to evaluate the nanoviscosity of the inter mesh solvent in the mucus. WGA-ICC bound to mucin in Ficoll 400 solutions reports on the macromolecular crowding and WGA-ICC bound to mucin in HEC gels lets one estimate the macroviscosity generated by the gel mesh or the protein backbone (Figure 4-17). Depending on which calibration is applied to the FLIM data of the mucus producing cell cultures shown in Figure 4-15 and Figure 4-16, all three contributions can be estimated. Note that I only included lifetime clusters in the calculation of $\overline{\tau}_{frame}$ (eq. (40)) with a lifetime which is covered by the respective calibration data without significant extrapolation. The

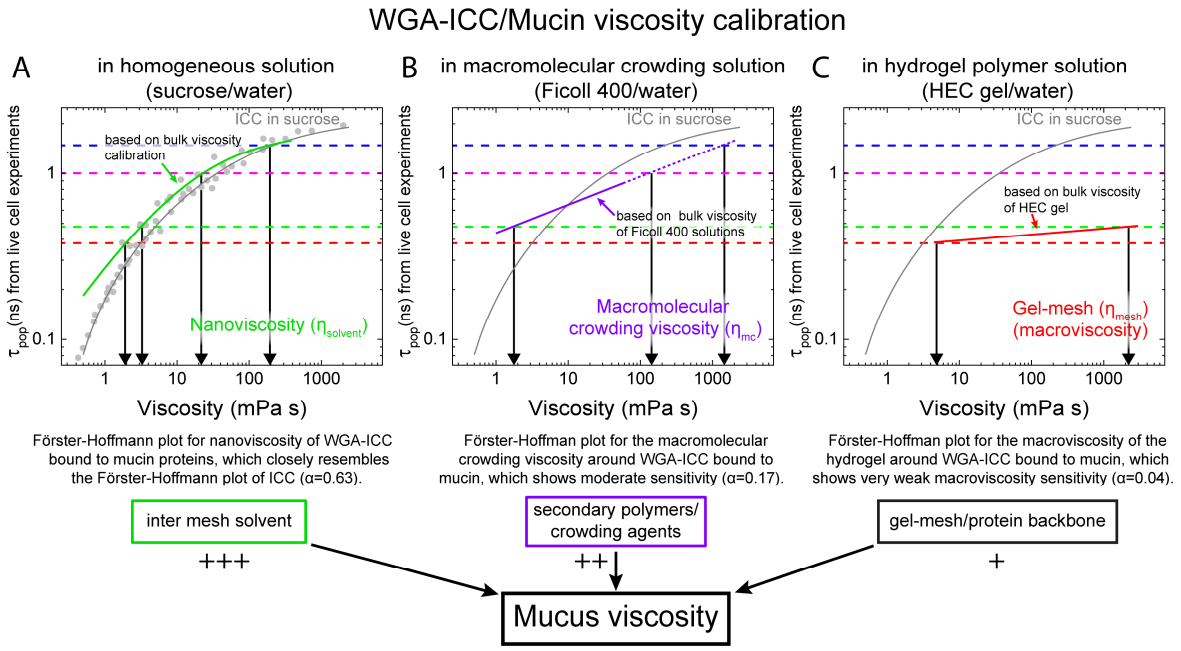

Figure 4-17. WGA-ICC/Mucin viscosity calibration. (A) Calibration in sucrose/water mixtures (Figure 4-7D) (B) Calibration in Ficoll 400/water mixtures (Figure 4-11C) (C) Calibration in HEC/water mixtures (Figure 4-8E). Indicated are also the mean fluorescence lifetimes of FLIM clusters found in the cell cultures as colored dashed lines (Figure 4-14, Figure 4-15, and Figure 4-16) and their respective equivalent viscosity in each calibration as vertical arrows. The plus signs denote sensitivity to the respective viscosity.

viscosity profiles of all four cultures are plotted in Figure 4-18. Looking at the nanoviscosity (Figure 4-18A, B), highest viscosities are found in the intracellular region where tightly packed mucin granules are located inside of the secretory vesicles. Although extracellular mucins are clearly visible up until 190 µm, the mucus layer nanoviscosity is not clearly distinct from the medium viscosity beyond 25 µm depth. Embedded into the homogeneous extracellular mucus layer with low viscosity, globular structures with a high viscosity of about 180 mPa s can be found (Figure 4-15C, blue cluster). Here, the viscosity is comparable to that of intracellular secretory vesicles, leading me to the hypothesis that these structures are freshly expelled mucin aggregations which aren't fully unfolded yet (see Figure 2-5C). Whether this reflects the physiologically normal case or is caused by the ATP-triggered mucus expulsion, is unclear at this point and remains to be investigated. The intracellular macromolecular crowding (Figure 4-18C) reveals a highly viscous regime in the secretory vesicles in all cell cultures ranging from 100-1000 mPa s. The macroviscosity of the mucus layer (Figure 4-18D) gives information about the viscosity encountered by macroscopic entities like for example food, during peristalsis. From the cell surface up to about 10 µm, one finds a dense mucus layer with a macroscopic viscosity of 40-700 mPa s at the cell surface, which continuously decrease until 10 µm, probably reflecting the firmly attached mucus layer[184]. With a distance from the cell surface greater than 10 µm, the macroscopic viscosity of the

mucus layer is low. This is called the slippage plane and its properties facilitates the propulsion of food during peristalsis by lubricating the undigested material[184]. When comparing cell cultures, mucus viscosity in cultures grown under dynamic conditions is more evenly distributed over depth (Figure 4-18D). The flow of the culture medium, which mimics physiological strain exerted on the mucosa, results in higher viscosity of 20-40 mPa s in the region beyond 10 µm, significantly higher than the 5-10 mPa s found in static cultures. This might be explained by additional entanglement of mucins induced by the shaking, leading to an increased macroscopic viscosity.

In cell cultures grown under static conditions, the HT29-mtx monoculture has a consistently higher viscosity throughout the cell and mucus layer. This is explained by the absence of non-secreting Caco-2 cells, which in turn leads to a lower extracellular mucin concentration, which is consistent with the lower viscosity observed in those cultures. Additionally, proteolytic enzymes like meprin-β are predominantly produced by enterocytes (Caco-2) and only when challenged by bacterial presence[58]. Missing enzymatic cleavage of the mucin multimers as well as the absence of bacterial stimuli possibly lead to a systematically higher viscosity in these cell cultures missing either enterocytes or contact to a microbiome.

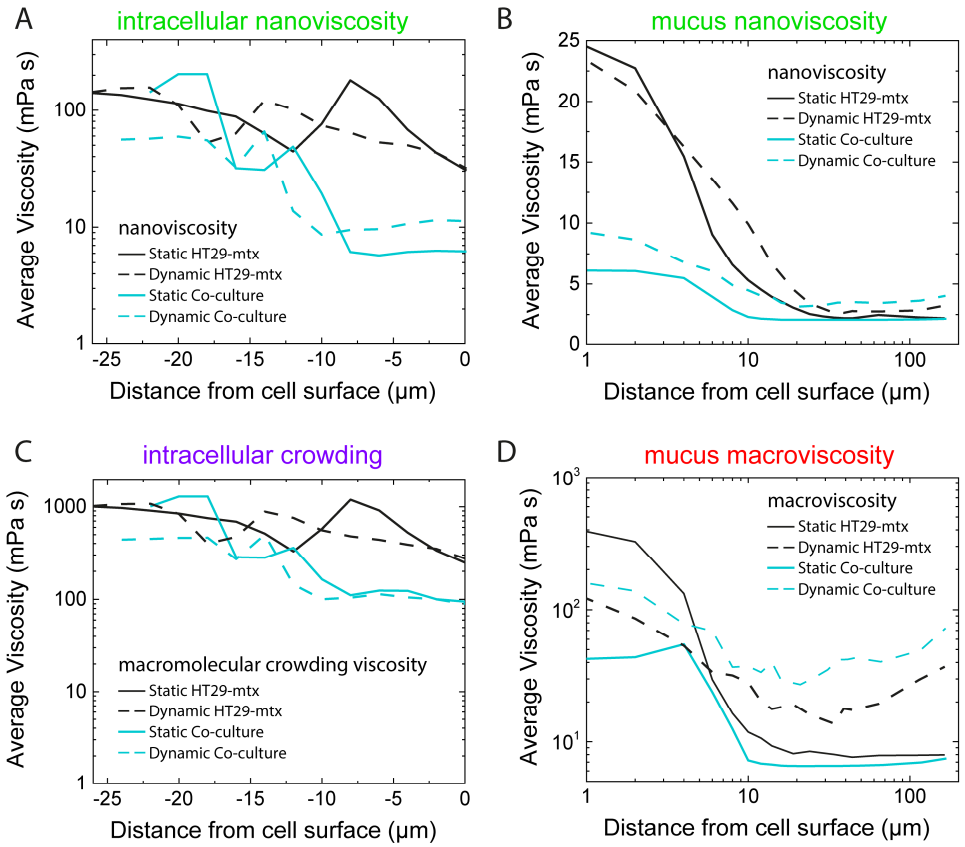

Figure 4-18. Depth profile of average viscosity found in the mucus layer on live HT29-mtx cell cultures (A) Nanoviscosity found in HT29-mtx cell cultures calculated with eq. (39) and (40), and based on the calibration of WGA-ICC bound to mucin in sucrose/water mixtures (Figure 4-7). (B) Apparent viscosity based on crowding found in HT29-mtx cell cultures calculated with eq. (38) and (40), and based on the calibration of WGA-ICC bound to mucin in aqueous solutions of Ficoll 400. The transition between the intracellular space and the apical mucus layer as gathered from the FLIM images are indicated. Experimental conditions as in Figure 4-15.

4.1.4 ICC as viscosity sensor in murine mucus

In the previous section, questions regarding the physiological relevance of the mucus layer produced by cell culture under different growing conditions were raised. Specifically, if the stimulus from bacterial contact is altering the properties of the mucus layer in the gastro/intestinal tract remained to be addressed. To focus on this question, I investigated the viscosity found in mucus of the murine intestinal tract and in particular the influence of the microbiome or lack thereof on mucus nanoviscosity. Samples of murine mucus were prepared by the AG Prof. Fulde.

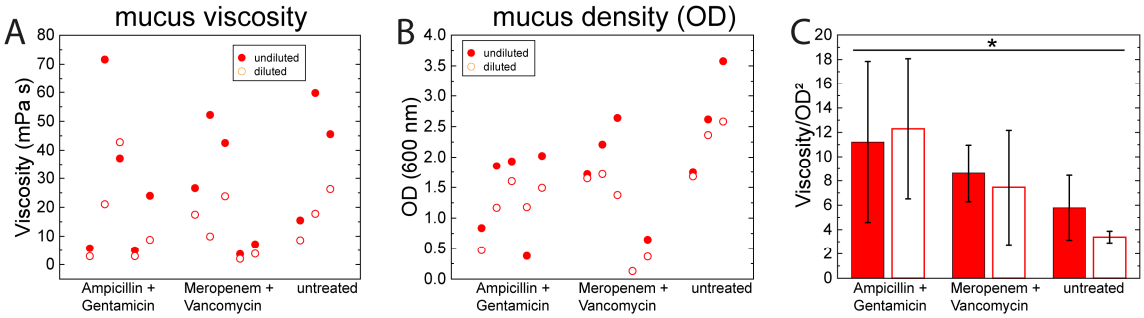

Figure 4-19. Changes in murine intestinal mucus viscosity after antibiotic treatment (A) mean fluorescence lifetime of 0.3 µM WGA-ICC in mucus of the murine small intestine after treatment with two different combinations of antibiotics "Ampicillin + Gentamicin" and "Meropenem + Vancomycin", and an untreated group. (B) Optical density at 600 nm of the mucus samples shown in (A) as a measure of mucin concentration. (C) Ratio of mean fluorescence lifetime over optical density squared for all three treatment groups. "Diluted" samples were diluted 1:1 with PBS before fluorescence decay and absorbance measurements. Experimental conditions: λ_{ex} = 530 nm, λ_{em} > 545 nm, T=37°C.

For that reason, mucus was harvested from the small intestine of 10 juvenile male mice after antibiotic treatment. Mice were divided into two groups and each treated with a combination of two antibiotics, Ampicillin and Gentamicin or Meropenem and Vancomycin. A group of untreated mice was also tested as reference for mucus viscosity in healthy mice. Once again, WGA-ICC was used to characterize the local environment of the molecular rotor ICC when bound to mucins of the murine mucus and calculate the nanoviscosity based on ICC's fluorescence lifetime. Since the intestines were rinsed with PBS before mucus harvest, unfortunately, the actual mucus samples ended up being diluted to an unknown extent which could not be controlled for. The determined fluorescence lifetimes from those samples were inconsistent and the data were not fit for a consistent viscosity determination (Figure 4-19A, and Table A7). In order to account for the random dilution, I also measured the mucus absorbance at λ=600 nm as a measure for mucin concentration in each sample (Figure 4-19B). Normalization of the viscosity data was achieved using the ratio $\eta/OD^2(600\,nm)$ as viscosity of mucus empirically increases with concentration squared (Figure 4-10A and Table 3). This normalization yielded more consistent results (Figure 4-19C). To validate

this method, I further diluted all mucus samples by a known factor of 1:1 with PBS and again determined the ratio τ_{mean}/OD in the diluted samples. This resulted in the same values as for undiluted samples, showing that this ratio is actually characteristic for the original mucus sample and independent of dilution, hence describes a quality independent of mucin concentration. Thus, this approach allows at least for qualitative statements and comparison between all murine samples. The lowest relative viscosity is found in the small intestine of untreated mice. Treatment with both antibiotic combinations led to an increase of relative viscosity where Ampicillin and Gentamicin produced the highest relative viscosity found the small intestine of all mice. Statistical analysis was done using a two-way ANOVA and statistical significance was assessed using the Tukey Test. No significant difference of $\eta/OD^2(600\,nm)$ was found between the undiluted and diluted sample, but the treatment with Ampicillin and Gentamicin produced a higher relative viscosity compared to the control group with a significance level of 0.05. Homeostasis of the intestinal mucus layer has been shown to be dependent on microbial triggers, which are a key factor in the proteolytic detachment of the mucus layer in the small intestine[58]. Also, motile bacteria employ proteolytic enzymes to lower the mucus viscosity in order to facilitate their movement[91]. Nevertheless, the acute changes of the mucus layer are very dependent on the used antibiotics. A higher viscosity as seen in our experiments upon antibiotic treatment is well explained by the aforementioned effects, and thickening of the mucus has been reported after treatment with different antibiotics, but also invariance[97,101].

4.2 Application of Cluster-FLIM to generate background free penetration profiles

4.2.1 Nanoparticle-enhanced drug delivery across the biological barriers of the skin

The skin poses as a target tissue of particular interest for drug administration as not only local diseases like atopic dermatitis or psoriasis can be treated directly but also systemic drug delivery can be achieved in case that sufficient drug penetration into deeper skin layers can be ensured. The latter is especially valuable as the GI tract and hepatic first-pass metabolism can be circumvented opposed to oral drug administration. To harness these benefits of transdermal drug delivery, the biological barrier functions of the skin has to be overcome. A detailed description of the skin and its barriers is given in chapter 2.2.2. Briefly, the skin comprises a list of chemical and mechanical barriers designed to protect the body from harmful environmental influences, toxins, pathogens. Most barrier function is found in the outermost skin layers, the viable epidermis (VE) and *stratum corneum* (SC). The SC can be described as a brick and mortar model[107], where corneocytes pose as bricks which are structurally coalesced with intercellular lipid matrix, the mortar. Three main penetration pathways have been proposed to overcome the skin barriers: the intercellular pathway through the intercellular lipid matrix, the intracellular pathway, using the corneocytes as penetration pathway as well, and the transfollicular pathway, using hair follicles as entry point into the skin (Figure 2-9)[185,186]. Nanoparticulate formulation of drugs are a promising tool to enhance the penetration of drugs across barriers[3,187], to increase bioavailability in deeper tissue layers[5], and ensure optimal therapeutic efficacy. Hair follicles have been proven as promising candidates for dermal and transdermal drug delivery when paired with a nanoparticle-based delivery system[130,188]. It has been shown that there exists a sweet spot for nanoparticle size which promotes a deeper penetration into the hair follicles and leads to accumulation in these orifices[125-127]. An in depth understanding of these pathways is the basis for the development of novel drug delivery system as documented for the first nanoparticulate formulation of the anti-cancer drug doxorubicin[189]. Advances in high-resolution imaging techniques[152] paired with theoretical approaches[190-192] provide the means to appropriately characterize the target tissue and nanoparticles, ultimately leading to the establishment of new drug delivery systems for topical dermatotherapy as well as transdermal drug penetration.

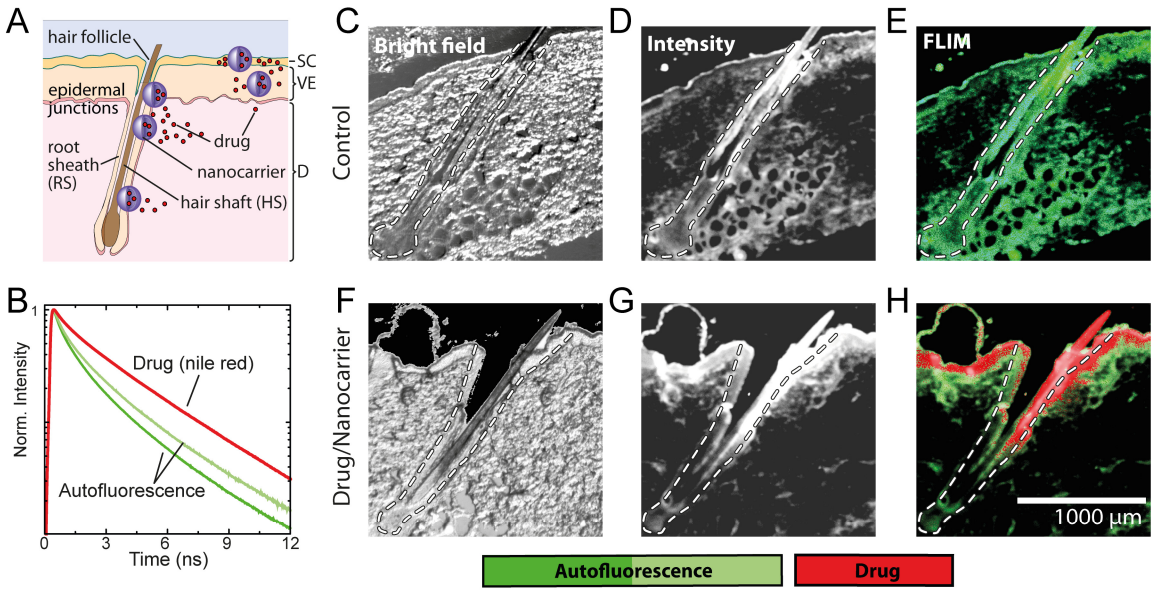

Figure 4-20. (A) Scheme of different transdermal drug delivery routes (C,F) bright field image of hair follicles (D,G) comparison of cargo fluorescence intensity with autofluorescence in the hair follicle (E,H) fluorescence lifetime imaging microscopy (FLIM), false color images based on fluorescence lifetime, shown in (B). Experimental conditions: fluorescence excitation λ_{ex} = 530 nm, fluorescence emission at λ_{em} > 545 nm.

We investigated the transfollicular penetration and bioavailability of the model drug Nile Red (NR) encapsulated in the pH-sensitive polymeric nanocarrier Eudragit® using our confocal FLIM setup. For this purpose, a skin area of 2x3 cm was treated with 20 µL/cm² aqueous solutions containing 2% Eudragit® L100 loaded with 50 µg/ml Nile Red. The skin area was massaged for 2 min and followed by incubation for 30 min at 32°C. Afterwards, any remaining supernatant was removed and biopsies were shock frozen for subsequent cryosectioning resulting in 10 µm thick sections. Results of FLIM measurements are shown in Figure 4-20 and Figure 4-21, fit results from fluorescence decay fits are summarized in Table 5. The hair follicle has naturally a very high level of autofluorescence which creates a challenge to identify location and abundance of any fluorescent probe based on the fluorescence intensity information alone (Figure 4-20D, G). We overcome this problem by discriminating the target fluorescence of Nile Red from the autofluorescence based on the fluorescence lifetime using Cluster-FLIM[152] and are thus capable to generate background free penetration profiles. As can be seen in (Figure 4-20E, H), autofluorescence of the hair follicle and the surrounding tissue is represented by the green and light green fluorescence decay cluster. On the other hand, we see a significantly slower decay of our target fluorescence (NR), depicted as red decay cluster in Figure 4-20H. With this technique, we now compare the penetration through the *stratum corneum* into deeper skin layers (Figure 4-21, ROI 1) to lateral penetration of NR at different depths in the hair follicle into the dermis (Figure 4-21, ROI 2 & 3). ROI 1 in Figure 4-21 shows the transepidermal penetration route taken by NR into deeper skin layers. Here we see a sharp drop of

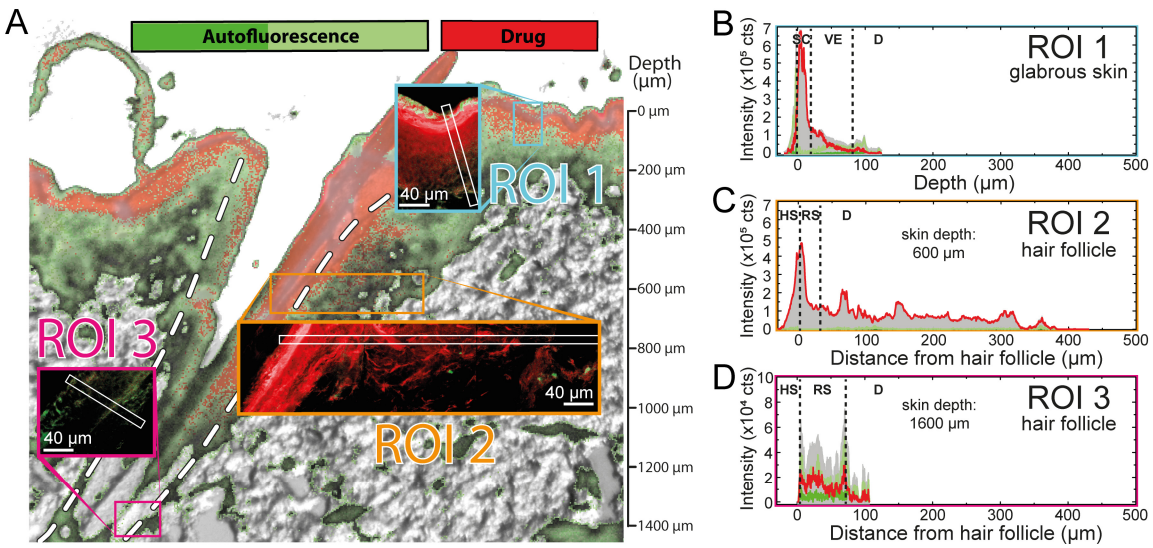

Figure 4-21. Nile Red penetration profiles at the skin surface (ROI 1, cyan), the hair shaft (ROI 2, orange) and the hair root sheath (ROI 3, magenta). False color images based on fluorescence lifetime, shown in Figure 1B). Experimental conditions: see Figure 4-20.

intensity just after the *stratum corneum* at 20 µm and only negligible amounts past the viable epidermis at 100 µm. This penetration profile compares well to previous findings with similar loaded Eudragit® L100 nanoparticles[157]. Here, the high concentration of NR in the SC is attributed a reservoir function of the SC for the nanoparticles. A decreased packing order of the lipids in the outermost SC layer facilitates the initial uptake and retention of the nanoparticle in the SC[157]. In contrast, ROI 2 (Figure 4-21C) shows the lateral penetration from hair shaft appx. 600 µm deep in the hair follicle into the adjacent dermis. Significant amounts of NR can still be detected >400 µm away from the hair follicle. The higher lateral diffusion into the dermis is enabled by the weaker barrier function of the inner root sheath compared to the SC of glabrous skin[193]. Assuming a radial diffusion pattern around the hair follicle and an average hair follicle density of 22 follicles/cm²[194], about 11% of the skin area would be supplied just due to lateral diffusion from the hair follicle into the dermis. Thus, Cluster-FLIM proved the enhanced drug delivery into the dermis via nanoparticle-assisted transfolliclular penetration route. Even at the hair root sheath, 1600 µm deep into the hair follicle (Figure 4-21D), Cluster-FLIM was able to identify traceable amounts of NR, twice as deep as found in previous studies[157]. We attribute this finding to the unambiguous discrimination between target fluorescence and autofluorescence only possible with Cluster-FLIM. Traditional methods which identify target fluorescence by intensity threshold tend to underestimate target fluorescence in highly autofluorescent tissue like in the hair follicle. Thus, we could verify nanoparticle-assisted drug penetration via the hair follicle into skin depths which would be unreachable through conventional transepidermal penetration routes. In addition, pH increases with skin depth[195], favoring a release of the drug mimetic from the nanoparticle. Hence, the penetration profiles show

that there is minimal chance to have high yield in dermis via the *stratum corneum* path, but there is high penetration with particle/NR into dermis via the hair follicle.

Table 5. Fit parameter of FLIM clusters of NR with and without Eudragit® in the hair follicle (Figure 4-20, Figure 4-21) and glabrous skin (Figure 4-22). Autofluorescence is represented by the green and spring green FLIM cluster. τ_i: fluorescence lifetime of the i-th decay component in ns, α_i the corresponding relative amplitude in %, $\bar{\tau}_{pop}$: mean fluorescence lifetime (eq. (6)) and χ^2: reduced chi square. The goodness of the fit was judged from the reduced χ^2 and the residuals. Fluorescence decay curves were fitted with the sum of n exponentials. A satisfactory number of exponentials was reached when neither the χ^2 nor the residuals improved when fitting with n+1 exponentials. As an example, the 4-exponential fit of the autofluorescent component (green) in the NR/Eudragit® experiment is given, which doesn't improve the χ^2 but also does not change the mean fluorescence lifetime. The errors of the mean fluorescence lifetime were determined to be within 0.4-1.5%, representing the accuracy of the fit.

	FLIM cluster	α_1(%)	α_2(%)	α_3(%)	α_4(%)	α_5(%)	τ_1(ns)	τ_2(ns)	τ_3(ns)	τ_4(ns)	τ_5(ns)	χ^2	$\bar{\tau}_{pop}$ (ns)
NR/ Eudragit®	red	28.2	50.7	21.1	-	-	0.38	2.60	4.58	-	-	1.7	3.30
	green	67.3	31.0	1.7	-	-	0.80	2.90	8.39	-	-	2.1	2.67
		65.8	25.0	8.4	0.8	-	0.79	2.56	4.00	10.12	-	2.1	2.67
	spring green	37.3	40.2	21.3	1.2	-	0.41	1.68	3.80	6.59	-	1.8	2.79
NR	red	31.0	34.8	26.4	7.3	0.6	0.71	2.1	3.79	5.56	12.66	2.1	3.55
	blue	63.5	24.8	10.7	0.9	0.2	0.29	1.19	3.12	5.79	11.78	2.0	2.25
	magenta	62.8	23.4	11.1	2.4	0.3	0.23	0.73	2.00	3.48	8.82	1.8	1.75
	green	48.1	33.7	17.1	0.9	0.3	0.34	1.50	3.85	8.45	11.82	1.8	3.04

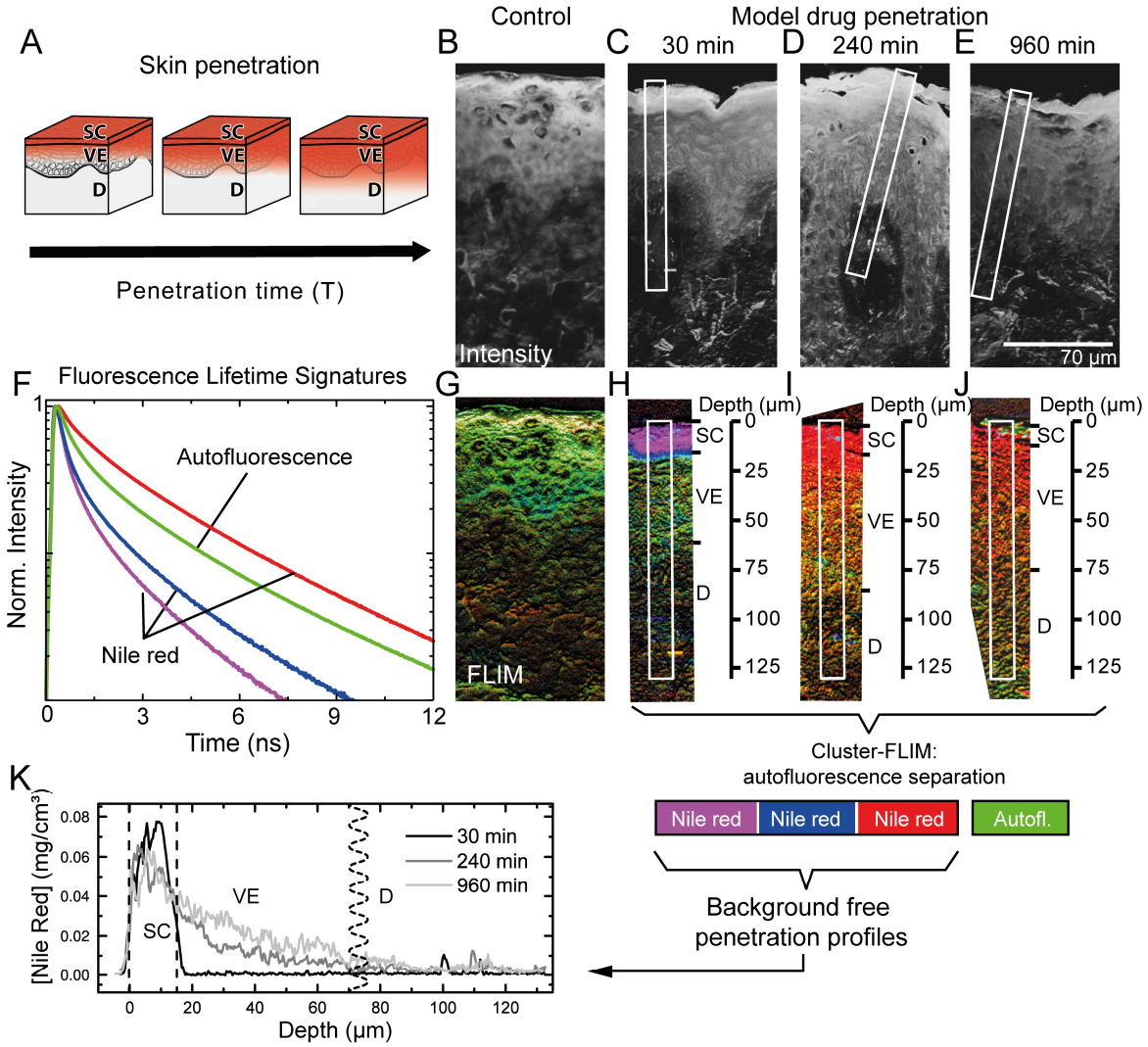

Figure 4-22. (A) Scheme of the experimental setup (B-E) Fluorescence intensity images of time-dependent Nile Red penetration profiles after 30, 240 and 960 min. (F) Fluorescence decay curves of Nile Red found in the penetration experiments (G-J) FLIM images of Nile Red penetration in skin, false color based on fl. decay shown in (F). (K) Nile Red penetration profiles generated from photon counts in the marked areas of (H-J). Experimental conditions: see Figure 4-20.

In a next step, we were interested in dynamic properties of the NR penetration into skin. For that purpose, we detected specific penetration profiles of topically applied NR, after different times of incubation (Figure 4-22). Pierre Volz-Rakebrand performed these measurements. As apparent from Figure 4-22B-E, the background fluorescence intensity is comparable to the target fluorescence of NR. But, as shown in the previous section, Cluster-FLIM allows for the subtraction of the skin autofluorescence on the basis of its differing fluorescence decay to yield background free penetration profiles (Table 5, Figure 4-22K). The intensity of the target fluorescence clusters was then converted into a concentration profile with the help of a NR concentration calibration (Figure 4-22K). These penetration profiles were then subject to numerically modelled diffusion analysis, done by Amanuel Wolde-Kidan in the group of Prof. Netz (Physics Department, FU Berlin, Germany). Figure 4-23 shows re-scaled experimentally measured concentration profiles (Figure 4-22K) in

comparison to the results of the numerical modelling. Computed penetration profiles reproduce the experimental data nicely with an average error of $\sigma = 0.003\ mg/cm^3$, equivalent to a relative error of less than 10%. The NR molecules are taken up quickly into the first layers of the skin, the *stratum corneum* (SC), were they accumulate. The immediate uptake is driven by the low water content (~15%[196]) and high concentration of ceramides, phospholipids and cholesterol[197,198] packed into highly ordered lamella, which results in a minimum of free energy $\Delta F_{SC-sol} \approx (-1.10 \pm 0.01)\ k_B T$ in the SC for this lipophilic dye. The analysis suggests an immediate uptake of NR into the SC, seconds after application (Figure 4-23B). However, further penetration from the SC into the subjacent epidermal layers occurs only after a delay of several minutes to hours. This characterizes the SC as a reservoir for NR penetration.

The minimum in free energy for NR might be explained by the lipophilic milieu of the densely packed intercellular lipids, allowing for a high fraction of NR, which has a logP value of 3.8[199]. While we see a net negative ΔF in the lipid rich SC and *stratum granulosum* (SG), the free energy strictly increases with skin depth, presumably caused by changes in hydrophilicity and mechanical structure of the environment, i.e. by the reduction in lipid dry mass in this region[108,196]. An increase of free energy in the VE has been reported before for the lipophilic drug dexamethasone [190], though slope of the free energy increase seems to be proportional to the partition coefficient of the compound. While NR with a logP of 3.8 experiences a difference of free energy between the SC and D of $\Delta F_{SC-D} = (2.3 \pm 0.5)\ k_B T$ (Figure 4-23C), dexamethasone, being less lipophilic with a logP of only 1.8[200], sees an increase of free energy of only $\Delta F_{SC-D} \cong 1\ k_B T$[190] over the same distance. So, our findings clearly supports the standing notion that the epidermis, and the SC in particular, acts as a lipophilic drug reservoir after initial uptake sink with high lipophilic affinity whereas the dermis is characterized as essentially hydrophilic[190], reflected in an increase of free energy to $F_D = 7.88\ k_B T$ (Figure 4-23C).

The numerical modeling approach also provides an independent diffusivity profile for the model drug on which I will focus next. NR in aqueous solutions exhibits a diffusion constant of $D_{sol} \approx (335.55 \pm 225.84)\ \mu m^2/s$ (Figure 4-23D), which is also found in the literature for small lipophilic fluorescent dyes.[201] In the SC, D drops by several decades, consistent with earlier reports[190]. The low diffusivity leads to an immobilization of NR up to a depth of 16 µm. As discussed earlier, this retention leads to a non-monotonic penetration behavior, as can be seen in the time-dependent decrease of NR in solution and its uptake into the skin layers (Figure 4-23B). Values for the diffusion constant in this region lie between $D_{SC} \approx 0.01 - 42.87\ \mu m^2/s$ (Figure 4-23D), which agree with

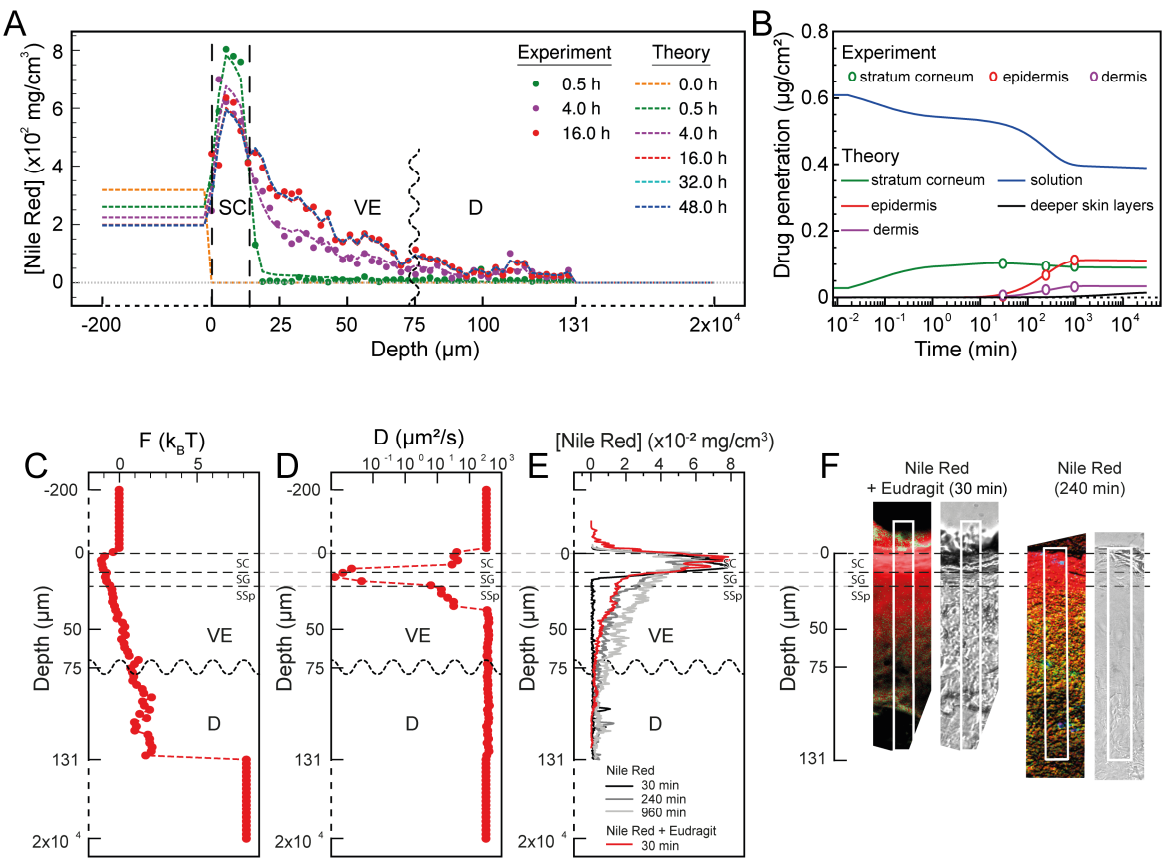

Figure 4-23. Results from the numerical model of Nile Red penetrating in human skin. (A) Numerically computed profiles (dashed lines) in comparison to experimentally measured data (data points). Numerical data agree well to experimental measurements. (B) Computed drug concentration in different skin layers over time. (C) Free energy landscape and (D) diffusivity profiles obtained from the fit. The different skin layers are indicated as *stratum corneum* (SC), *stratum granulosum* (SG), *stratum spinosum* (SSp), viable epidermis (VE), and dermis (D). (E) Comparison of NR penetration in glabrous skin with and without Eudragit® nanoparticles. (F) Comparison of FLIM images for 30min penetration of encapsulated NR (Figure 4-20, ROI 1) with 240 min penetration of free NR (Figure 4-22D,I) in glabrous skin. Theoretical modeling by Amanuel Wolde-Kidan.

values obtained for NR diffusing in cellular membranes[202], or other comparable lipophilic dyes diffusing in lipidic environments[203]. In the subjacent skin layer, the *stratum granulosum* (SG), the diffusion constant continuously increases from 16 µm to 22 µm. In the SG, cell-cell adhesion points, the tight junctions, form a selective diffusion barrier. They mainly consist of the membrane bound proteins occludin, claudins and zonula occludens (ZO). Claudins are expressed evenly over the majority of the viably epidermis. Occludins, on the other hand, are exclusively found in the SG. ZO-1 is present from the SG to the *stratum spinosum* (SSp) but decreases in concentration with increasing skin depth. Note that the differentiation-dependent expression of the ZO proteins is an integral factor for the formation of functional tight junctions.[198,204] This is well reflected in the gradual increase of diffusivity in a skin depth of 22 µm to 40 µm, where it finally reverts to free diffusion,

$D_{VE} \approx 376.47 \pm 210.01\ \mu m^2/s$ in the epidermis and $D_D \approx 325.99 \pm 225.20\ \mu m^2/s$ in the dermis.

Steady-state equilibrium of the diffusion process is reached after 16 h of penetration. A total of 37% of the initial NR applied to the skin sections is taken up, while the rest remained in solution (Figure 4-23B). This leads us to the conclusion that lipophilic compounds are limited in their ability to reach deeper skin layers despite the SCs reservoir function.

When comparing penetration profiles of free NR with NR loaded nanoparticles in glabrous skin, one finds the same qualitative distribution of NR in the different skin layers. However, the nanoparticle assisted penetration of NR after 30 min achieves a NR concentration in the VE which is comparable to the penetration of free NR after 240 min (Figure 4-23E,F), implying an 8 times faster uptake into the skin. This improvement probably results from a reduction of SC barrier by the nanoparticle. Since no uptake into the dermis can be observed, we suspect that the nanoparticle Eudragit® L100 only helps to overcome the diffusion barrier between SC and VE. In addition, the transfollicular penetration route offers great potential for the nanoparticle assisted drug delivery as the nanoparticle size enables the translocation deeper into the hair shaft after topical application[188]. The increased pH in deeper skin layers triggers the drug release from the Eudragit® nanoparticle and facilitates the lateral diffusion into the dermis benefitting from the absent SC barrier in the hair follicle. Hence, the detailed dissection of the diffusivity profile and free energy landscape of NR representing a lipophilic drug mimetic in skin and the comparison to the nanoparticle assisted penetration of the same compound allowed us to gain valuable insight into the physicochemical properties of the skin and the penetrating agent which govern effective dermal and transdermal drug delivery.

4.2.2 Drug interaction with tumor-microenvironment of epithelial mucosa squamous cell carcinoma model

The goal for targeted drug delivery systems is to exclusively route the therapeutic agent to the pathological tissue, which results in high drug efficacy while eliminating side effects. Therefore, biophysical parameters such as drug diffusivity profiles of healthy and diseased tissue provide valuable information to exploit the unique features of the pathological tissue in order to develop targeted delivery strategies. In the context of tumor targeting, this field of research is called transport oncophysics[187]. In this chapter, I investigated the penetration of the anticancer drug cetuximab through diseased tissue and analyzed the cell interaction profile using biophysical methods.

Head and neck squamous cell carcinoma (HNSCC) is one of the most common cancers type with also poor prognosis. Common therapy options including surgery, radiotherapy, chemotherapy or their combination can not achieve better five-year survival rates than 50% in patients with locally advanced diseases, leading to 450.000 deaths worldwide in 2018[205,206]. Pharmacotherapy often falls short in this type of cancer due to emerging chemoresistance or severe systemic side effects ensuing from dose escalation. The introduction of new antibody based drugs like cetuximab, nivolumab, or pembrolizumab improved the outcome but did not overcome the fundamental problem of primary or acquired treatment resistance in the majority of patients[207]. Hence, a deeper understanding of the underlying mechanism of drug-cancer interaction on the molecular level is pivotal to the development of more effective treatment strategies. The significance of research derived from animal models suffer from pathophysiological differences to humans[208] and monolayer models constructed from primary human tumor cells lack the microenvironment of tumors. Therefore, human derived 3D tumor tissue models are urgently needed to overcome these limitations and progress the development of new drugs in preclinical trials. The group of Prof. Schäfer-Korting (Department of Pharmacy, FU Berlin, Germany) recently developed models from patient derived HNSCC xenografts and characterized the phenotype[141]. These multi-layered HNSCC models contain important oral mucosal components, hence, resembling the tumor morphology and microenvironment more closely. First tests indicate cetuximab-resistant tumor cells as five systemic applications of 100 µg/ml results only in minor changes to epithelial thickness in UM-SCC-22B models and no changes in SCC-25 models with an additionally high proliferation index at the end of the culture period[141]. In a cooperation between the groups of Prof. Schäfer-Korting and Prof. Alexiev (Physics Department, FU Berlin, Germany), we aim to understand key regulators of drug interactions with this tumor oral mucosa (TOM) models, which may contribute to the introduction of topical therapy in clinical practice for HNSCC treatment to mitigate systemic side effects[209].

4.2.2.1 Cetuximab labeling with FITC

I labeled cetuximab with fluorescein isothiocyanate yielding Cetuximab-FITC. Isothiocyanate reacts with amines to form a stable thiourea linkage [210]. As proteins, like cetuximab, contain primary amines, protein fluorescence labeling via isothiocyanates emerged as a common protein stain in microscopy experiments[211] and in spectroscopic experiments on the molecular level. The detailed labeling procedure is presented in chapter 3.16. Figure 4-24A shows the absorbance spectra of the eluted fractions of FITC labeled cetuximab after a Sephadex G25 column. Figure 4-24B shows normalized spectra to calculate FITC contribution to the protein absorbance at 280 nm. The labeling stoichiometry was calculated using eq. (36) and is presented in Figure 4-24C. The main fractions F8

and F9 exhibit a stoichiometry of about 6 FITC labels per cetuximab molecule. The 6 labeling sites are out of 23 potential labeling sites, which are presented in Figure 4-25.

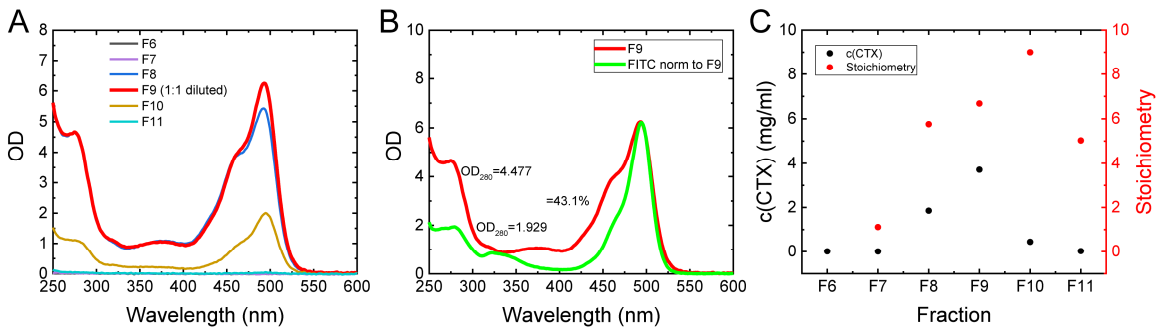

Figure 4-24. Cetuximab (CTX) labeling with FITC. (A) Absorbance spectra of fractions (F6-F11) after Sephadex G25 column. (B) FITC contribution to the protein absorption peak at 280 nm. (C) Cetuximab concentration found in the eluded fractions to calculate labeling stoichiometry corrected for FITC absorbance at 280 nm.

4.2.2.2 Cetuximab receptor binding in the cell membrane

The epidermal growth factor receptor (EGFR) is involved in many ligand-induced signaling cascades including cell proliferation, motility, and differentiation [212]. Alteration in these signaling pathways may lead to malignant transformations, which is why the EGFR is often involved in cancer pathogenesis[213]. Cetuximab binds exclusively to the domain III of the EGFR[214] (Figure 4-25) and thereby sterically prevents ligand binding in the tumor cells, rendering it a potent anti-cancer drug.

First, I tested whether cetuximab-FITC still binds to the membrane receptor EGFR after labeling. Membrane binding of cetuximab-FITC was verified in cell monolayers of SCC-25 cells (Figure 4-26I). In a next step, cetuximab-FITC was applied to multi-layered SCC-25 tissue models for 12 or 48 h, either systemic or topically. Systemically means the addition of cetuximab-FITC in the cell medium reservoir from below and topically describes the application from the top, directly onto the tissue model. The constructs were snap frozen and cut into 7 µm slices by a cryotome (Leica CM 1510 S; Leica, Wetzlar, Germany) and subjected to FLIM. Then, I mapped cetuximab cell binding in TOM models after topical and systemic administration with the help of Cluster-FLIM (Figure 4-26). Cluster-FLIM is able to quantify drug penetration due to the discrimination between target fluorescence of the FITC labeled drug cetuximab and the autofluorescence background which subsequently generates background free penetration profiles.

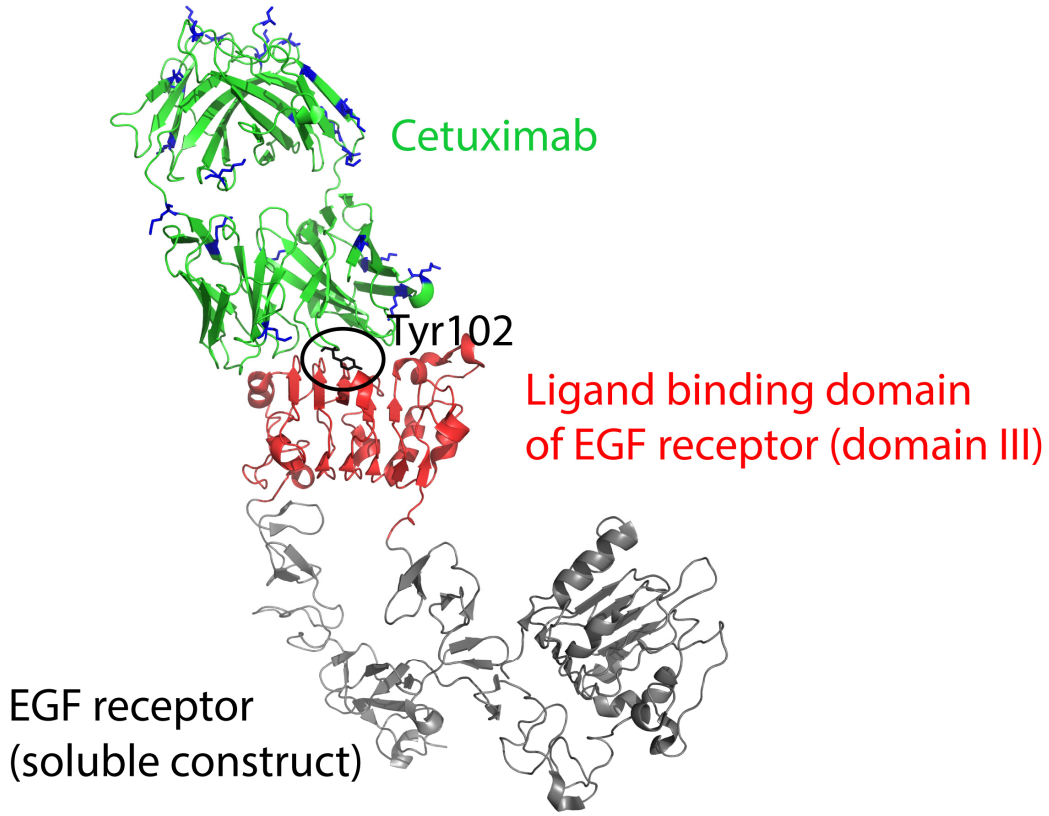

Figure 4-25. Binding of cetuximab (green) to the domain III (red) of the epidermal growth factor receptor (EGFR) (PDB 1YY9). The tyrosine 102 occupies the same binding pocket of domain III of EGFR as the leucine 47 of the epidermal growth factor (EGF) would, which inhibits the EGFR activation. All lysines of cetuximab which can be labeled by FITC are shown in blue.

From the three observed clusters (yellow, cyan, and red, Figure 4-26F) in the 3D model, only the yellow cluster is unique to the measurement of drug penetration and did not overlap with autofluorescence contributions to the cyan and red FLIM cluster. Based on the spatial localization of the yellow cluster and the resemblance with the fluorescence decay found in monolayer experiments (Figure 4-26I), we assigned the yellow fluorescence cluster to FITC labeled cetuximab interaction with the tumor cells (Figure 4-26B, G). The cyan and red fluorescence clusters, on the other hand, both include contributions of autofluorescence (Figure 4-26H). Nonetheless, the high photon counts of the cyan cluster in the lamina propria signals the presence of a significant amount of cetuximab, as seen clearly when comparing Figure 4-26C (control) with Figure 4-26E, the highest dose of cetuximab in systemic application. In more detail, in SCC-25 models, with a dose of 10 µg/ml, we observe low but homogeneous cetuximab-FITC penetration after topical and systemic application (Figure 4-26A, D). With a higher dose of 100 µg/ml, clear differences between systemic and topical administration become visible regarding drug concentration in the tissue (Figure 4-26B, E). Based on the respective penetration profiles, one gathers a 2-fold higher drug concentration in

the epidermal layer of the tumor model with systemic application (Ø $1.5x10^5$ counts) compared to topical application (Ø $3.3x10^5$ counts). In the subjacent lamina propria, even an 11-fold increase can be observed for systemic application (Ø $7.6x10^5$ counts in systemic application, Ø $0.7x10^5$ counts in topical application). As Cluster-FLIM is also able to discriminate different microenvironments of the fluorophore based on its fluorescence lifetime, we analyzed the occurring FLIM clusters of topically applied 100 µg/ml dose and a control sample with 60x magnification (Figure 4-26G, H) and also investigated a second tissue model derived from UM-SCC-22B cells. We studied the dose dependency of penetration profiles in these models after systemic application. Again, we found increased penetration (cyan cluster) and cell interaction (yellow cluster) for the higher dose. In Figure 4-26L, we quantify the cetuximab-FITC cell interaction (yellow cluster). Note that significant tumor cell interaction can be found in the SCC-25 and UM-SCC-22B models regardless of dose and application mode from the FLIM experiments (Figure 4-26G, J). Nonetheless, no cytotoxic anti-cancer properties of cetuximab can be found in the SCC-25 model and only slight decrease in cell viability for the UM-SCC-22B model was observed by our collaborators, indicating resistance of SCC-25 and UM-SCC-22B cells against cetuximab in the 3D model but a slight pharmacological effect was observed in the cell monolayer experiments[141]. Everything considered, cetuximab reaches and interacts with the tumor cells of the 3D model but is not effective under the local conditions. These findings underline the relevance of biophysical techniques to visualize and analyze drug interactions and pharmacology in living tissue.

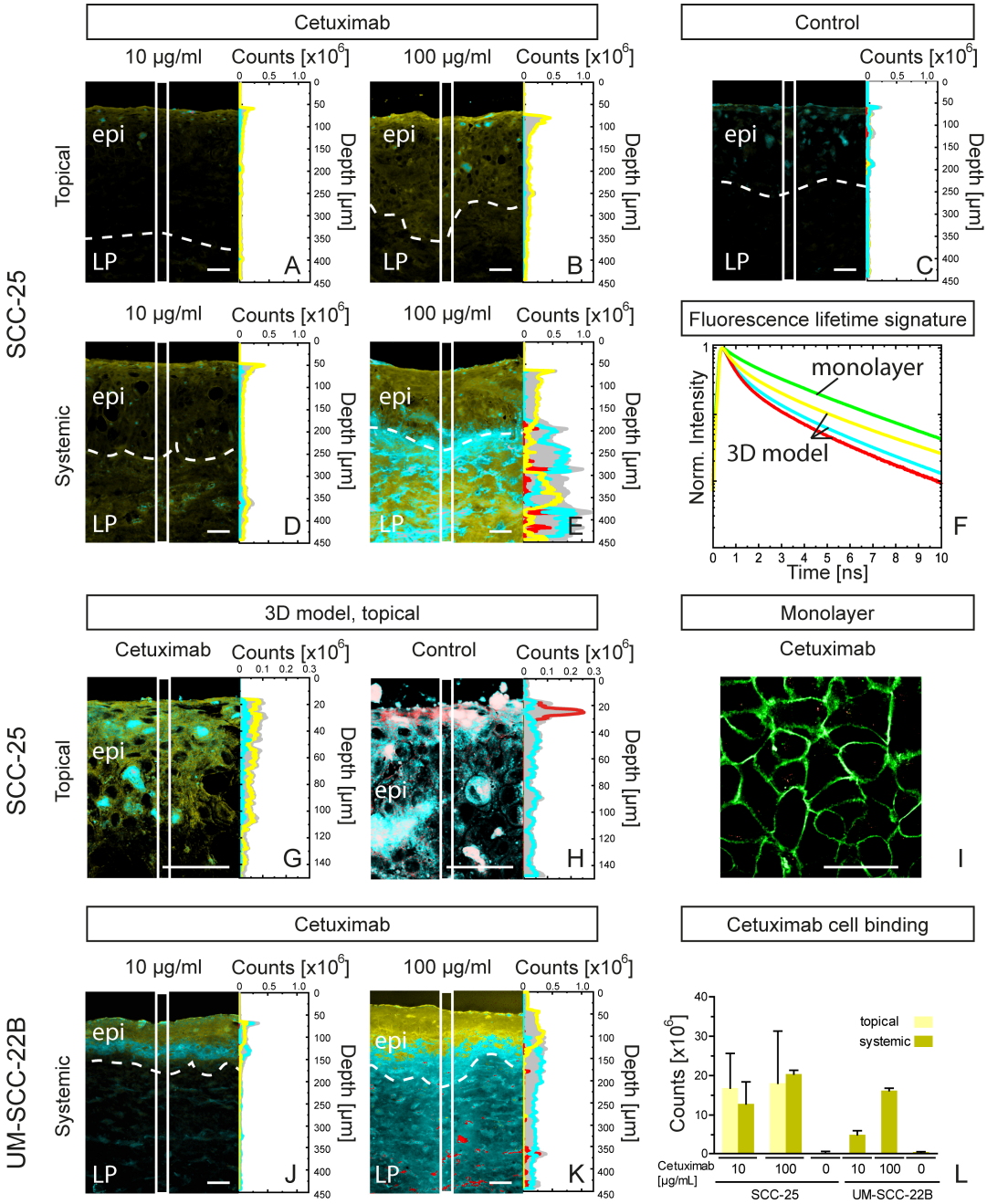

Figure 4-26. Cetuximab-FITC penetration in SCC-25 and UM-SCC-22B models and cell interactions. (A, B, D, E, G) Cluster-FLIM images of Cetuximab-FITC penetration into SCC-25 models and UM-SCC-22B models (J, K) as well as vehicle control (C, H) after 48h incubation. Epidermis (epi), lamina propria (LP). Penetration profiles resolved for fluorescence cluster contribution of the marked area are shown on the right of each FLIM image. The gray area represents total fluorescence intensity. False-color coding of FLIM images and penetration profiles according to fluorescence decays shon in (F). (G-I) Comparison of 3D tissue model and cell monolayer experiments after 100 µg/ml (3D model) and 50 µg/ml (monolayer) drug application. (L) Quantification of the yellow FLIM cluster of cetuximab-FITC in the epithelial layer. Scale bar = 50 µm. Experimental conditions (A, B, C, D, E, J, K): objective 20x, λex= 488 nm, λem>515 nm, 300 s integration, pinhole= 0.5 airy units; (G, H, I): objective 60x, λex= 488 nm, λem>515 nm, 300 s integration, pinhole= 0.25 airy unit. Adaptation with permission from [141].

4.3 Multiplexed FLIM-EPR spectroscopy: a dual fluorescence-spin label probe for the visualization and quantification of target molecules in tissue

The quantification of molecules of interest in tissue usually requires invasive procedures, including time-consuming steps of tissue homogenization, and performing analysis such as chemical extraction of the sample. Hence, spectroscopic techniques for direct, non-invasive, and spatially resolved concentration quantification are highly attractive for research ranging from fundamental biology to drug delivery assessments. Conventional fluorescence microscopy as a direct quantitative tool for the determination of concentration in tissue has been explored but remains challenging [215-217], mostly due to scattering and absorption of the excitation and the emitted fluorescence light, as well as the autofluorescence in the tissue. However, fluorescence lifetime imaging microscopy (FLIM) has recently received a lot of attention as a sensitive tool for visualizing the spatial distribution of endogenous and exogenous fluorescent molecules at the subcellular and suborganelle level[14,15,21,22]. FLIM is a technique for spatially visualizing fluorophores by measuring fluorescence intensity and lifetime. Fluorescence lifetime is an intrinsic property of a fluorophore and usually independent of fluorophore concentration and optical loss in the sample, enabling FLIM of high sensitivity and signal specificity[218,219]. Furthermore, fluorescence lifetime is sensitive to the local environment and can reveal biomolecular interactions, changes in pH and viscosity and reactive oxygen species[17,18,23]. EPR is an efficient tool to quantify the absolute number of spin-labeled drugs in skin according to that the double integral of EPR spectral lines is proportional to the numbers of spin-labeled drugs. It allows for measurements of skin tissues in large volumes, which provides a holistic understanding of the microenvironment around the spin-labeled drugs but also limits its spatially resolution to approximately 50-100 μm[220]. Besides, EPR provides information about the microenvironments surrounding spin-labeled drugs, such as polarity, pH and viscosity[27,28].

Up to now, the biomolecule of interest in general is singly labeled: a fluorophore label for studying biomolecular dynamics and interactions[16,19,221], or visualization and tissue distribution by FLIM[15,18,143,222,223]; and a spin label for quantification of target molecules in tissue or their dynamics by EPR[27,28,157,224-229]. Combining both labels into a single probe proved to be difficult since the fluorophore is prone to heavy quenching by the unpaired electron of the spin probe[20,43,230-232]. However, individual labeling of the molecule of interest with a fluorophore or spin label could change its physicochemical properties, such as the logP-value, and thereby tissue penetration[233]. Combining the strength of FLIM and EPR, we envisioned a dual label (DL) for multiplexed FLIM and EPR measurements. So, in this section, I will outline the development of this novel platform for dual-labeled compounds and present the basic spectroscopic characterization of the final

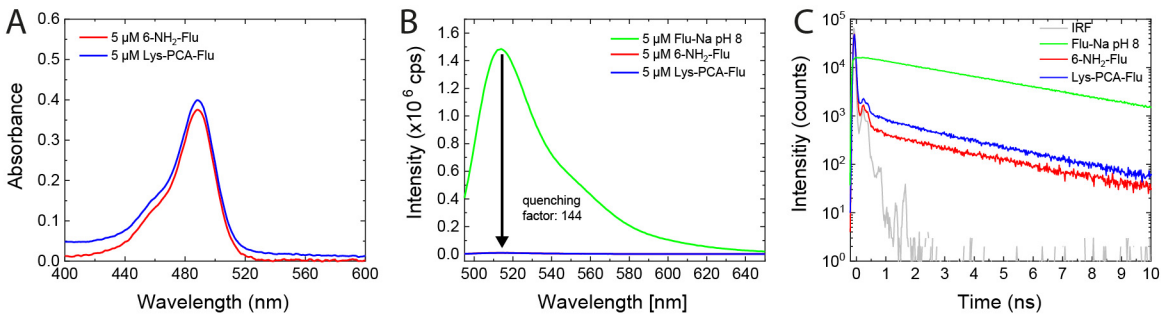

Figure 4-27. Characterization of a dual-label utilizing 6-aminofluorescein as a fluorophore. (A) Absorbance spectrum of 5 µM 6-aminofluorescein and the dual-label Lys-PCA-aminofluorescein (B) Emission spectra of the dianionic fluorescein sodium salt with a quantum yield of QY=0.93 [235] and for comparison the emission spectrum of the non-fluorescent aminofluorescein and PCA-Lys-aminofluorescein. Usually, this fluorescein derivative recovers its fluorescence after labelling [234] which was not the case in this configuration. This quenching may be due to reactions of the PCA radical in the presence of the aminofluorescein. (C) Fluorescence lifetime curve of fluorescein sodium salt compared to the lifetime curves of the unreacted aminofluorescein and the labeled aminofluorescein, which show the strong quenching.

compound which reveals a concentration dependence of the fluorophore Rhodamine B when in conjugation with the spin probe PCA. After calibration, this property is then used for proof-of-principle experiments in skin tissue, comparing the spatially resolved concentration of the target compound determined by EPR, fluorescence intensity, and fluorescence lifetime.

In a first attempt we produced a dual-label compound which uses 6-aminofluorescein as the fluorophore, 2,2,5,5-tetramethyl-1-pyrrolidinyloxy-3-carboxylic acid (PCA) as the spin probe and a lysine (Lys) as trifunctional linker (Figure 4-27). Aminofluorescein by itself is a non-fluorescent compound which recovers its quantum yield after labeling of the amine group[234]. As can be seen in Figure 4-27, this is not the case when in conjugation with PCA. While the vicinity to PCA has no noticeable influence on the absorbance spectrum (Figure 4-27A), the emission of aminofluorescein and the Lys-PCA-Flu compound is quenched by a factor of almost 150 when compared to the dianionic form of fluorescein as the sodium salt with a quantum yield of QY=0.93[235]. A compound with that low fluorescence is unusable in studies and was not pursued any further.

In a next attempt, we exchanged aminofluorescein for Rhodamine B (RhoB) and added a piperazine as a spacer between both labels (Figure 3-7) which proved to be enough for the PCA to not significantly quench RhoB's fluorescence. Figure 4-28 shows the spectroscopic characterization of the newly designed DL and its precursors. RhoB in aqueous solutions has an absorbance maximum at $\lambda_{abs} = 555\,nm$ and highest fluorescence emission at $\lambda_{em} = 581\,nm$. It exhibits a monoexponential fluorescence decay with a decay time of $\tau = 1.7\,ns$ (Table 6). The addition of the piperazine to RhoB at its carboxy-phenyl group introduces a bathochromic shift of RhoB's

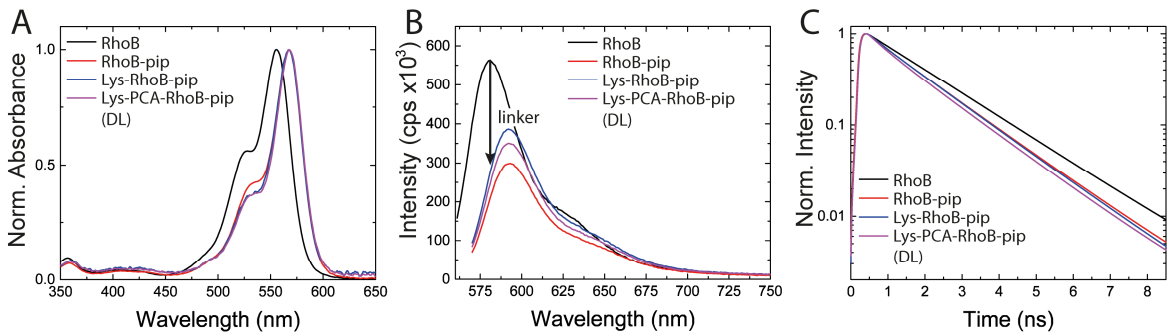

Figure 4-28. Characterization of DL in solution (A) Absorbance spectra of Rhodamine B (RhoB), DL, Rhodamine B-piperazine, and Boc-Lys-RhoB-piperazine for comparison. (B) Emission spectra. The highest quenching of Rhodamine B fluorescence occurs upon addition the linker piperazine between PCA and Rhodamine B. (B) Fluorescence decay curves. Experimental conditions for lifetime curves: λ_{ex} = 530 nm, λ_{em} > 545 nm.

absorbance and emission maximum a $\lambda_{abs} = (567 \pm 1)\, nm$ and $\lambda_{em} = (592 \pm 1)\, nm$, and also adds a second decay component, shortening the mean fluorescence lifetime to $\bar{\tau} = 1.5\, ns$ (Table 6), which is consistent with known effects on RhoB emission, quantum yield, and fluorescence lifetime depending on the condition of the carboxy-phenyl group [236,237]. The fluorescence was only slightly quenched by a factor of $Q_f = 1.6$, an outstanding result, especially when compared to the $Q_f = 144$ of the aminofluoresceine. Further addition of the Lysine linker and the PCR did not change RhoB's fluorescence properties in any significant manner (Figure 4-28, Table 6). For the final compound DL, a quantum yield ϕ = 0.18 ± 0.03 was determined using RhoB in ethanol (ϕ = 0.7 at 20°C [236]) as reference. The logP-value of 0.07±0.05 for DL reveals good water solubility. RhoB provides plenty fluorescence signal and, in combination with PCR, proves to be a promising platform for functional DL. Furthermore, I demonstrated the stability of DL against endogenous tissue enzymes, e.g. esterases, to ensure the comparability of EPR and FLIM results from tissue experiments.

One goal of this project was it to compare both methods, fluorescence and EPR, in their capabilities to characterize a biological sample and how a labeled compound interacts with it. As a model system we chose human skin as it is comprised of various distinct microenvironments, i.e. the lipid rich cornified outer layer in the *stratum corneum*, a cellular layer in the epidermis and also connective tissue in the dermis, with much lower cell concentration but rich in collagen and elastin fibers. In drug efficacy of topically applied drugs, it is often a high priority to know the penetration behavior of compound of interest after topical application and its subsequent quantification in the tissue. Two information are needed for the determination of DL concentration in skin via fluorescence: a) the stability of DL during incubation with skin, and b) the correlation of

fluorescence intensity and lifetime with DL concentration. We investigated the stability by mimicking the conditions of incubation in a petri dish without skin, with the DL solutions spread to increase surface area, but such that we were able to compare absorbance and emission from before and after the incubation (Figure 4-29). Over 2 h exposure of the DL solution to normal air at 32°C, we found a decrease of fluorescence intensity by a factor of F_r=1.8, most likely due to oxidation of the fluorophore. The fluorescence lifetime, on the other hand, remained unchanged (Figure 4-29C).

Table 6. Fit parameter of Lys-PCA-RhoB (DL) and its precursors in FLIM experiments shown in Figure 4-28 through Figure 4-32 . τ_i: fluorescence lifetime of the *i*-th decay component in ns, β_i the corresponding fractional amplitude in %, $\bar{\tau}_{pop}$: mean fluorescence lifetime and χ^2_{red}: reduced chi square. The presented errors are the standard deviation resulting from repeated fitting of the data (n=5) to give an impression of the accuracy of the fit. Decay curves of DL and its precursors with fit curves and residuals are shown in Figure A2. The larger χ^2_{red} originates from the high photon counts collected in the FLIM setup for the dye solutions. For the FLIM setup, an error of <1% was observed for $\bar{\tau}_{pop}$. Experimental conditions: λ_{ex} = 530 nm, λ_{em} > 545 nm.

Sample	$\boldsymbol{\beta_1}(\%)$	$\boldsymbol{\beta_2}(\%)$	$\boldsymbol{\beta_3}(\%)$	$\boldsymbol{\tau_1}(\mathrm{ns})$	$\boldsymbol{\tau_2}(\mathrm{ns})$	$\boldsymbol{\tau_3}(\mathrm{ns})$	$\boldsymbol{\chi^2_{red}}$	$\boldsymbol{\bar{\tau}_{pop}}(\mathrm{ns})$
RhoB	100			1.700 ±0.004			3.8 ±0.4	1.700 ±0.004
RhoB	5.3 ±5.9	94.7 ±5.9		1.0 ±0.4	1.71 ±0.02		3.4 ±0.5	1.69 ±0.01
RhoB-pip	5.3 ±1.0	94.7 ±1.0		0.66 ±0.08	1.534 ±0.005		1.7 ±0.1	1.488 ±0.001
Lys-RhoB-pip	4.5 ±1.2	95.5 ±1.2		0.6 ±0.1	1.51 ±0.01		1.7 ±0.2	1.470 ±0.005
Lys-PCA-RhoB-pip (DL)	8.3 ±0.5	91.7 ±0.5		0.52 ±0.03	1.492 ±0.004		1.78 ±0.05	1.412 ±0.002
FLIM cluster								
Blue	7.51	85.35	7.14	0.95	2.99	5.29	1.8	3.0
Cyan	14.38	60.00	25.61	0.96	2.50	3.86	4.6	2.6
Yellow	17.43	67.79	14.78	0.81	2.32	4.30	3.4	2.3
Orange	21.03	60.35	18.63	0.65	1.88	3.86	1.3	2.0
Red	38.24	50.79	10.97	0.54	1.55	6.27	1.3	1.7

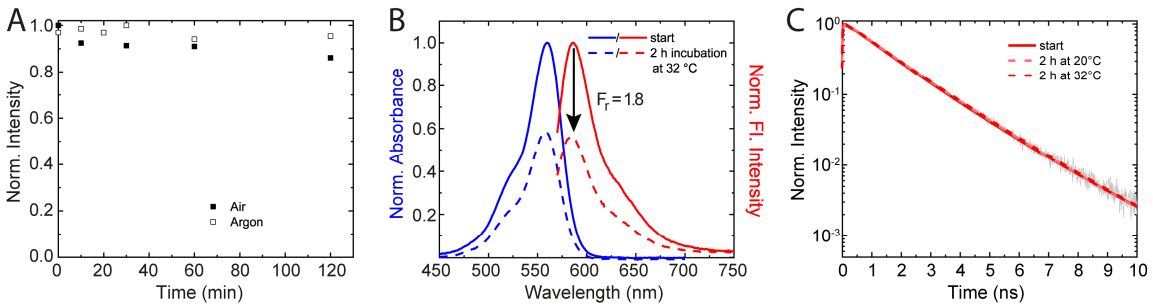

Figure 4-29. Influence of oxygen on DLs photophysical parameters. (A) Decrease of the DL fluorescence intensity in PBS over a time period of 2 h at 20°C under normal atmosphere and under oxygen deprived conditions at 20°C. (B) DL fluorescence emission spectra in PBS showing the reduction under conditions mimicking skin penetration experiments, i.e. DL was pipetted on a glass bottom dish surface covering a similar surface area as in skin incubation for 2 h at 32 °C. The resulting reduction factor in fluorescence and absorption is F_r = 1.8. (C) Fluorescence decay curves of DL before (solid) and after incubation (dashed) for 2 h at 20°C and 32°C. Fluorescence lifetime data in gray, and biexponential fits of the data in red. The fit data are "Start": β_1=0.54, τ_1=1.22 ns; β_2=0.46, τ_2=1.95 ns; $<\tau_{pop}>$=1.56 ns. "2h at 20°C": β_1=0.39, τ_1=1.17 ns; β_2=0.61, τ_2=1.82 ns; $<\tau_{pop}>$=1.56 ns. "2h at 32°C": β_1=0.34, τ_1=1.12 ns; β_2=0.66, τ_2=1.80 ns; $<\tau_{pop}>$=1.57 ns. Here, β_i are the fractional amplitudes, τ_i are the decay components, and $<\tau_{pop}>$ is the mean fluorescence lifetime.

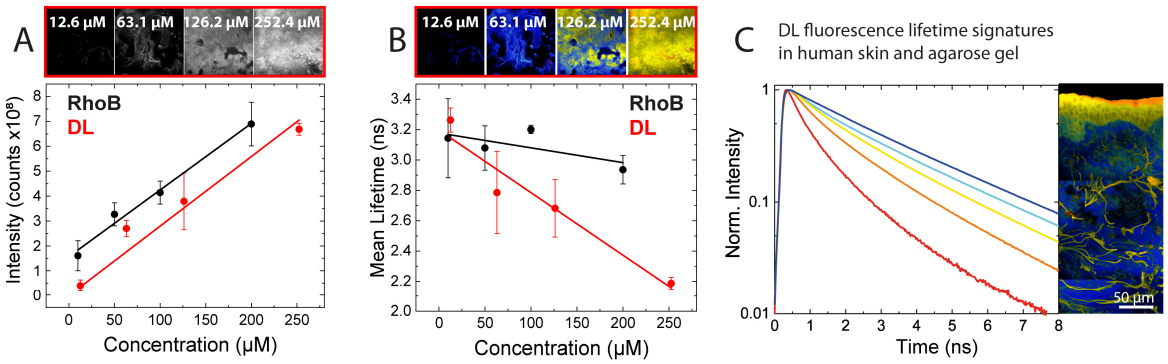

Figure 4-30. Calibration measurements of RhoB and DL in agarose gel. (A) Fluorescence intensity-based calibration, fit parameter for DL: slope=(2.79±0.20) x10^6 cts/µM, intercept=0 cts (B) fluorescence lifetime-based calibration, fit parameter for DL: slope=(-41.2±7.7) x10^{-4} ns/µM, intercept=/3.20±0.11). Exemplary FLIM images of DL in agarose are shown above the respective graph (C) fluorescence decays found in agarose slides of varying DL concentration and in cryosections of human skin. Experimental conditions: λ_{ex} = 530 nm, λ_{em} > 545 nm.

The amplitude of an EPR signal is naturally directly proportional to the number of spins i.e. labeled molecules in the sample and thus serves as an excellent reference for any fluorescence-based quantification. A fluorescent signal on the other hand needs to be calibrated in order to relate signal amplitude to concentration.

For this purpose, agarose gels with defined RhoB and DL concentrations, ranging from 10 to 253 µM were prepared and cryotomed to 7 µm to mimic the actual skin cryosections (Figure 4-30). These

calibration slides were consequently measured in our FLIM setup under the same conditions as the tissue sections. The fluorescence intensity increased linearly with concentration for RhoB and DL (Figure 4-30A). The fluorescence lifetime of RhoB was almost invariant to its concentration; however, the fluorescence lifetime of DL exhibited a faster fluorescence lifetime with increasing DL concentration (Figure 4-30B). Thus, in addition to FLIM-based visualization, we can utilize the DL fluorescence intensity and lifetime as a concentration measure. Both, fluorescence intensity and lifetime were fitted in first approximation as a linear function in dependence of fluorophore concentration. Using the fit parameters from the calibration measurements of DL in agarose gel (Figure 4-30) and using reduction factor F_r gathered from oxidation experiments (Figure 4-29) one can calculate the DL concentration in a skin section after DL penetration from the fluorescence intensity in FLIM images using the following equation:

$$c_{DL}(I) = \frac{I_{ROI} / \#pixel\ in\ ROI \times image\ pixel}{\alpha} * \mathrm{MW} * F_r \qquad (41)$$

Where I_{ROI} is the fluorescence intensity in the region of interest (ROI), such as whole skin, viable epidermis or dermis, MW is the molecular weight and and α and b are slope and intercept of a linear fit of the concentration calibration data (Figure 4-30). FLIM lifetime data were analyzed using our cluster algorithm [152,210], which discriminates images pixels on the basis of discrete lifetime clusters. Hence, the following equation is used to calculate concentration from lifetime data:

$$c_{DL}(\tau) = \sum_{cluster} \frac{\left(\frac{\tau_{cluster} - b}{\alpha}\right) * \#pixel_{cluster}}{total\ \#pixel\ in\ ROI} * MW * F_r \qquad (42)$$

Where $\tau_{cluster}$ is the mean fluorescence lifetime of a given fluorescence cluster. As explained above, I am using a cluster algorithm that sorts all image pixel into discrete lifetime cluster with shared mean fluorescence lifetime to achieve higher contrast and statistical significance while maintaining image resolution.

For tissue measurements, barrier disrupted human skin permeated with DL was used as a model system. Human skin samples were prepared as described in the method section 3.12. Tissue preparation as well as EPR experiments were conducted by Pin Dong of the Meinke working group (Department of Dermatology, Charité Universitätsmedizin Berlin). In EPR, whole tissue blocks were measured. FLIM on the other hand, measured cryo-sections but of the very same skin preparation (Figure 3-8).

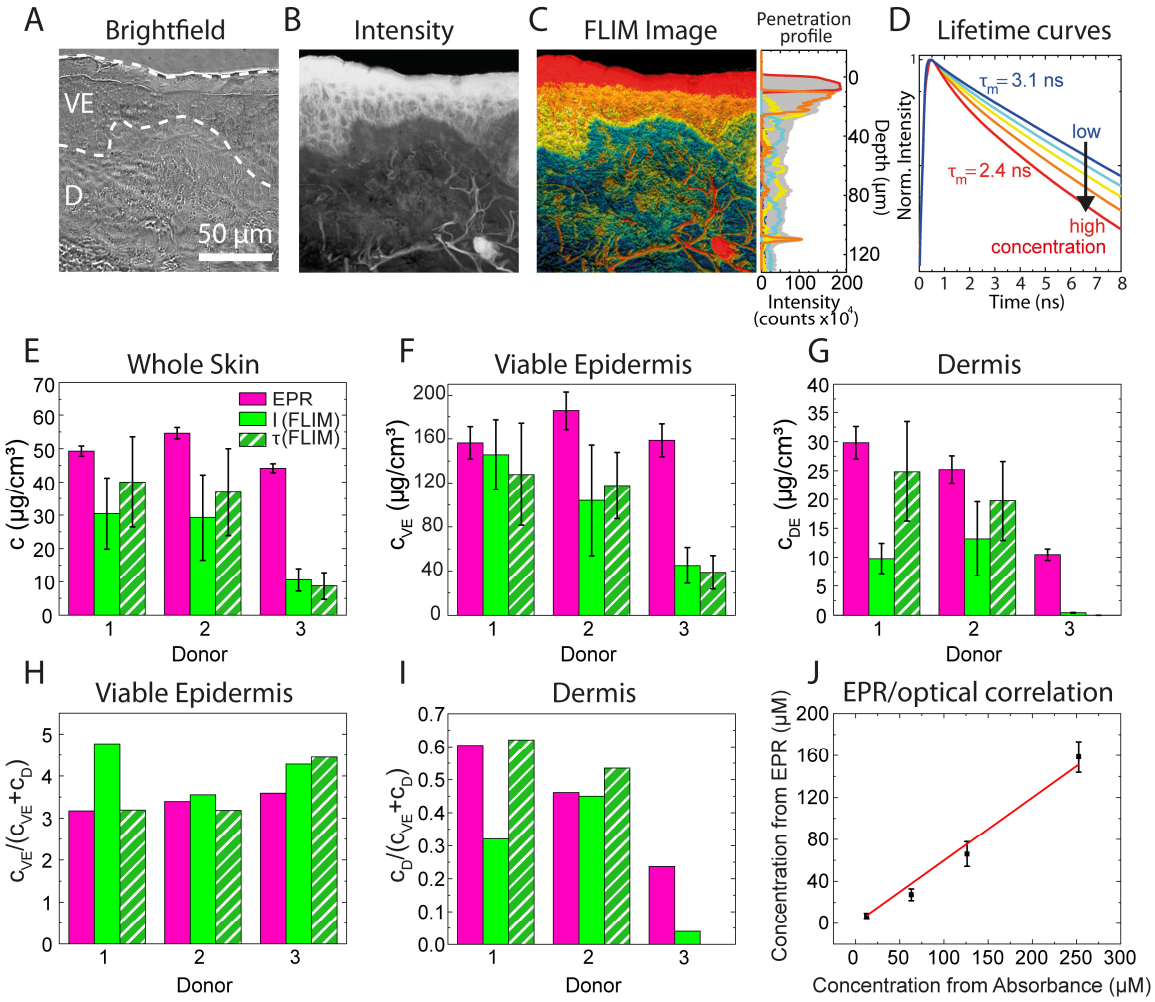

Figure 4-31. Localization and quantifaction of DL in human skin by EPR and FLIM. Brightfield microscopy and FLIM yield a multitude of read-outs from skin sections: (A) histological features, (B) spatially resolved fluorescence intensity and (C,D) fluorescence lifetime information of the DL which independently reports on label concentration used in the quantification (E-I). (E) The absolute concentrations of DL in the whole skin layers containing the viable epidermis and dermis, (F) viable epidermis (G) dermis and (H,I) the respective concentrations which were normalized to the concentration of DL in whole skin (c_D+c_{VE}) of each donor. (J) Relative labelling stoichiometry of PCA and RhoB labels determined to be 60% in DL. Measured by EPR and fluorescence absorption, respectively. Error bars are ± SD (n=3). Experimental conditions: λ_{ex} = 530 nm, λ_{em} > 545 nm. EPR experiments and data analysis was performed by Pin Dong.

For the localization of DL in human skin we used FLIM measurements. The Cluster-FLIM approach enhances the image contrast as well as statistical significance and thereby resolves the diffusion patterns of DL spatially, identifies structures in the skin where DL accumulates (Figure 4-31B,C) and paints a more comprehensive picture of DLs penetration behavior in conjunction with EPR analysis.

As shown in Figure 4-30C and Figure 4-31D, DL exhibits the fastest fluorescence decay (red cluster) in the upper layers of the VE and filament like structures in the D, presumably collagen and elastin fibers. Intermediate decay times are found in the lower epidermis whereas the slowest decays are observed in most of the tissue in the dermis (blue cluster). The absolute concentrations of DL in the VE and DE (c_{VE} and c_D) were quantified by EPR and FLIM (Figure 4-31E-G). Both fluorescence-based methods are in good agreement for each donor in whole skin.

Note that we found the concentration of the nitroxide spins measured by EPR account for about 60% of the concentration calculated from the optical density in absorption spectra of the same DL solution (Figure 4-31J). Based on this finding, I corrected the concentration determined by EPR accordingly. EPR and fluorescence approaches yielded consistent DL concentrations within 2σ in skin, except for donor #3. At lower DL concentrations within the dermis (Figure 4-31H), the fluorescence lifetime-based concentration determination agrees nicely with the EPR quantification. I also calculated a normalized concentration in VE and D (c_{VE} and c_D over c_{VE+D}) in order to compare the relative distribution DL in different skin layers, i.e., VE and D (Figure 4-31H,I). Here, the data reveal very good agreement between EPR and FLIM in the viable epidermis for all three donors (Figure 4-31H).

The apparent heterogeneous inter-donor penetration behavior of donor #3 may be due to the fact that sample penetration heterogeneities would be more pronounced in cryosections, as used for FLIM, than in the integral concentration determination in EPR (Figure 3-8). Also, distinct morphological features such as skin furrows and hair follicles are potential accumulation sites of DL but were not included in the cryosections for FLIM so far. Figure 4-32A shows a hair follicle after incubation with DL for 2h. The follicular and transfollicular penetration was significantly (18-fold higher concentration compared to surrounding tissue) for the barrier disrupted skin used in this work. In contrast to the FLIM measurements on cryosections, the EPR measurements on tissue blocks include DL molecules trapped in the hair follicles and its surroundings. However, even if considerably higher DL can be found in hair follicles, they only contribute to 1-14% of the skin surface[194], such that DL penetration would be increased by only about 5%. Thus, everything considered, our quantitative results of DL skin penetration were consistent between EPR and FLIM.

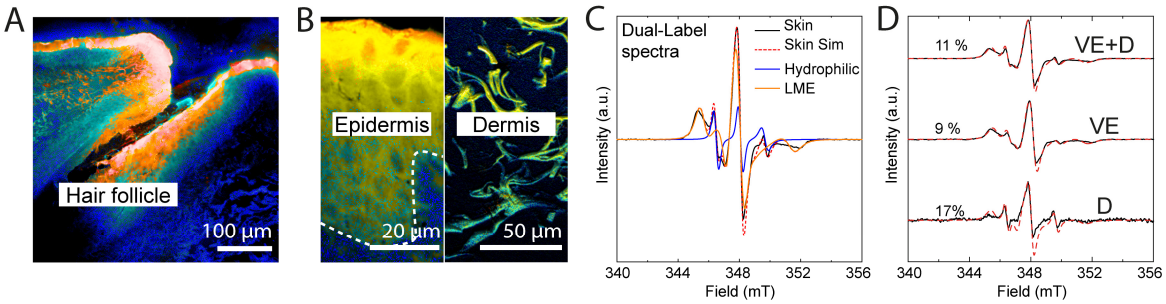

Figure 4-32. Sites of DL accumulation in (A) hair follicle (B) the viable epidermis and the dermis shown by FLIM. (C) EPR spectrum of DL in whole skin is a linear combination of pure spectra of DL in a hydrophilic, fast mobility (DL_{Hydro}) or less polar, low mobility environment (LME). (D) The experimental and simulated EPR spectra of DL in the viable epidermis (VE) and dermis (D). All spectra were normalized to their own highest peak intensity. The solid lines are experimental spectra and the dotted lines are simulated spectra. The fractions of DL_{Hydro} in different skin layers are denoted in (D). EPR experiments and data analysis was performed by Pin Dong.

With high lateral resolution, FLIM is able to characterize the localizations of DL at subcellular level. As presented in Figure 4-32B, in the upper region of the VE, DL distributed in the cytoplasm of keratinocytes and intercellular space. In the dermis, collagens and elastins exhibit a notably strong DL signal, while it wasn't found in local skin cells, i.e. fibroblasts, macrophages, etc. (Figure 4-32B). Simulating superpositions of EPR spectra revealed the presence of two distinct microenvironments for the DL (Figure 4-32C). The first representing DL with low mobility in a slightly apolar microenvironment, compatible to a restricted microenvironment with lipids, hydrophobic proteins, or less water content. The other, presents DL with much higher mobility, indicating a hydrophilic microenvironment (DL_{Hydro}). DL_{Hydro} was found (9 ± 3) % in the VE, and it increased to 17% in the D (Figure 4-32D). Due to low signal in the D, the sum of all collected spectra of DL in the D was used in the simulation, hence only one value was generated without standard deviation. Nevertheless, the result reveals a higher fraction of DL_{Hydro} in the D compared to the viable epidermis because of higher water content in the D. (11 ± 3) % was the mean fraction of DL_{Hydro} in the skin sample containing the VE and D.

The combination of FLIM and EPR is a valuable strategy to realize quantitative study of skin penetration and visualization of spatial distribution of drugs. Yet, previous studies have labeled the drug of interest by exclusively either fluorophore or spin for studying the skin penetration[157,238]. Different labeling probably changes the physiochemical properties of the drug and consequently the skin penetration could vary, making it hard to compare FLIM and EPR results[233,239]. Thus, to incorporate two labels into one compound is prerequisite for investigating the same drug by FLIM and EPR. This work has established a synthesis platform which covalently binds RhoB and PCA to the linker of Fmoc-Lys(Boc) via amide bonds. Importantly, the tert-butanol ester bond in the DL

provides the third labeling position which offers the possibility in future studies to attach the DL to a variety of drugs, such as dexamethasone, etanercept and tacrolimus. Consequently, the cutaneous penetration of these dual-labeled drugs can be detected by label-free and label-based techniques together to investigate the drug release kinetics from carriers and penetration mechanisms[240,241]. The choice of label in these studies proves to be critical since, as mentioned above, fluorescein is quenched by PCA and RhoB gradually degrades in the presence of oxygen. Also, in the latest iteration, the fraction of active nitroxide label is only about 60%.

The quantitative results of skin penetration obtained by FLIM are in a good agreement with EPR results, except that EPR found significantly more DL in the VE and D of the third donor. The skin of this donor had obviously more hairs than the other two donors.

FLIM images illustrate that DL mainly accumulated in the intercellular space of the VE and collagens of the DE, while EPR simulations show that a major part of DL in the VE and D was in a relative hydrophobic microenvironment though a LogP of 0.07 suggests an equiportional partition in hydrophilic and hydrophobic regimes. These DL might bind to the cell membrane and proteins in the intercellular space of the VE and the hydrophobic domains of collagen[242,243]. The lower fraction of DL in a hydrophilic microenvironment of the VE reflected in the EPR result can be explained by the distribution of DL in the cytoplasm of the keratinocytes. The EPR results can provide not only the absolute amount of DL in skin but also fractions of DL located in different microenvironments. If these microenvironments can be clearly assigned to the spatial distribution of DL in the FLIM images, then the quantification of DL on a subcellular level is possible.

5 Summary

In this work, I employed state-of-the-art time-resolved fluorescence spectroscopic and microscopic techniques to investigate biomolecular interactions on the subcellular to tissue level. With the help of newly developed analysis methods, this enabled me to characterize innovative nanoparticle assisted drug delivery systems as well as the biological barriers they seek to overcome with direct implications for future drug development and medical application. We used fluorescent molecular rotor dyes to determine membrane viscosity and lipid phase transitions in artificial vesicle systems and even living cells, and then went on to spatially resolve viscosity profiles of the mucus layer on epithelial cells of the intestine and could even connect changes in mucus viscosity to bacterial challenge in the murine GI tract. We generated background free penetration profiles with the help of Cluster-FLIM, which allowed for a computer-based prediction model for time-dependent Nile Red concentration in different skin layers or evaluate drug-cell interaction of the fluorescently labeled anti-cancer drug cetuximab in 3D tissue models. Finally, we developed a platform for dual-labeled drugs to simultaneously capitalize on the complementary read-outs from EPR and FLIM to unravel penetration pathways in skin and pinpoint drug accumulation sites.

For the investigation of membrane viscosity and lipid phase transition, we used the fluorescent molecular rotor ICC coupled to a dendritic polyglycerol nanoparticle (dPGS). Using this construct, I could determine the positioning of the ICC within the lipid bilayer using spin labeled lipids and the induced fluorescence quenching of ICC by the presence of the unpaired electron. The ICC label was incorporated 3 Å below the polar headgroups, thus reporting on the local nanoviscosity of the upper lipid tail region. We went on and demonstrated dPGS-ICCs capabilities in detecting lipid composition and membrane fluidity in DMPC MLV and reliably detect the lipid phase transition. I finally determined membrane nanoviscosity in live HeLa cells and found intracellular vesicles characterized by higher viscosity (404 mPa s) than the outer cell membrane (187 mPa s) both of which values are in agreement with the literature[169,170].

To expand on the capability of ICC to report on viscosity, I used ICC conjugated to wheat germ agglutinin (WGA) to compile the viscosity distribution of mucus *in vitro* and *in vivo* with high spatial resolution. WGA binds to the o-glycans of mucins and thus ensures the detection of local nanoviscosity directly associated with the mucin network. Calibration curves of WGA-ICC in aqueous sucrose and various polymer solutions have been established to assess the contribution of protein backbone, inter mesh solvent and secondary crowding agents to the overall nano- and bulk viscosity found in mucus. The extensive dissection of these calibration curves in combination with the global analysis of a series of Cluster-FLIM images facilitated the compilation of viscosity

profiles of the apical mucus layer found on live HT29-mtx cells, an immortalized epithelial cell line reproducing the phenotype of goblet cells found in the small intestine. I could determine not only the viscosity gradient and thickness of the mucus layer but also detect heterogeneities of high viscosity zones in the otherwise low viscosity regime far from the cell surface which were impossible to detect with other techniques and, hence, have not been reported before. Finally, I investigated the mucus viscosity in the murine small intestine and could find an increase in viscosity after antibiotic treatment suggesting the missing cleavage of mucin multimers due to bacterial challenge. Following from these results, I hope I could demonstrate conclusively the value of fluorescent molecular rotors for the characterization of membrane systems and the mucus layer in detail but also for the establishment of a holistic understanding of biological barriers in general.

In order to evaluate penetration pathways and quantify the benefit of nanoparticle assisted drug delivery of lipophilic drugs in the skin, we used the capability of Cluster-FLIM to generate background free penetration profiles. Based on these profiles, numerical modelling simulated the free energy and diffusivity profile for NR in the skin. The unambiguous dissection of the free energy landscape and diffusivity gradients of NR and the comparison to the penetration enhancement achieved by the pH sensitive nanoparticle Eudragit® provided new insight into physicochemical parameters which determine cutaneous and transcutaneous drug delivery. The SC was identified as a sink for lipophilic molecules in the skin. The dermis, on the other hand, appears to be essentially water like, which creates a free energy barrier and prevents the deeper penetration of lipophilic molecules like NR. The nanoparticle assisted uptake led to an 8 times faster uptake into the epidermis, presumably by reducing the SC-VE barrier. Additionally, we could show the effective deep penetration of the nanoparticles in hair follicles and subsequent lateral diffusion, leading to higher bioavailability in the dermis, corresponding to a better therapeutic effect of the delivered drug.

For the simultaneous visualization and quantification of molecules of interest in tissue, we developed a platform for dual-labeled compounds. Using a highly fluorescent dye and a spin probe, conjugated by a tri-functional linker which also enables the coupling to a biomolecule of choice, we provide the means for multiplexing FLIM and EPR spectroscopy. In addition, the conjugation of the dye Rhodamine B to the dual label rendered its fluorescence lifetime concentration dependent. Using calibration measurements in model tissue, this enabled us to compare three independent assessments of label concentration in penetration experiments in human skin. After correcting for labeling stoichiometry and stability, we found consistent values between EPR and fluorescence based concentration determination in different skin layers and especially well matching results within the fluorescence lifetime based and fluorescence intensity based methods. In addition, FLIM

could spatially resolve the accumulation sites of the dual label and identified the intercellular matrix followed by the cytoplasm as regions of highest dual label concentration in the viable epidermis. In the dermis, the dual label was almost exclusively found in the collagen/elastin fibers. EPR contributed by finding most of the dual label in a slightly apolar and highly restricted microenvironment in the viable epidermis with an increasing contribution of a hydrophilic and more mobile phase in the dermis. In this study, we provided plenty of precedence for the versatile combination of FLIM and EPR measurements. In the future, numerous further applications are imaginable. The EPR probe could act as a sensor for reactive oxygen species[244] while FLIM provides the simultaneous spatial resolution within the cellular environment[245]. Also, the use of photosensitizers in photodynamic therapy would be imaginable[246]. Thus, I hope to contribute with these results to novel future study designs which will yield valuable insight into biomolecular interactions, structure, and dynamics using the complementary data from FLIM and EPR.

Publications

The following publications resulted from this thesis:

A Dual Fluorescence-Spin Label Probe for Visualization and Quantification of Target Molecules in Tissue by Multiplexed FLIM – EPR Spectroscopy
Pin Dong, Johannes Stellmacher, Lydia M. Bouchet, Marius Nieke, Amit Kumar, Ernesto R. Osorio-Blanco, Gregor Nagel, Silke B. Lohan, Alexa Patzelt, Monika Schäfer-Korting, Marcelo Calderón, Martina Meinke, Ulrike Alexiev
Angew. Chem. Int. Ed.. Accepted Author Manuscript. https://doi.org/10.1002/anie.202012852

A multilayered epithelial mucosa model of head neck squamous cell carcinoma for analysis of tumor-microenvironment interactions and drug development
Leonie Gronbach, Christopher Wolff, Konrad Klinghammer, Johannes Stellmacher, Philipp Jurmeister, Ulrike Alexiev, Monika Schäfer-Korting, Ingeborg Tinhofer, Ulrich Keilholz, Christian Zoschke
Biomaterials. 2020; 258: 120277

Faster, sharper, more precise: Automated Cluster-FLIM in preclinical testing directly identifies the intracellular fate of theranostics in live cells and tissue
Robert Brodwolf, Pierre Volz-Rakebrand, Johannes Stellmacher, Christopher Wolff, Michael Unbehauen, Rainer Haag, Monika Schäfer-Korting, Christian Zoschke, Ulrike Alexiev
Theranostics. 2020; 10(14): 6322–6336

The redox-coupled proton-channel opening in cytochrome c oxidase
Alexander Wolf, Jovan Dragelj, Juliane Wonneberg, Johannes Stellmacher, Jens Balke, Anna Lena Woelke, Milan Hodoscek, Ernst Walter Knapp, Ulrike Alexiev
Chem. Sci. 2020; 11: 3804-3811

Transient Deprotonation of the Chromophore Affects Protein Dynamics Proximal and Distal to the Linear Tetrapyrrole Chromophore in Phytochrome Cph1
Maryam Sadeghi, Jens Balke, Constantin Schneider, Soshichiro Nagano, Johannes Stellmacher, Günter Lochnit, Christina Lang, Chris Weise, Jon Hughes, Ulrike Alexiev
Biochemistry. 2020; 59(9): 1051-1062

Expanding the Scope of Reporting Nanoparticles: Sensing of Lipid Phase Transitions and Nanoviscosities in Lipid Membranes
Katja Ober, Pierre Volz-Rakebrand, Johannes Stellmacher, Robert Brodwolf, Kai Licha, Rainer Haag, Ulrike Alexiev
Langmuir. 2019; 35: 11422-11434

Pitfalls in using fluorescence tagging of nanomaterials: tecto-dendrimers in skin tissue as investigated by Cluster-FLIM
Pierre Volz, Priscila Schilrreff, Robert Brodwolf, Christopher Wolff, Johannes Stellmacher, Jens Balke, Maria J. Morilla, Christian Zoschke, Monika Schäfer-Korting, Ulrike Alexiev
Ann. N. Y. Acad. Sci. 2017; 1405: 202-214

Under revision:

Assessment of Nanoparticle-enhanced Drug Delivery across Barriers by Cluster-FLIM and Data-based Modeling: Hair Follicles as Target Structures
Johannes Stellmacher, Pierre Volz-Rakebrand, Robert Brodwolf, Amanuel Wolde-Kidan, Robert Schulz, Silke Lohan, Martina Meinke, Jürgen Lademann, Fitsum Feleke Sahle, Roland Bodmeier, Sabrina Hadam, Annika Vogt, Roland R. Netz, Ulrike Alexiev
Submitted to: Journal of Investigative Dermatology

References

1 Wong, C. H., Siah, K. W. & Lo, A. W. Estimation of clinical trial success rates and related parameters. *Biostatistics* **20**, 273-286, doi:10.1093/biostatistics/kxx069 (2019).

2 Khozin, S., Jarow, J. P., Pazdur, R. & Liu, K. Why do oncology drugs fail to gain US regulatory approval? *Nature Reviews Drug Discovery* **14**, 450-U157, doi:10.1038/nrd4651 (2015).

3 Blanco, E., Shen, H. & Ferrari, M. Principles of nanoparticle design for overcoming biological barriers to drug delivery. *Nature Biotechnology* **33**, 941-951, doi:10.1038/nbt.3330 (2015).

4 Lieleg, O. & Ribbeck, K. Biological hydrogels as selective diffusion barriers. *Trends in Cell Biology* **21**, 543-551, doi:10.1016/j.tcb.2011.06.002 (2011).

5 Cevc, G. & Vierl, U. Nanotechnology and the transdermal route: A state of the art review and critical appraisal. *J Control Release* **141**, 277-299, doi:10.1016/j.jconrel.2009.10.016 (2010).

6 Sok, M., Sentjurc, M., Schara, M., Stare, J. & Rott, T. Cell membrane fluidity and prognosis of lung cancer. *Ann Thorac Surg* **73**, 1567-1571, doi:10.1016/s0003-4975(02)03458-6 (2002).

7 Kaur, J. & Sanyal, S. N. Alterations in membrane fluidity and dynamics in experimental colon cancer and its chemoprevention by diclofenac. *Mol Cell Biochem* **341**, 99-108, doi:10.1007/s11010-010-0441-6 (2010).

8 Goldstein, D. B. The effects of drugs on membrane fluidity. *Annu Rev Pharmacol Toxicol* **24**, 43-64, doi:10.1146/annurev.pa.24.040184.000355 (1984).

9 Liu, P., Duan, W., Wang, Q. & Li, X. The damage of outer membrane of Escherichia coli in the presence of TiO2 combined with UV light. *Colloids Surf B Biointerfaces* **78**, 171-176, doi:10.1016/j.colsurfb.2010.02.024 (2010).

10 Prates Ramalho, J. P., Gkeka, P. & Sarkisov, L. Structure and phase transformations of DPPC lipid bilayers in the presence of nanoparticles: insights from coarse-grained molecular dynamics simulations. *Langmuir* **27**, 3723-3730, doi:10.1021/la200236d (2011).

11 Bothun, G. D. Hydrophobic silver nanoparticles trapped in lipid bilayers: Size distribution, bilayer phase behavior, and optical properties. *J Nanobiotechnology* **6**, 13, doi:10.1186/1477-3155-6-13 (2008).

12 Park, S. H., Oh, S. G., Mun, J. Y. & Han, S. S. Effects of silver nanoparticles on the fluidity of bilayer in phospholipid liposome. *Colloids Surf B Biointerfaces* **44**, 117-122, doi:10.1016/j.colsurfb.2005.06.002 (2005).

13 Lai, S. K., Wang, Y. Y., Wirtz, D. & Hanes, J. Micro- and macrorheology of mucus. *Adv Drug Deliver Rev* **61**, 86-100, doi:10.1016/j.addr.2008.09.012 (2009).

14 Berezin, M. Y. & Achilefu, S. Fluorescence lifetime measurements and biological imaging. *Chem Rev* **110**, 2641-2684, doi:10.1021/cr900343z (2010).

15 Alexiev, U., Volz, P., Boreham, A. & Brodwolf, R. Time-resolved fluorescence microscopy (FLIM) as an analytical tool in skin nanomedicine. *Eur. J. Pharm. Biopharm.* **116**, 111-124, doi:10.1016/j.ejpb.2017.01.005 (2017).

16 Boreham, A. *et al.* Detecting and Quantifying Biomolecular Interactions of a Dendritic Polyglycerol Sulfate Nanoparticle Using Fluorescence Lifetime Measurements. *Molecules* **21**, E22, doi:10.3390/molecules21010022 (2015).

17 Richter, C. *et al.* Dual-fluorescence pH probe for bio-labelling. *Phys Chem Chem Phys* **17**, 30590-30597, doi:10.1039/c5cp05454k (2015).

18 Balke, J. *et al.* Visualizing Oxidative Cellular Stress Induced by Nanoparticles in the Subcytotoxic Range Using Fluorescence Lifetime Imaging. *Small* **14**, e1800310, doi:10.1002/smll.201800310 (2018).

19 Kirchberg, K. *et al.* Conformational dynamics of helix 8 in the GPCR rhodopsin controls arrestin activation in the desensitization process. *Proc Natl Acad Sci U S A* **108**, 18690-18695, doi:10.1073/pnas.1015461108 (2011).

20 Ober, K. *et al.* Expanding the Scope of Reporting Nanoparticles: Sensing of Lipid Phase Transitions and Nanoviscosities in Lipid Membranes. *Langmuir* **35**, 11422-11434, doi:10.1021/acs.langmuir.9b01372 (2019).
21 Borst, J. W. & Visser, A. J. W. G. Fluorescence lifetime imaging microscopy in life sciences. *Meas. Sci. Technol.* **21**, 102002-102024, doi:10.1088/0957-0233/21/10/102002 (2010).
22 Hirvonen, L. M. *et al.* Lightsheet fluorescence lifetime imaging microscopy with wide-field time-correlated single photon counting. *J Biophotonics*, e201960099, doi:10.1002/jbio.201960099 (2019).
23 Witting, M. *et al.* Interactions of hyaluronic Acid with the skin and implications for the dermal delivery of biomacromolecules. *Mol Pharm* **12**, 1391-1401, doi:10.1021/mp500676e (2015).
24 Gaus, K., Zech, T. & Harder, T. Visualizing membrane microdomains by Laurdan 2-photon microscopy (Review). *Molecular Membrane Biology* **23**, 41-48, doi:10.1080/09687860500466857 (2006).
25 Budin, I. *et al.* Viscous control of cellular respiration by membrane lipid composition. *Science* **362**, 1186-1189, doi:10.1126/science.aat7925 (2018).
26 Chiantia, S., Ries, J., Kahya, N. & Schwille, P. Combined AFM and two-focus SFCS study of raft-exhibiting model membranes. *Chemphyschem* **7**, 2409-2418, doi:10.1002/cphc.200600464 (2006).
27 Saeidpour, S. *et al.* Localization of dexamethasone within dendritic core-multishell (CMS) nanoparticles and skin penetration properties studied by multi-frequency electron paramagnetic resonance (EPR) spectroscopy. *Eur J Pharm Biopharm* **116**, 94-101, doi:10.1016/j.ejpb.2016.10.001 (2017).
28 Saeidpour, S. *et al.* Drug distribution in nanostructured lipid particles. *Eur J Pharm Biopharm* **110**, 19-23, doi:10.1016/j.ejpb.2016.10.008 (2017).
29 Becker, W. *Advanced time-correlated single photon counting applications*. Vol. 111 (Springer, 2015).
30 Parker, C. A. *Photoluminescence of Solutions: with applications to photochemistry and analytical chemistry*. pp. 71-82 (Elsevier Publishing Company, 1968).
31 Birks, J. B. *Aromatic Molecules*. Vol. 704 pp. 433-447 (Wiley, New York, 1970).
32 Stern, O. & Volmer, M. Volmer "Über die abklingungszeit der fluoreszenz. *Physics Z* **20**, 183 (1919).
33 Kuimova, M. K., Yahioglu, G., Levitt, J. A. & Suhling, K. Molecular rotor measures viscosity of live cells via fluorescence lifetime imaging. *J Am Chem Soc* **130**, 6672-6673, doi:10.1021/ja800570d (2008).
34 Wu, Y. *et al.* Molecular rheometry: direct determination of viscosity in Lo and Ld lipid phases via fluorescence lifetime imaging. *Phys Chem Chem Phys* **15**, 14986-14993, doi:10.1039/c3cp51953h (2013).
35 Vysniauskas, A. *et al.* Exploring viscosity, polarity and temperature sensitivity of BODIPY-based molecular rotors. *Phys Chem Chem Phys* **19**, 25252-25259, doi:10.1039/c7cp03571c (2017).
36 Swindells, J. F., Snyder, C. F., Hardy, R. C. & Golden, P. E. Viscosities of sucrose solutions at various temperatures: Tables of recalculated values. *Supplement to National Bureau of Standards Circular* **440** (1958).
37 Rashid, R., Chee, S. M., Raghunath, M. & Wohland, T. Macromolecular crowding gives rise to microviscosity, anomalous diffusion and accelerated actin polymerization. *Phys Biol* **12**, 034001, doi:10.1088/1478-3975/12/3/034001 (2015).
38 Förster, T. & Hoffmann, G. Die viskositätsabhängigkeit der fluoreszenzquantenausbeuten einiger farbstoffsysteme. *Zeitschrift für Physikalische Chemie* **75**, 63-76 (1971).
39 Green, J. A., Singer, L. A. & Parks, J. H. Fluorescence quenching by the stable free radical di-t-butylnitroxide. *The Journal of Chemical Physics* **58**, 2690-2695 (1973).

40 London, E. Investigation of membrane structure using fluorescence quenching by spin-labels. *Molecular and cellular biochemistry* **45**, 181-188 (1982).
41 Lin, F. *et al.* Electron transfer quenching by nitroxide radicals of the fluorescence of carbon dots. *Journal of Materials Chemistry* **22**, 11801-11807 (2012).
42 Jost, P., Waggoner, A. & Griffith, O. Structure and function of biological membranes. *Academic Press, New York, NY*, pp. 83-144 (1971).
43 Chattopadhyay, A. & London, E. Parallax method for direct measurement of membrane penetration depth utilizing fluorescence quenching by spin-labeled phospholipids. *Biochemistry* **26**, 39-45, doi:10.1021/bi00375a006 (1987).
44 Tristram-Nagle, S., Liu, Y., Legleiter, J. & Nagle, J. F. Structure of gel phase DMPC determined by X-ray diffraction. *Biophys J* **83**, 3324-3335, doi:10.1016/S0006-3495(02)75333-2 (2002).
45 Bevins, C. L. & Salzman, N. H. Paneth cells, antimicrobial peptides and maintenance of intestinal homeostasis. *Nat Rev Microbiol* **9**, 356-368, doi:10.1038/nrmicro2546 (2011).
46 Ambort, D. *et al.* Calcium and pH-dependent packing and release of the gel-forming MUC2 mucin. *Proc Natl Acad Sci U S A* **109**, 5645-5650, doi:10.1073/pnas.1120269109 (2012).
47 Shogren, R., Gerken, T. A. & Jentoft, N. Role of glycosylation on the conformation and chain dimensions of O-linked glycoproteins: light-scattering studies of ovine submaxillary mucin. *Biochemistry* **28**, 5525-5536, doi:10.1021/bi00439a029 (1989).
48 Corfield, A. P. Mucins: a biologically relevant glycan barrier in mucosal protection. *Biochim Biophys Acta* **1850**, 236-252, doi:10.1016/j.bbagen.2014.05.003 (2015).
49 Hattrup, C. L. & Gendler, S. J. Structure and function of the cell surface (tethered) mucins. *Annu Rev Physiol* **70**, 431-457, doi:10.1146/annurev.physiol.70.113006.100659 (2008).
50 Gum, J. R., Jr., Crawley, S. C., Hicks, J. W., Szymkowski, D. E. & Kim, Y. S. MUC17, a novel membrane-tethered mucin. *Biochem Biophys Res Commun* **291**, 466-475, doi:10.1006/bbrc.2002.6475 (2002).
51 Williams, S. J. *et al.* Two novel mucin genes down-regulated in colorectal cancer identified by differential display. *Cancer Res* **59**, 4083-4089 (1999).
52 Linden, S. K., Florin, T. H. & McGuckin, M. A. Mucin dynamics in intestinal bacterial infection. *PLoS One* **3**, e3952, doi:10.1371/journal.pone.0003952 (2008).
53 Shibahara, H. *et al.* Pathobiological implications of mucin (MUC) expression in the outcome of small bowel cancer. *PLoS One* **9**, e86111, doi:10.1371/journal.pone.0086111 (2014).
54 Audie, J. P. *et al.* Expression of human mucin genes in respiratory, digestive, and reproductive tracts ascertained by in situ hybridization. *J Histochem Cytochem* **41**, 1479-1485, doi:10.1177/41.10.8245407 (1993).
55 Larsson, J. M. *et al.* Altered O-glycosylation profile of MUC2 mucin occurs in active ulcerative colitis and is associated with increased inflammation. *Inflamm Bowel Dis* **17**, 2299-2307, doi:10.1002/ibd.21625 (2011).
56 Hasnain, S. Z., Gallagher, A. L., Grencis, R. K. & Thornton, D. J. A new role for mucins in immunity: insights from gastrointestinal nematode infection. *Int J Biochem Cell Biol* **45**, 364-374, doi:10.1016/j.biocel.2012.10.011 (2013).
57 Ridley, C. *et al.* Assembly of the respiratory mucin MUC5B: a new model for a gel-forming mucin. *J Biol Chem* **289**, 16409-16420, doi:10.1074/jbc.M114.566679 (2014).
58 Schutte, A. *et al.* Microbial-induced meprin beta cleavage in MUC2 mucin and a functional CFTR channel are required to release anchored small intestinal mucus. *Proc Natl Acad Sci U S A* **111**, 12396-12401, doi:10.1073/pnas.1407597111 (2014).
59 Specian, R. D. & Neutra, M. R. Mechanism of rapid mucus secretion in goblet cells stimulated by acetylcholine. *J Cell Biol* **85**, 626-640, doi:10.1083/jcb.85.3.626 (1980).
60 Wlodarska, M. *et al.* NLRP6 inflammasome orchestrates the colonic host-microbial interface by regulating goblet cell mucus secretion. *Cell* **156**, 1045-1059, doi:10.1016/j.cell.2014.01.026 (2014).
61 Ermund, A., Schutte, A., Johansson, M. E., Gustafsson, J. K. & Hansson, G. C. Studies of mucus in mouse stomach, small intestine, and colon. I. Gastrointestinal mucus layers have

different properties depending on location as well as over the Peyer's patches. *Am J Physiol Gastrointest Liver Physiol* **305**, G341-347, doi:10.1152/ajpgi.00046.2013 (2013).

62 Johansson, M. E. *et al.* The inner of the two Muc2 mucin-dependent mucus layers in colon is devoid of bacteria. *Proc Natl Acad Sci U S A* **105**, 15064-15069, doi:10.1073/pnas.0803124105 (2008).

63 Johansson, M. E. Fast renewal of the distal colonic mucus layers by the surface goblet cells as measured by in vivo labeling of mucin glycoproteins. *PLoS One* **7**, e41009, doi:10.1371/journal.pone.0041009 (2012).

64 van der Waaij, L. A. *et al.* Bacterial population analysis of human colon and terminal ileum biopsies with 16S rRNA-based fluorescent probes: commensal bacteria live in suspension and have no direct contact with epithelial cells. *Inflamm Bowel Dis* **11**, 865-871, doi:10.1097/01.mib.0000179212.80778.d3 (2005).

65 Lai, S. K., Wang, Y. Y., Wirtz, D. & Hanes, J. Micro- and macrorheology of mucus. *Adv Drug Deliv Rev* **61**, 86-100, doi:10.1016/j.addr.2008.09.012 (2009).

66 Carlstedt, I. & Sheehan, J. K. Structure and macromolecular properties of cervical mucus glycoproteins. *Symp Soc Exp Biol* **43**, 289-316 (1989).

67 Thornton, D. J. & Sheehan, J. K. From mucins to mucus: toward a more coherent understanding of this essential barrier. *Proc Am Thorac Soc* **1**, 54-61, doi:10.1513/pats.2306016 (2004).

68 Engel, E., Guth, P. H., Nishizaki, Y. & Kaunitz, J. D. Barrier function of the gastric mucus gel. *Am J Physiol* **269**, G994-999, doi:10.1152/ajpgi.1995.269.6.G994 (1995).

69 Samet, J. M. & Cheng, P. W. The role of airway mucus in pulmonary toxicology. *Environ Health Perspect* **102 Suppl 2**, 89-103, doi:10.1289/ehp.9410289 (1994).

70 Quraishi, M. S., Jones, N. S. & Mason, J. The rheology of nasal mucus: a review. *Clin Otolaryngol Allied Sci* **23**, 403-413, doi:10.1046/j.1365-2273.1998.00172.x (1998).

71 Matthews, L. W., Spector, S., Lemm, J. & Potter, J. L. Studies on Pulmonary Secretions. I. The over-All Chemical Composition of Pulmonary Secretions from Patients with Cystic Fibrosis, Bronchiectasis, and Laryngectomy. *Am Rev Respir Dis* **88**, 199-204, doi:10.1164/arrd.1963.88.2.199 (1963).

72 Mrsny, R. J. *et al.* Distribution of DNA and alginate in purulent cystic fibrosis sputum: implications to pulmonary targeting strategies. *J Drug Target* **4**, 233-243, doi:10.3109/10611869608995625 (1996).

73 Dawson, M., Wirtz, D. & Hanes, J. Enhanced viscoelasticity of human cystic fibrotic sputum correlates with increasing microheterogeneity in particle transport. *J Biol Chem* **278**, 50393-50401, doi:10.1074/jbc.M309026200 (2003).

74 Wolf, D. P., Blasco, L., Khan, M. A. & Litt, M. Human cervical mucus. I. Rheologic characteristics. *Fertil Steril* **28**, 41-46 (1977).

75 Cone, R. A. in *Mucosal Immunology (Third Edition)* (eds Jiri Mestecky *et al.*) 49-72 (Academic Press, 2005).

76 Meyer, F. A. & Silberberg, A. The rheology and molecular organization of epithelial mucus. *Biorheology* **17**, 163-168, doi:10.3233/bir-1980-171-217 (1980).

77 Carlstedt, I. & Sheehan, J. K. Macromolecular properties and polymeric structure of mucus glycoproteins. *Ciba Found Symp* **109**, 157-172, doi:10.1002/9780470720905.ch11 (1984).

78 Girod, S., Zahm, J. M., Plotkowski, C., Beck, G. & Puchelle, E. Role of the physiochemical properties of mucus in the protection of the respiratory epithelium. *Eur Respir J* **5**, 477-487 (1992).

79 Olmsted, S. S. *et al.* Diffusion of macromolecules and virus-like particles in human cervical mucus. *Biophys J* **81**, 1930-1937, doi:10.1016/S0006-3495(01)75844-4 (2001).

80 Sanders, N. N., De Smedt, S. C. & Demeester, J. The physical properties of biogels and their permeability for macromolecular drugs and colloidal drug carriers. *Journal of pharmaceutical sciences* **89**, 835-849 (2000).

81 Lai, S. K. *et al.* Rapid transport of large polymeric nanoparticles in fresh undiluted human mucus. *Proc Natl Acad Sci U S A* **104**, 1482-1487, doi:10.1073/pnas.0608611104 (2007).
82 Tippe, A., Korbel, R., Ziesenis, A. & Heyder, J. Viscoelastic properties of canine tracheal mucus: effects of structural inhomogeneities and storage. *Scand J Clin Lab Invest* **58**, 259-264, doi:10.1080/00365519850186652 (1998).
83 Tomkiewicz, R. P. *et al.* Species differences in the physical and transport properties of airway secretions. *Can J Physiol Pharmacol* **73**, 165-171, doi:10.1139/y95-025 (1995).
84 Bell, A. E., Allen, A., Morris, E. R. & Ross-Murphy, S. B. Functional interactions of gastric mucus glycoprotein. *International Journal of Biological Macromolecules* **6**, 309-315 (1984).
85 Sellers, L. A., Allen, A., Morris, E. R. & Ross-Murphy, S. B. Mechanical characterization and properties of gastrointestinal mucus gel. *Biorheology* **24**, 615-623, doi:10.3233/bir-1987-24614 (1987).
86 Sellers, L. A. & Allen, A. Gastrointestinal mucus gel rheology. *Symp Soc Exp Biol* **43**, 65-71 (1989).
87 Sellers, L. A., Allen, A., Morris, E. R. & Ross-Murphy, S. B. The rheology of pig small intestinal and colonic mucus: weakening of gel structure by non-mucin components. *Biochim Biophys Acta* **1115**, 174-179, doi:10.1016/0304-4165(91)90027-e (1991).
88 Macpherson, A. J., McCoy, K. D., Johansen, F. E. & Brandtzaeg, P. The immune geography of IgA induction and function. *Mucosal Immunol* **1**, 11-22, doi:10.1038/mi.2007.6 (2008).
89 Jakobsson, H. E. *et al.* The composition of the gut microbiota shapes the colon mucus barrier. *EMBO Rep* **16**, 164-177, doi:10.15252/embr.201439263 (2015).
90 Caldara, M. *et al.* Mucin biopolymers prevent bacterial aggregation by retaining cells in the free-swimming state. *Curr Biol* **22**, 2325-2330, doi:10.1016/j.cub.2012.10.028 (2012).
91 Silva, A. J., Pham, K. & Benitez, J. A. Haemagglutinin/protease expression and mucin gel penetration in El Tor biotype Vibrio cholerae. *Microbiology* **149**, 1883-1891, doi:10.1099/mic.0.26086-0 (2003).
92 Sonnenburg, E. D. *et al.* Diet-induced extinctions in the gut microbiota compound over generations. *Nature* **529**, 212-215, doi:10.1038/nature16504 (2016).
93 Juge, N. Microbial adhesins to gastrointestinal mucus. *Trends Microbiol* **20**, 30-39, doi:10.1016/j.tim.2011.10.001 (2012).
94 Rawls, J. F., Mahowald, M. A., Ley, R. E. & Gordon, J. I. Reciprocal gut microbiota transplants from zebrafish and mice to germ-free recipients reveal host habitat selection. *Cell* **127**, 423-433, doi:10.1016/j.cell.2006.08.043 (2006).
95 Barr, J. J. *et al.* Bacteriophage adhering to mucus provide a non-host-derived immunity. *Proc Natl Acad Sci U S A* **110**, 10771-10776, doi:10.1073/pnas.1305923110 (2013).
96 El Aidy, S. *et al.* Temporal and spatial interplay of microbiota and intestinal mucosa drive establishment of immune homeostasis in conventionalized mice. *Mucosal Immunol* **5**, 567-579, doi:10.1038/mi.2012.32 (2012).
97 Johansson, M. E. *et al.* Normalization of Host Intestinal Mucus Layers Requires Long-Term Microbial Colonization. *Cell Host Microbe* **18**, 582-592, doi:10.1016/j.chom.2015.10.007 (2015).
98 El Aidy, S. *et al.* Transient inflammatory-like state and microbial dysbiosis are pivotal in establishment of mucosal homeostasis during colonisation of germ-free mice. *Benef Microbes* **5**, 67-77, doi:10.3920/BM2013.0018 (2014).
99 Willing, B. P., Russell, S. L. & Finlay, B. B. Shifting the balance: antibiotic effects on host-microbiota mutualism. *Nat Rev Microbiol* **9**, 233-243, doi:10.1038/nrmicro2536 (2011).
100 Knoop, K. A., McDonald, K. G., Kulkarni, D. H. & Newberry, R. D. Antibiotics promote inflammation through the translocation of native commensal colonic bacteria. *Gut* **65**, 1100-1109, doi:10.1136/gutjnl-2014-309059 (2016).
101 Wlodarska, M. *et al.* Antibiotic treatment alters the colonic mucus layer and predisposes the host to exacerbated Citrobacter rodentium-induced colitis. *Infect Immun* **79**, 1536-1545, doi:10.1128/IAI.01104-10 (2011).

102 Bouwstra, J. A., Honeywell-Nguyen, P. L., Gooris, G. S. & Ponec, M. Structure of the skin barrier and its modulation by vesicular formulations. *Prog Lipid Res* **42**, 1-36, doi:10.1016/s0163-7827(02)00028-0 (2003).
103 Sandby-Moller, J., Poulsen, T. & Wulf, H. C. Epidermal thickness at different body sites: relationship to age, gender, pigmentation, blood content, skin type and smoking habits. *Acta Derm Venereol* **83**, 410-413, doi:10.1080/00015550310015419 (2003).
104 Koehler, M. J. *et al.* In vivo measurement of the human epidermal thickness in different localizations by multiphoton laser tomography. *Skin Res Technol* **16**, 259-264, doi:10.1111/j.1600-0846.2010.00437.x (2010).
105 Blanpain, C. & Fuchs, E. Epidermal stem cells of the skin. *Annu Rev Cell Dev Biol* **22**, 339-373, doi:10.1146/annurev.cellbio.22.010305.104357 (2006).
106 Elias, P. M. Stratum corneum defensive functions: an integrated view. *J Invest Dermatol* **125**, 183-200, doi:10.1111/j.0022-202X.2005.23668.x (2005).
107 Elias, P. M. Epidermal lipids, barrier function, and desquamation. *J Invest Dermatol* **80**, 44s-49s, doi:10.1038/jid.1983.12 (1983).
108 Egawa, M., Hirao, T. & Takahashi, M. In vivo estimation of stratum corneum thickness from water concentration profiles obtained with Raman spectroscopy. *Acta Derm Venereol* **87**, 4-8, doi:10.2340/00015555-0183 (2007).
109 Hitomi, K. Transglutaminases in skin epidermis. *Eur J Dermatol* **15**, 313-319 (2005).
110 Lee, S. H. *et al.* Calcium and potassium are important regulators of barrier homeostasis in murine epidermis. *J Clin Invest* **89**, 530-538, doi:10.1172/JCI115617 (1992).
111 Nemes, Z. & Steinert, P. M. Bricks and mortar of the epidermal barrier. *Exp Mol Med* **31**, 5-19, doi:10.1038/emm.1999.2 (1999).
112 van Smeden, J., Janssens, M., Gooris, G. S. & Bouwstra, J. A. The important role of stratum corneum lipids for the cutaneous barrier function. *Biochim Biophys Acta* **1841**, 295-313, doi:10.1016/j.bbalip.2013.11.006 (2014).
113 Feingold, K. R. & Elias, P. M. Role of lipids in the formation and maintenance of the cutaneous permeability barrier. *Biochim Biophys Acta* **1841**, 280-294, doi:10.1016/j.bbalip.2013.11.007 (2014).
114 Baroni, A. *et al.* Structure and function of the epidermis related to barrier properties. *Clin Dermatol* **30**, 257-262, doi:10.1016/j.clindermatol.2011.08.007 (2012).
115 Man, M. M., Feingold, K. R., Thornfeldt, C. R. & Elias, P. M. Optimization of physiological lipid mixtures for barrier repair. *J Invest Dermatol* **106**, 1096-1101, doi:10.1111/1523-1747.ep12340135 (1996).
116 Wertz, P. W. Current understanding of skin biology pertinent to skin penetration: skin biochemistry. *Skin Pharmacol Physiol* **26**, 217-226, doi:10.1159/000351949 (2013).
117 Pascher, I., Lundmark, M., Nyholm, P. G. & Sundell, S. Crystal structures of membrane lipids. *Biochim Biophys Acta* **1113**, 339-373, doi:10.1016/0304-4157(92)90006-v (1992).
118 Groen, D., Poole, D. S., Gooris, G. S. & Bouwstra, J. A. Is an orthorhombic lateral packing and a proper lamellar organization important for the skin barrier function? *Biochim Biophys Acta* **1808**, 1529-1537, doi:10.1016/j.bbamem.2010.10.015 (2011).
119 Joke A Bouwstra, P. L. H.-N., Gert S Gooris, Maria Ponec. Structure of the skin barrier and its modulation by vesicular formulations. *Progress in Lipid Research* **42**, 1-36 (2003).
120 Brandner, J. M., Haftek, M. & Niessen, C. M. Adherens junctions, desmosomes and tight junctions in epidermal barrier function. *The Open Dermatology Journal* **4** (2010).
121 Elias, P. M. The skin barrier as an innate immune element. *Semin Immunopathol* **29**, 3-14, doi:10.1007/s00281-007-0060-9 (2007).
122 Anderson, J. M. & Van Itallie, C. M. Physiology and function of the tight junction. *Cold Spring Harb Perspect Biol* **1**, a002584-a002584, doi:10.1101/cshperspect.a002584 (2009).
123 Ohman, H. & Vahlquist, A. In vivo studies concerning a pH gradient in human stratum corneum and upper epidermis. *Acta Derm Venereol* **74**, 375-379, doi:10.2340/0001555574375379 (1994).

124 Mauro, T. M. in *Skin Barrier* (eds Peter M. Elias & Kenneth R. Feingold) 223-230 (Taylor & Francis Group, 2006).
125 Lademann, J. *et al.* Penetration and storage of particles in human skin: perspectives and safety aspects. *Eur J Pharm Biopharm* **77**, 465-468, doi:10.1016/j.ejpb.2010.10.015 (2011).
126 Lademann, J. *et al.* Hair follicles as a target structure for nanoparticles. *Journal of Innovative Optical Health Sciences* **08**, 1530004, doi:10.1142/s1793545815300049 (2015).
127 Radtke, M., Patzelt, A., Knorr, F., Lademann, J. & Netz, R. R. Ratchet effect for nanoparticle transport in hair follicles. *Eur J Pharm Biopharm* **116**, 125-130, doi:10.1016/j.ejpb.2016.10.005 (2017).
128 Nino, M., Calabro, G. & Santoianni, P. Topical delivery of active principles: the field of dermatological research. *Dermatol Online J* **16**, 4 (2010).
129 Schroter, A. *et al.* Basic nanostructure of stratum corneum lipid matrices based on ceramides [EOS] and [AP]: a neutron diffraction study. *Biophys J* **97**, 1104-1114, doi:10.1016/j.bpj.2009.05.041 (2009).
130 Döge, N. *et al.* Identification of polystyrene nanoparticle penetration across intact skin barrier as rare event at sites of focal particle aggregations. *J. Biophotonics* **11**, e201700169, doi:10.1002/jbio.201700169 (2018).
131 Li, S. K. & Peck, K. D. Passive and iontophoretic transport through the skin polar pathway. *Skin Pharmacol Physiol* **26**, 243-253, doi:10.1159/000351926 (2013).
132 Schatzlein, A. & Cevc, G. Non-uniform cellular packing of the stratum corneum and permeability barrier function of intact skin: a high-resolution confocal laser scanning microscopy study using highly deformable vesicles (Transfersomes). *Br J Dermatol* **138**, 583-592, doi:10.1046/j.1365-2133.1998.02166.x (1998).
133 Elias, P. M., Tsai, J., Menon, G. K., Holleran, W. M. & Feingold, K. R. The potential of metabolic interventions to enhance transdermal drug delivery. *J Investig Dermatol Symp Proc* **7**, 79-85, doi:10.1046/j.1523-1747.2002.19632.x (2002).
134 Menon, G. K. & Elias, P. M. Morphologic basis for a pore-pathway in mammalian stratum corneum. *Skin Pharmacol* **10**, 235-246, doi:10.1159/000211511 (1997).
135 Zhang, Z., Tsai, P. C., Ramezanli, T. & Michniak-Kohn, B. B. Polymeric nanoparticles-based topical delivery systems for the treatment of dermatological diseases. *Wires Nanomed Nanobi* **5**, 205-218, doi:10.1002/wnan.1211 (2013).
136 Goyal, R., Macri, L. K., Kaplan, H. M. & Kohn, J. Nanoparticles and nanofibers for topical drug delivery. *Journal of Controlled Release* **240**, 77-92 (2016).
137 Borgia, S. L. *et al.* Lipid nanoparticles for skin penetration enhancement-correlation to drug localization within the particle matrix as determined by fluorescence and parelectric spectroscopy. *Journal of Controlled Release* **110**, 151-163, doi:10.1016/j.jconrel.2005.09.045 (2005).
138 Küchler, S. *et al.* Nanoparticles for skin penetration enhancement - A comparison of a dendritic core-multishell-nanotransporter and solid lipid nanoparticles. *Eur. J. Pharm. Biopharm.* **71**, 243-250, doi:10.1016/j.ejpb.2008.08.019 (2009).
139 Embil, K. & Nacht, S. The Microsponge(R) Delivery System (MDS): A topical delivery system with reduced irritancy incorporating multiple triggering mechanisms for the release of actives. *J Microencapsul* **13**, 575-588, doi:Doi 10.3109/02652049609026042 (1996).
140 Haag, R. Supramolecular drug-delivery systems based on polymeric core-shell architectures. *Angew Chem Int Edit* **43**, 278-282, doi:10.1002/anie.200301694 (2004).
141 Gronbach, L. *et al.* A multilayered epithelial mucosa model of head neck squamous cell carcinoma for analysis of tumor-microenvironment interactions and drug development. *Biomaterials* **258**, 120277, doi:10.1016/j.biomaterials.2020.120277 (2020).
142 Guterres, S. S., Alves, M. P. & Pohlmann, A. R. Polymeric nanoparticles, nanospheres and nanocapsules, for cutaneous applications. *Drug Target Insights* **2**, 147-157 (2007).

143 Alnasif, N. *et al.* Penetration of normal, damaged and diseased skin--an in vitro study on dendritic core-multishell nanotransporters. *J. Control. Release* **185**, 45-50, doi:10.1016/j.jconrel.2014.04.006 (2014).
144 Licha, K. *et al.* Fluorescence imaging with multifunctional polyglycerol sulfates: novel polymeric near-IR probes targeting inflammation. *Bioconjug Chem* **22**, 2453-2460, doi:10.1021/bc2002727 (2011).
145 Monsigny, M., Roche, A. C., Sene, C., Magetdana, R. & Delmotte, F. Sugar-Lectin Interactions - How Does Wheat-Germ-Agglutinin Bind Sialoglycoconjugates. *Eur J Biochem* **104**, 147-153, doi:DOI 10.1111/j.1432-1033.1980.tb04410.x (1980).
146 Alexiev, U., Rimke, I. & Pohlmann, T. Elucidation of the nature of the conformational changes of the EF-interhelical loop in bacteriorhodopsin and of the helix VIII on the cytoplasmic surface of bovine rhodopsin: a time-resolved fluorescence depolarization study. *J Mol Biol* **328**, 705-719 (2003).
147 Kim, T. Y., Winkler, K. & Alexiev, U. Picosecond multidimensional fluorescence spectroscopy: a tool to measure real-time protein dynamics during function. *Photochem Photobiol* **83**, 378-384, doi:10.1562/2006-06-21-RA-943 (2007).
148 Boreham, A. *et al.* Exploiting Fluorescence Lifetime Plasticity in FLIM: Target Molecule Localization in Cells and Tissues. *ACS Med. Chem. Lett.* **2**, 724-728, doi:10.1021/ml200092m (2011).
149 Volz, P. *et al.* White-Light Supercontinuum Laser-Based Multiple Wavelength Excitation for TCSPC-FLIM of Cutaneous Nanocarrier Uptake. *Z. Phys. Chem* **232**, 671-688, doi:10.1515/zpch-2017-1050 (2018).
150 Gerritsen, H. C., Asselbergs, M. A. H., Agronskaia, A. V. & Van Sark, W. G. J. H. M. Fluorescence lifetime imaging in scanning microscopes: acquisition speed, photon economy and lifetime resolution. *J Microsc-Oxford* **206**, 218-224, doi:DOI 10.1046/j.1365-2818.2002.01031.x (2002).
151 Kollner, M. & Wolfrum, J. How Many Photons Are Necessary for Fluorescence-Lifetime Measurements. *Chem Phys Lett* **200**, 199-204, doi:Doi 10.1016/0009-2614(92)87068-Z (1992).
152 Brodwolf, R. *et al.* Faster, sharper, more precise: Automated Cluster-FLIM in preclinical testing directly identifies the intracellular fate of theranostics in live cells and tissue. *Theranostics* **10**, 6322-6336, doi:10.7150/thno.42581 (2020).
153 Olson, F., Hunt, C. A., Szoka, F. C., Vail, W. J. & Papahadjopoulos, D. Preparation of liposomes of defined size distribution by extrusion through polycarbonate membranes. *Biochim Biophys Acta* **557**, 9-23, doi:10.1016/0005-2736(79)90085-3 (1979).
154 Cooperation, O. f. E. & Development. (OECD Paris, 1995).
155 Teichmann, A. *et al.* Differential stripping: determination of the amount of topically applied substances penetrated into the hair follicles. *J Invest Dermatol* **125**, 264-269, doi:10.1111/j.0022-202X.2005.23779.x (2005).
156 Rao, J. P. & Geckeler, K. E. Polymer nanoparticles: Preparation techniques and size-control parameters. *Prog Polym Sci* **36**, 887-913, doi:10.1016/j.progpolymsci.2011.01.001 (2011).
157 Dong, P. *et al.* pH-sensitive Eudragit(R) L 100 nanoparticles promote cutaneous penetration and drug release on the skin. *J Control Release* **295**, 214-222, doi:10.1016/j.jconrel.2018.12.045 (2019).
158 Behrens, I., Stenberg, P., Artursson, P. & Kissel, T. Transport of lipophilic drug molecules in a new mucus-secreting cell culture model based on HT29-MTX cells. *Pharm Res* **18**, 1138-1145, doi:10.1023/a:1010974909998 (2001).
159 Pinto, M. *et al.* Enterocyte-Like Differentiation and Polarization of the Human-Colon Carcinoma Cell-Line Caco-2 in Culture. *Biol Cell* **47**, 323-330 (1983).
160 Meaney, C. & O'Driscoll, C. Mucus as a barrier to the permeability of hydrophilic and lipophilic compounds in the absence and presence of sodium taurocholate micellar systems

using cell culture models. *Eur J Pharm Sci* **8**, 167-175, doi:Doi 10.1016/S0928-0987(99)00007-X (1999).
161 Merlin, D. *et al.* ATP-stimulated electrolyte and mucin secretion in the human intestinal goblet cell line HT29-Cl.16E. *J Membr Biol* **137**, 137-149, doi:10.1007/bf00233483 (1994).
162 Boreham, A. *et al.* Temperature and environment dependent dynamic properties of a dendritic polyglycerol sulfate. *Polym. Adv. Technol.* **25**, 1329-1336, doi:10.1002/pat.3355 (2014).
163 Boreham, A., Brodwolf, R., Walker, K., Haag, R. & Alexiev, U. Time-Resolved Fluorescence Spectroscopy and Fluorescence Lifetime Imaging Microscopy for Characterization of Dendritic Polymer Nanoparticles and Applications in Nanomedicine. *Molecules* **22**, doi:10.3390/molecules22010017 (2016).
164 Dernedde, J. *et al.* Dendritic polyglycerol sulfates as multivalent inhibitors of inflammation. *P Natl Acad Sci USA* **107**, 19679-19684, doi:10.1073/pnas.1003103107 (2010).
165 Sanborn, M. E., Connolly, B. K., Gurunathan, K. & Levitus, M. Fluorescence properties and photophysics of the sulfoindocyanine Cy3 linked covalently to DNA. *J Phys Chem B* **111**, 11064-11074, doi:10.1021/jp072912u (2007).
166 Hughes, L. D., Rawle, R. J. & Boxer, S. G. Choose Your Label Wisely: Water-Soluble Fluorophores Often Interact with Lipid Bilayers. *Plos One* **9**, doi:ARTN e87649 10.1371/journal.pone.0087649 (2014).
167 Nojima, Y. & Iwata, K. Viscosity heterogeneity inside lipid bilayers of single-component phosphatidylcholine liposomes observed with picosecond time-resolved fluorescence spectroscopy. *J Phys Chem B* **118**, 8631-8641, doi:10.1021/jp503921e (2014).
168 Heimburg, T. A model for the lipid pretransition: coupling of ripple formation with the chain-melting transition. *Biophys J* **78**, 1154-1165, doi:10.1016/S0006-3495(00)76673-2 (2000).
169 Levanon, A. & Kohn, A. Changes in cell membrane microviscosity associated with adsorption of viruses. Differences between fusing and non-fusing viruses. *FEBS Lett* **85**, 245-248, doi:10.1016/0014-5793(78)80465-7 (1978).
170 Kubankova, M., Lopez-Duarte, I., Kiryushko, D. & Kuimova, M. K. Molecular rotors report on changes in live cell plasma membrane microviscosity upon interaction with beta-amyloid aggregates. *Soft Matter* **14**, 9466-9474, doi:10.1039/c8sm01633j (2018).
171 Lopez-Duarte, I., Vu, T. T., Izquierdo, M. A., Bull, J. A. & Kuimova, M. K. A molecular rotor for measuring viscosity in plasma membranes of live cells. *Chem Commun (Camb)* **50**, 5282-5284, doi:10.1039/c3cc47530a (2014).
172 Brennan, M.-L. & Schrijver, I. Cystic fibrosis: a review of associated phenotypes, use of molecular diagnostic approaches, genetic characteristics, progress, and dilemmas. *The Journal of Molecular Diagnostics* **18**, 3-14 (2016).
173 Del Giudice, F., Tassieri, M., Oelschlaeger, C. & Shen, A. Q. When microrheology, bulk rheology, and microfluidics meet: broadband rheology of hydroxyethyl cellulose water solutions. *Macromolecules* **50**, 2951-2963 (2017).
174 Wang, Y. Y. *et al.* The Microstructure and Bulk Rheology of Human Cervicovaginal Mucus Are Remarkably Resistant to Changes in pH. *Biomacromolecules* **14**, 4429-4435, doi:10.1021/bm401356q (2013).
175 Kirch, J. *et al.* Optical tweezers reveal relationship between microstructure and nanoparticle penetration of pulmonary mucus. *P Natl Acad Sci USA* **109**, 18355-18360, doi:10.1073/pnas.1214066109 (2012).
176 Ibarz, A., Pagan, J. & Miguelsanz, R. Rheology of Clarified Fruit Juices .2. Black-Currant Juices. *J Food Eng* **15**, 63-73, doi:Doi 10.1016/0260-8774(92)90040-D (1992).
177 Wiedmann, T. S., Liang, W. & Herrington, H. Excluded volume effect of rat intestinal mucin on taurocholate/phosphatidylcholine mixed micelles. *J Colloid Interf Sci* **270**, 321-328, doi:10.1016/j.jcis.2003.09.040 (2004).

178 Fielding, D. Practical issues in autofluorescence bronchoscopy with Storz D Light bronchoscope. *Photodiagnosis Photodyn Ther* **1**, 247-251, doi:10.1016/S1572-1000(04)00063-8 (2004).
179 Heredia, R. B. *et al.* Autofluorescence as a tool to study mucus secretion in Eisenia foetida. *Comp Biochem Physiol A Mol Integr Physiol* **151**, 407-414, doi:10.1016/j.cbpa.2007.01.726 (2008).
180 Wu, Y., Xi, P., Qu, J., Cheung, T. H. & Yu, M. Y. Depth-resolved fluorescence spectroscopy reveals layered structure of tissue. *Opt Express* **12**, 3218-3223, doi:10.1364/opex.12.003218 (2004).
181 Mahler, G. J., Shuler, M. L. & Glahn, R. P. Characterization of Caco-2 and HT29-MTX cocultures in an in vitro digestion/cell culture model used to predict iron bioavailability. *J Nutr Biochem* **20**, 494-502, doi:10.1016/j.jnutbio.2008.05.006 (2009).
182 Lesuffleur, T., Barbat, A., Dussaulx, E. & Zweibaum, A. Growth Adaptation to Methotrexate of Ht-29 Human Colon-Carcinoma Cells Is Associated with Their Ability to Differentiate into Columnar Absorptive and Mucus-Secreting Cells. *Cancer Res* **50**, 6334-6343 (1990).
183 Merlin, D. *et al.* Atp-Stimulated Electrolyte and Mucin Secretion in the Human Intestinal Goblet Cell-Line Ht29-Cl.16e. *J Membrane Biol* **137**, 137-149 (1994).
184 Ensign, L. M., Cone, R. & Hanes, J. Oral drug delivery with polymeric nanoparticles: The gastrointestinal mucus barriers. *Adv Drug Deliver Rev* **64**, 557-570, doi:10.1016/j.addr.2011.12.009 (2012).
185 Barry, B. W. Drug delivery routes in skin: a novel approach. *Adv Drug Deliv Rev* **54 Suppl 1**, S31-40 (2002).
186 Benson, H. A. Transdermal drug delivery: penetration enhancement techniques. *Curr Drug Deliv* **2**, 23-33 (2005).
187 Khalid, A. *et al.* Strategies for improving drug delivery: nanocarriers and microenvironmental priming. *Expert Opin Drug Del* **14**, 865-877, doi:10.1080/17425247.2017.1243527 (2017).
188 Lademann, J. *et al.* Hair follicles as a target structure for nanoparticles. *J Innov Opt Heal Sci* **8**, doi:10.1142/S1793545815300049 (2015).
189 Barenholz, Y. Doxil(R)--the first FDA-approved nano-drug: lessons learned. *J Control Release* **160**, 117-134, doi:10.1016/j.jconrel.2012.03.020 (2012).
190 Schulz, R. *et al.* Data-based modeling of drug penetration relates human skin barrier function to the interplay of diffusivity and free-energy profiles. *Proc Natl Acad Sci U S A* **114**, 3631-3636, doi:10.1073/pnas.1620636114 (2017).
191 Schulz, R. *et al.* Modeling of Drug Diffusion Based on Concentration Profiles in Healthy and Damaged Human Skin. *Biophysical Journal* **117**, 998-1008, doi:10.1016/j.bpj.2019.07.027 (2019).
192 Lohan, S. B. *et al.* Nanocrystals for Improved Drug Delivery of Dexamethasone in Skin Investigated by EPR Spectroscopy. *Pharmaceutics* **12**, doi:10.3390/pharmaceutics12050400 (2020).
193 Jepps, O. G., Dancik, Y., Anissimov, Y. G. & Roberts, M. S. Modeling the human skin barrier--towards a better understanding of dermal absorption. *Adv Drug Deliv Rev* **65**, 152-168, doi:10.1016/j.addr.2012.04.003 (2013).
194 Otberg, N. *et al.* Variations of hair follicle size and distribution in different body sites. *J Invest Dermatol* **122**, 14-19, doi:10.1046/j.0022-202X.2003.22110.x (2004).
195 Dimde, M. *et al.* Synthesis and Validation of Functional Nanogels as pH-Sensors in the Hair Follicle. *Macromol Biosci* **17**, doi:10.1002/mabi.201600505 (2017).
196 Warner, R. R., Myers, M. C. & Taylor, D. A. Electron probe analysis of human skin: determination of the water concentration profile. *J Invest Dermatol* **90**, 218-224 (1988).
197 Freinkel, R. K. & Traczyk, T. N. Lipid composition and acid hydrolase content of lamellar granules of fetal rat epidermis. *J Invest Dermatol* **85**, 295-298 (1985).
198 Landmann, L. The epidermal permeability barrier. *Anat Embryol (Berl)* **178**, 1-13 (1988).

199 Cheng, T. J. *et al.* Computation of octanol-water partition coefficients by guiding an additive model with knowledge. *J Chem Inf Model* **47**, 2140-2148, doi:DOI 10.1021/ci700257y (2007).
200 Hansch, C., Leo, A. & Hoekman, D. Exploring QSAR. Hydrophobic, electronic, and steric constants. ACS Professional Reference Book. *ACS, Washington* (1995).
201 Quitevis, E. L., Marcus, A. H. & Fayer, M. D. Dynamics of Ionic Lipophilic Probes in Micelles - Picosecond Fluorescence Depolarization Measurements. *J Phys Chem-Us* **97**, 5762-5769, doi:DOI 10.1021/j100123a049 (1993).
202 Chow, D., Guo, L., Gai, F. & Goulian, M. Fluorescence Correlation Spectroscopy Measurements of the Membrane Protein TetA in Escherichia coli Suggest Rapid Diffusion at Short Length Scales. *Plos One* **7**, doi:10.1371/journal.pone.0048600 (2012).
203 Boreham, A., Volz, P., Peters, D., Keck, C. M. & Alexiev, U. Determination of nanostructures and drug distribution in lipid nanoparticles by single molecule microscopy. *Eur J Pharm Biopharm* **110**, 31-38, doi:10.1016/j.ejpb.2016.10.020 (2017).
204 Brandner, J. M. *et al.* Organization and formation of the tight junction system in human epidermis and cultured keratinocytes. *Eur J Cell Biol* **81**, 253-263, doi:10.1078/0171-9335-00244 (2002).
205 Bray, F. *et al.* Global cancer statistics 2018: GLOBOCAN estimates of incidence and mortality worldwide for 36 cancers in 185 countries. *CA: a cancer journal for clinicians* **68**, 394-424 (2018).
206 Siegel, R. L., Miller, K. D. & Jemal, A. Cancer statistics, 2019. *CA Cancer J Clin* **69**, 7-34, doi:10.3322/caac.21551 (2019).
207 Alsahafi, E. *et al.* Clinical update on head and neck cancer: molecular biology and ongoing challenges. *Cell Death Dis* **10**, doi:10.1038/s41419-019-1769-9 (2019).
208 Bailey, J., Thew, M. & Balls, M. An analysis of the use of animal models in predicting human toxicology and drug safety. *Alternatives to Laboratory Animals* **42**, 181-199 (2014).
209 Hearnden, V. *et al.* New developments and opportunities in oral mucosal drug delivery for local and systemic disease. *Adv Drug Deliver Rev* **64**, 16-28, doi:10.1016/j.addr.2011.02.008 (2012).
210 Volz, P. *et al.* Pitfalls in using fluorescence tagging of nanomaterials: tecto-dendrimers in skin tissue as investigated by Cluster-FLIM. *Ann. N. Y. Acad. Sci.* **1405**, 202-214, doi:10.1111/nyas.13473 (2017).
211 Witting, M. *et al.* Interactions of hyaluronic Acid with the skin and implications for the dermal delivery of biomacromolecules. *Mol. Pharm.* **12**, 1391-1401, doi:10.1021/mp500676e (2015).
212 Holbro, T. & Hynes, N. E. ErbB receptors: Directing key signaling networks throughout life. *Annu Rev Pharmacol* **44**, 195-217, doi:DOI 10.1146/annurev.pharmtox.44.101802.121440 (2004).
213 Arteaga, C. L. ErbB-targeted therapeutic approaches in human cancer. *Experimental Cell Research* **284**, 122-130, doi:10.1016/S0014-4827(02)00104-0 (2003).
214 Li, S. Q. *et al.* Structural basis for inhibition of the epidermal growth factor receptor by cetuximab. *Cancer Cell* **7**, 301-311, doi:10.1016/j.ccr.2005.03.003 (2005).
215 Kascakova, S. *et al.* In vivo quantification of photosensitizer fluorescence in the skin-fold observation chamber using dual-wavelength excitation and NIR imaging. *Lasers Med Sci* **26**, 789-801, doi:10.1007/s10103-011-0888-z (2011).
216 Gurfinkel, M. *et al.* Pharmacokinetics of ICG and HPPH-car for the detection of normal and tumor tissue using fluorescence, near-infrared reflectance imaging: a case study. *Photochem Photobiol* **72**, 94-102, doi:10.1562/0031-8655(2000)072<0094:poiahc>2.0.co;2 (2000).
217 Diamond, K. R., Malysz, P. P., Hayward, J. E. & Patterson, M. S. Quantification of fluorophore concentration in vivo using two simple fluorescence-based measurement techniques. *J Biomed Opt* **10**, doi:10.1117/1.1887932 (2005).

218 Herman, B. W., X.F.; Wodnicki, P.; Perisamy, A.; Mahajan, N.; Berry, G.; Gordon, G. in *Applied Fluorescence in Chemistry, Biology and Medicine* Vol. 1 (ed Bernd Strehmel Wolfgang Rettig, Sigurd Schrader, Holger Seifert) Ch. 20, 562 (Springer-Verlag Berlin Heidelberg, 1999).

219 Chen, L. C., Lloyd, W. R., 3rd, Chang, C. W., Sud, D. & Mycek, M. A. Fluorescence lifetime imaging microscopy for quantitative biological imaging. *Methods Cell Biol* **114**, 457-488, doi:10.1016/B978-0-12-407761-4.00020-8 (2013).

220 Kuppusamy, P., Wang, P., Chzhan, M. & Zweier, J. L. High resolution electron paramagnetic resonance imaging of biological samples with a single line paramagnetic label. *Magn Reson Med* **37**, 479-483, doi:10.1002/mrm.1910370402 (1997).

221 Kilic, S. *et al.* Single-molecule FRET reveals multiscale chromatin dynamics modulated by HP1alpha. *Nat Commun* **9**, 235, doi:10.1038/s41467-017-02619-5 (2018).

222 Vogt, A. *et al.* Nanocarriers for drug delivery into and through the skin - do existing technologies match clinical challenges? *J. Control. Release* **242**, 3-15, doi:DOI: 10.1016/j.jconrel.2016.07.027 (2016).

223 Frombach, J. *et al.* Core-multishell nanocarriers enhance drug penetration and reach keratinocytes and antigen-presenting cells in intact human skin. *J Control Release* **299**, 138-148, doi:10.1016/j.jconrel.2019.02.028 (2019).

224 Joseph, B. *et al.* Distance Measurement on an Endogenous Membrane Transporter in E. coli Cells and Native Membranes Using EPR Spectroscopy. *Angew Chem Int Ed Engl* **54**, 6196-6199, doi:10.1002/anie.201501086 (2015).

225 Bertoli, F. *et al.* Magnetic nanoparticles to recover cellular organelles and study the time resolved nanoparticle-cell interactome throughout uptake. *Small* **10**, 3307-3315, doi:10.1002/smll.201303841 (2014).

226 Hubbell, W. L., Cafiso, D. S. & Altenbach, C. Identifying conformational changes with site-directed spin labeling. *Nature Structural Biology* **7**, 735-739 (2000).

227 Kohout, S. C., Corbalan-Garcia, S., Gomez-Fernandez, J. C. & Falke, J. J. C2 domain of protein kinase C alpha: elucidation of the membrane docking surface by site-directed fluorescence and spin labeling. *Biochemistry* **42**, 1254-1265, doi:10.1021/bi026596f (2003).

228 Braem, C. *et al.* Interaction of drug molecules with carrier systems as studied by parelectric spectroscopy and electron spin resonance. *J Control Release* **119**, 128-135, doi:10.1016/j.jconrel.2007.01.017 (2007).

229 Lohan, S. B. *et al.* Investigation of cutaneous penetration properties of stearic acid loaded to dendritic core-multi-shell (CMS) nanocarriers. *Int J Pharm* **501**, 271-277, doi:10.1016/j.ijpharm.2016.02.004 (2016).

230 London, E. Investigation of Membrane-Structure Using Fluorescence Quenching by Spin-Labels - a Review of Recent Studies. *Molecular and Cellular Biochemistry* **45**, 181-188 (1982).

231 Blough, N. V. & Simpson, D. J. Chemically Mediated Fluorescence Yield Switching in Nitroxide Fluorophore Adducts - Optical Sensors of Radical Redox Reactions. *Journal of the American Chemical Society* **110**, 1915-1917, doi:DOI 10.1021/ja00214a041 (1988).

232 Barhate, N., Cekan, P., Massey, A. P. & Sigurdsson, S. T. A nucleoside that contains a rigid nitroxide spin label: A fluorophore in disguise. *Angew Chem Int Edit* **46**, 2655-2658, doi:10.1002/anie.200603993 (2007).

233 Beetge, E., du Plessis, J., Muller, D. G., Goosen, C. & van Rensburg, F. J. The influence of the physicochemical characteristics and pharmacokinetic properties of selected NSAID's on their transdermal absorption. *Int J Pharm* **193**, 261-264, doi:10.1016/s0378-5173(99)00340-3 (2000).

234 Mchedlov-Petrossyan, N. O., Cheipesh, T. A., Roshal, A. D., Doroshenko, A. O. & Vodolazkaya, N. A. Fluorescence of aminofluoresceins as an indicative process allowing one to distinguish between micelles of cationic surfactants and micelle-like aggregates. *Methods Appl Fluores* **4**, doi:10.1088/2050-6120/4/3/034002 (2016).

235 Robert Sjoback, J. N. & Kubista, M. Absorption and fluorescence properties of fluorescein. *Spectrochimica Acta Part A* **51**, L7-L2l (1995).
236 Arbeloa, T. L., Arbeloa, F. L., Bartolome, P. H. & Arbeloa, I. L. On the Mechanism of Radiationless Deactivation of Rhodamines. *Chem Phys* **160**, 123-130, doi:Doi 10.1016/0301-0104(92)87095-Q (1992).
237 Magde, D., Rojas, G. E. & Seybold, P. G. Solvent dependence of the fluorescence lifetimes of xanthene dyes. *Photochemistry and Photobiology* **70**, 737-744, doi:Doi 10.1562/0031-8655(1999)070<0737:Sdotfl>2.3.Co;2 (1999).
238 Volz, P. *et al.* Pitfalls in using fluorescence tagging of nanomaterials: tecto-dendrimers in skin tissue as investigated by Cluster-FLIM. *Annals of the New York Academy of Sciences* **1405**, 202-214, doi:doi:10.1111/nyas.13473 (2017).
239 Watkinson, A. C., Kearney, M. C., Quinn, H. L., Courtenay, A. J. & Donnelly, R. F. Future of the transdermal drug delivery market--have we barely touched the surface? *Expert Opin Drug Deliv* **13**, 523-532, doi:10.1517/17425247.2016.1130034 (2016).
240 Yamamoto, K. *et al.* Selective Probing of the Penetration of Dexamethasone into Human Skin by Soft X-ray Spectromicroscopy. *Anal Chem* **87**, 6173-6179, doi:10.1021/acs.analchem.5b00800 (2015).
241 Vogt, A. *et al.* Nanocarriers for drug delivery into and through the skin - Do existing technologies match clinical challenges? *J Control Release* **242**, 3-15, doi:10.1016/j.jconrel.2016.07.027 (2016).
242 Hashimoto, K. Intercellular spaces of the human epidermis as demonstrated with lanthanum. *J Invest Dermatol* **57**, 17-31, doi:10.1111/1523-1747.ep12292052 (1971).
243 McGuinness, K., Khan, I. J. & Nanda, V. Morphological diversity and polymorphism of self-assembling collagen peptides controlled by length of hydrophobic domains. *ACS Nano* **8**, 12514-12523, doi:10.1021/nn505369d (2014).
244 Elpelt, A. *et al.* Insight into the redox status of inflammatory skin equivalents as determined by EPR spectroscopy. *Chemico-biological interactions* **310**, 108752 (2019).
245 Kuznetsov, A. V. *et al.* Mitochondrial ROS production under cellular stress: comparison of different detection methods. *Anal Bioanal Chem* **400**, 2383-2390, doi:10.1007/s00216-011-4764-2 (2011).
246 Guelluy, P. H. *et al.* Optimizing photodynamic therapy by liposomal formulation of the photosensitizer pyropheophorbide-a methyl ester: in vitro and ex vivo comparative biophysical investigations in a colon carcinoma cell line. *Photochem Photobiol Sci* **9**, 1252-1260, doi:10.1039/c0pp00100g (2010).

Appendix

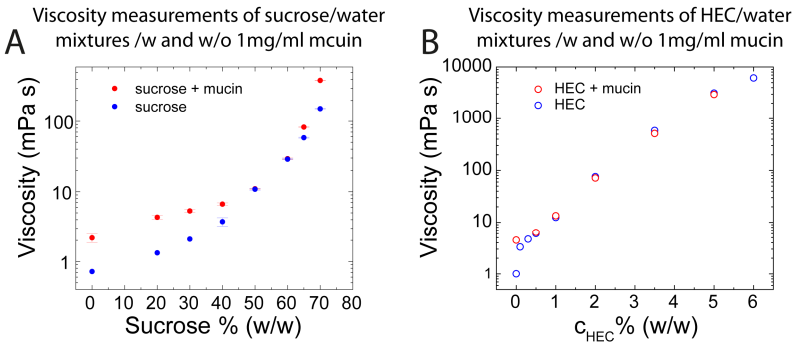

Figure A1. Bulk viscosity measurements using a rotational viscosimeter of sucrose/water mixtures at 37°C (A) and HEC/water mixtures at 20°C (B) with and without mucin.

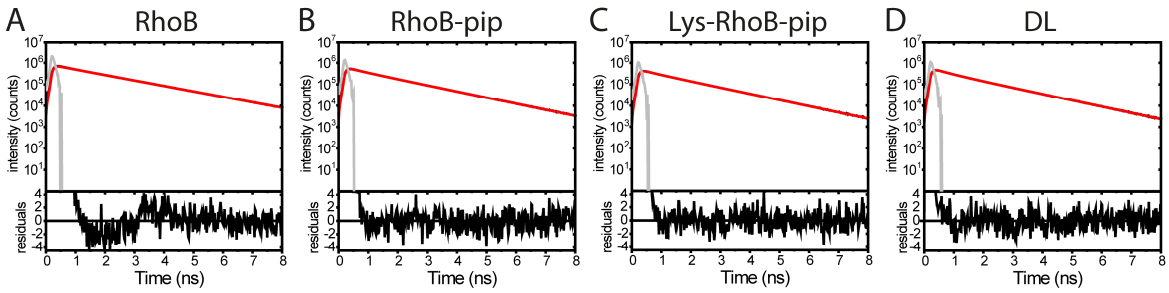

Figure A2. Fluorescence decay traces of DL and its precursors in aqueous solution. (A) RhoB, (B) RhoB-pip, (C) Lys-RhoB-pip, and (D) DL. Shown are the fluorescence decay traces in black and biexponential fit in red. Fit parameters are summarized in Table 6. The instrument response function (IRF; simulated) was fitted together with the fluorescence decay data and is shown in grey. Residuals are displayed below the fit.

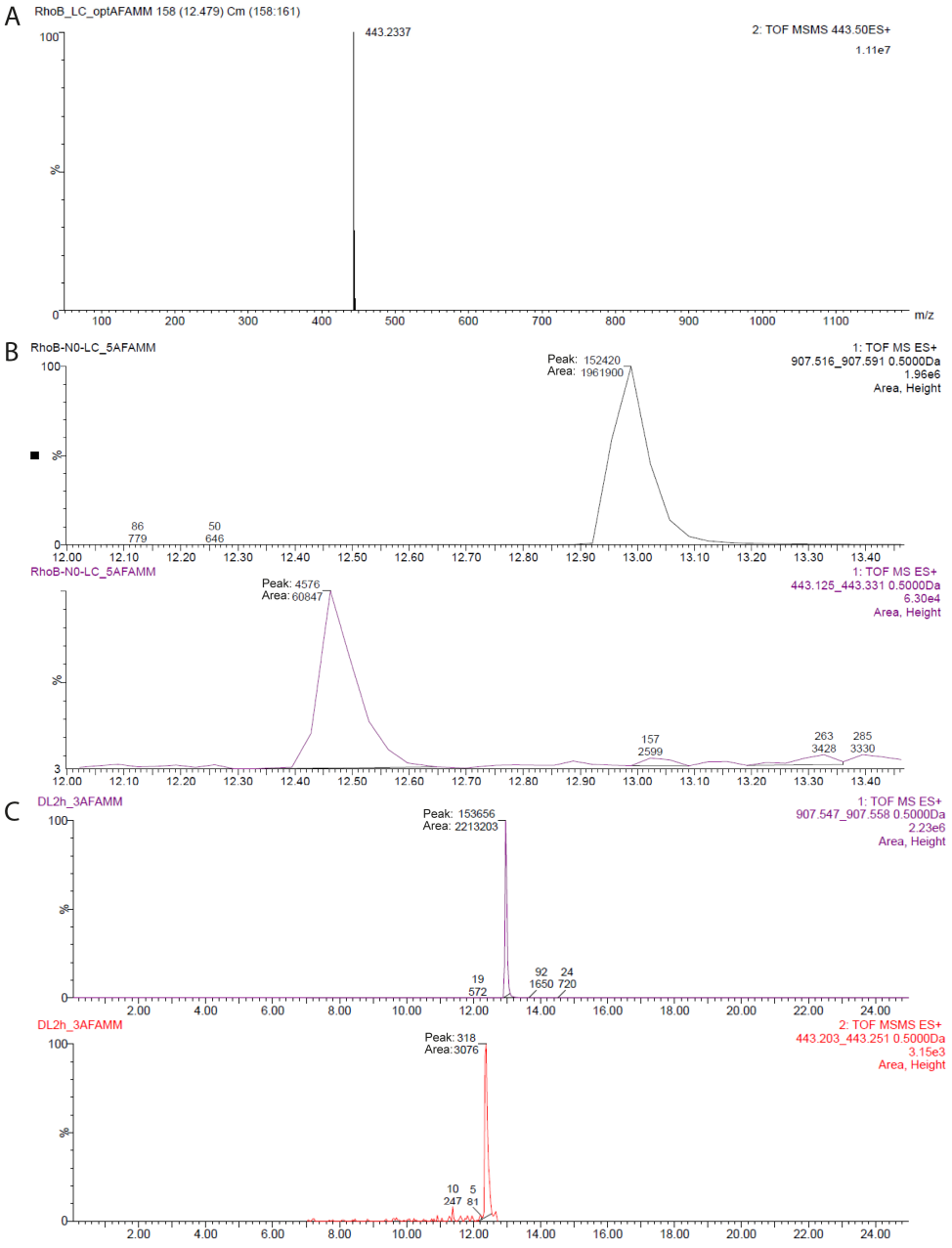

Figure A3. (A) Mass spectrum (ESI TOF) of RhoB, 443.2 Da, calculated 443.6, for $C_{28}H_{31}N_2O_3$. (B) ESI TOF chromatogram at 443.2 Da (lower panel) and 907.5 Da (upper panel) of DL before digestion. Indicated in the graph are peak height and area, showing ~3% free RhoB. (C) ESI TOF chromatogram at 443.2 Da and 907.5 Da of DL after 2h digestion by normal human keratinocytes (NHK) lysate showing no digestion of DL as indicated by the absence of an increase in the fraction of free RhoB. Data are summarized in Table A9.

Table A1. Fit parameters of FLS shown in Figure 3-5. τ_i: fluorescence lifetime of the *i*-th decay component in ns, α_i the corresponding relative amplitude in %. $\tau_{m,a}$: amplitude weighted mean fluorescence lifetime, and χ^2: reduced chi square.

	FLS	α_1(%)	τ_1(ns)	α_2(%)	τ_2(ns)	α_3(%)	τ_3(ns)	α_4(%)	τ_4(ns)	χ^2_{red}	$\bar{\tau}_{pop}$
4 FLS 90 cts/px	Cyan	29.4	0.67	70.2	1.56	0.4	4.98	-	-	1.10	1.48
	Green	53.3	0.17	27.4	0.54	14.3	1.00	5.0	1.56	1.06	0.78
	Magenta	76.1	0.22	19.1	0.53	4.5	1.07	0.3	1.17	2.67	0.46
	Red	94.9	0.15	4.5	0.33	0.6	0.9	-	-	1.14	0.20
5 FLS 170 cts/px	Cyan	34.9	0.78	64.8	1.65	0.3	6.29	-	-	1.39	1.53
	Green	56.7	0.25	32.4	0.77	6.9	1.14	4.0	1.85	1.74	0.83
	Magenta	68.5	0.19	23.8	0.43	7.2	0.87	0.5	1.76	1.34	0.46
	Red	94.8	0.16	4.4	0.40	0.8	0.87	-	-	1.74	0.24
	Yellow	56.5	0.33	29.6	0.97	13.6	2.11	0.3	4.42	1.17	1.30

Table A2. Fit parameter of 0.3 µM WGA-ICC + mucin of porcine stomach type II and sucrose/water-mixtures. τ_i: fluorescence lifetime of the *i*-th decay component in ns, α_i the corresponding relative amplitude in %, $\bar{\tau}_{pop}$: mean fluorescence lifetime and χ^2_{red}: reduced chi square. Experimental conditions: λ_{ex} = 488 nm, λ_{em} > 515 nm, T=37°C.

$c_{sucrose}$ (% w/w)	c_{mucin} (mg/ml)	η(cP)	α_1(%)	α_2(%)	α_3(%)	τ_1(ns)	τ_2(ns)	τ_3(ns)	$\bar{\tau}_{pop}$	χ^2_{red}
0	0	0.7	95.9	3.9	0.2	0.1	0.5	3.2	0.3	2.3
20	0	1.3	70.4	29.1	0.4	0.2	0.4	1.7	0.3	0.8
30	0	2.1	67.5	32.1	0.4	0.2	0.5	2.1	0.4	0.8
40	0	3.7	53.9	45.4	0.7	0.3	0.6	2.1	0.5	0.9
50	0	8.4	45.6	53.3	1.1	0.4	0.8	2.2	0.7	1.0
60	0	28.8	18.8	65.3	15.9	0.3	0.9	1.6	1.0	1.1
65	0	58.2	14.1	64.4	21.5	0.3	1.0	1.7	1.2	1.0
70	0	153.3	17.5	66.6	15.8	0.5	1.3	2.0	1.4	1.0
0	0.1	2.5	90.7	9.0	0.3	0.1	0.3	1.5	0.2	0.6
0	0.5	2.2	89.9	9.7	0.4	0.1	0.3	2.1	0.3	0.9
0	1	2.1	92.1	7.3	0.6	0.1	0.4	2.8	0.4	1.0
0	5	3.2	89.3	7.2	3.5	0.2	1.1	3.9	1.4	1.1
0	10	3.1	86.9	9.3	3.8	0.2	1.0	3.9	1.7	1.3
0	50	6.3	68.7	23.1	8.1	0.2	1.2	4.1	2.2	1.2
0	100	20.2	62.3	27.7	10.0	0.3	1.3	4.1	2.2	2.7
0	1	2.2	92.1	7.3	0.6	0.1	0.4	2.8	0.4	1.0
20	1	4.3	81.1	18.1	0.8	0.2	0.4	3.1	0.6	1.1
30	1	5.3	73.7	25.3	1.0	0.2	0.5	3.0	0.6	1.0
40	1	6.7	67.3	31.6	1.1	0.3	0.6	3.4	0.7	1.0
50	1	11.0	48.6	50.0	1.3	0.3	0.8	3.5	0.9	1.0
60	1	29.3	34.0	63.9	2.1	0.4	1.0	3.6	1.2	1.0
65	1	82.2	29.1	68.8	2.1	0.5	1.3	3.4	1.3	1.0
70	1	386.6	19.0	76.8	4.2	0.5	1.5	3.2	1.6	1.0

Table A3. Fit parameter of ICC in HEC/water-mixtures. τ_i: fluorescence lifetime of the *i*-th decay component in ns, α_i the corresponding relative amplitude in %, $\bar{\tau}_{pop}$: mean fluorescence lifetime and χ^2_{red}: reduced chi square. Experimental conditions: λ_{ex} = 488 nm, λ_{em} > 515 nm, T= 20°C.

c_{HEC} (% w/w)	η(cP)	α_1(%)	α_2(%)	α_3(%)	τ_1(ns)	τ_2(ns)	τ_3(ns)	$\bar{\tau}_{pop}$	χ^2_{red}
0.1	3.3	32.3	27.0	40.7	0.07	0.17	0.19	0.17	6.0
0.3	4.7	60.6	38.5	0.9	0.15	0.21	0.52	0.20	1.3
0.5	6.0	58.7	40.9	0.5	0.14	0.21	1.15	0.21	0.9
1	12	81.4	17.9	0.7	0.15	0.27	1.26	0.24	1.1
2	76	91.2	8.2	0.7	0.17	0.44	1.76	0.31	1.1
3.5	580	91.4	7.3	1.3	0.2	0.59	1.34	0.37	2.8
5	3150	87.1	11.7	1.2	0.18	0.59	2.17	0.49	1.1

Table A4. Fit parameter of WGA-ICC +/- mucin of porcine stomach type II in HEC/water-mixtures. τ_i: fluorescence lifetime of the *i*-th decay component in ns, α_i the corresponding relative amplitude in %, $\bar{\tau}_{pop}$: mean fluorescence lifetime and χ^2_{red}: reduced chi square. Experimental conditions: λ_{ex} = 530 nm, λ_{em} > 545 nm, T=20°C.

c_{HEC} (% w/w)	c_{mucin} (mg/ml)	η(cP)	α_1(%)	α_2(%)	α_3(%)	τ_1(ns)	τ_2(ns)	τ_3(ns)	$\bar{\tau}_{pop}$	χ^2_{red}
0	0	1.0	86.35	12.68	0.96	0.21	0.35	0.87	0.27	1.3
0.5	0	6	90.09	9.05	0.83	0.22	0.49	1.26	0.32	1.3
1	0	12.5	79.09	16.96	3.35	0.2	0.39	1.21	0.51	1.1
2	0	76	87.19	8.57	3.44	0.24	0.73	1.55	0.67	2.3
5	0	3150	78.46	14.61	5.84	0.26	0.91	1.82	0.93	1.5
0	1	4.5	85.4	12.8	1.7	0.21	0.51	1.29	0.40	1.0
0.5	1	6.3	89.7	9.3	1.0	0.21	0.51	1.66	0.39	1.4
1	1	13.5	86.4	12.1	1.4	0.21	0.46	1.35	0.38	1.2
2	1	72	90.1	8.7	1.1	0.23	0.61	1.52	0.42	2.2
5	1	2960	75.3	19.6	4.7	0.21	0.43	1.06	0.49	1.6

Table A5. Fit parameter of WGA-ICC +/- mucin of porcine stomach type II in Ficoll 70/water-mixtures shown in Figure 4-11. Viscosity η was taken from [37] and assumed to be identical with or without 1 mg/ml mucin. τ_i: fluorescence lifetime of the *i*-th decay component in ns, α_i the corresponding relative amplitude in %, $\bar{\tau}_{pop}$: mean fluorescence lifetime and χ^2_{red}: reduced chi square. Experimental conditions: λ_{ex} = 530 nm, λ_{em} > 545 nm, T=20°C.

$c_{Ficoll70}$ (% w/v)	c_{mucin} (mg/ml)	η(mPa s)	α_1(%)	α_2(%)	α_3(%)	α_4(%)	τ_1(ns)	τ_2(ns)	τ_3(ns)	τ_4(ns)	$\bar{\tau}_{pop}$	χ^2_{red}
0	0	1	85.4	12.8	1.7	0.1	0.21	0.51	1.29	2.78	0.40	1.0
50	0	1.5	80.4	16.1	3.4	0.2	0.21	0.53	1.20	2.35	0.46	1.3
100	0	2.6	73.3	20.9	4.7	1.1	0.22	0.53	1.14	1.75	0.55	2.7
150	0	4.7	76.6	19.1	1.7	2.5	0.27	0.76	1.14	1.76	0.64	4.6
200	0	7.9	66.5	25.4	8.1	0.1	0.27	0.68	1.41	3.56	0.73	1.2
250	0	13.3	60.0	26.6	12.4	1.0	0.28	0.65	1.26	2.25	0.78	1.4
300	0	22.2	61.5	27.9	9.0	1.6	0.33	0.84	1.46	2.17	0.88	1.7
0	1	1.0	85.4	12.8	1.7	0.1	0.21	0.51	1.29	2.78	0.40	1.0
50	1	1.5	76.7	15.7	6.5	1.0	0.22	0.44	0.85	1.86	0.48	4.4
100	1	2.6	76.5	18.4	4.4	0.7	0.23	0.60	1.22	2.15	0.57	3.8
150	1	4.7	72.7	20.9	6.0	0.4	0.26	0.68	1.38	2.62	0.68	2.5
200	1	7.9	66.0	19.4	11.6	3.0	0.28	0.64	1.04	1.91	0.75	4.1
250	1	13.3	66.8	24.1	7.5	1.6	0.32	0.83	1.36	2.24	0.82	5.2
300	1	22.2	65.4	30.4	4.2	0.0	0.37	1.01	1.99	0.00	0.89	3.1
$c_{Ficoll400}$ (% w/v)	c_{mucin} (mg/ml)	η(mPa s)	α_1(%)	α_2(%)	α_3(%)	α_4(%)	τ_1(ns)	τ_2(ns)	τ_3(ns)	τ_4(ns)	$\bar{\tau}_{pop}$	χ^2_{red}
0	0	1	85.4	12.8	1.7	0.1	0.21	0.51	1.29	2.78	0.40	1.0
50	0	2.1	75.0	19.3	4.8	0.9	0.20	0.43	0.93	1.73	0.46	1.7
100	0	4.7	75.5	17.8	5.6	1.1	0.22	0.54	1.06	1.89	0.55	2.1
150	0	9.6	74.1	15.5	8.4	2.0	0.25	0.61	0.99	1.84	0.64	4.4
200	0	18.1	69.8	23.8	6.4	0.1	0.27	0.72	1.51	4.50	0.72	1.4
250	0	32.8	67.4	26.1	6.4	0.0	0.30	0.81	1.63	8.01	0.79	1.3
300	0	57.9	65.3	26.3	5.8	2.6	0.32	0.86	1.40	2.03	0.85	4.5
0	1	1.0	85.4	12.8	1.7	0.1	0.21	0.51	1.29	2.78	0.40	1.0
50	1	2.1	76.1	17.7	5.7	0.5	0.22	0.46	1.02	2.23	0.50	2.3
100	1	4.7	72.5	19.4	7.2	1.0	0.23	0.51	1.05	2.10	0.59	3.4
150	1	9.6	70.9	20.3	8.2	0.6	0.25	0.58	1.20	2.44	0.66	2.4
200	1	18.1	68.1	23.3	8.2	0.4	0.27	0.66	1.36	2.67	0.73	1.5
250	1	32.8	59.8	29.3	10.7	0.2	0.28	0.68	1.44	3.26	0.81	1.2
300	1	57.9	65.1	24.9	9.0	1.1	0.32	0.81	1.41	2.37	0.84	3.0

Table A6. Fit parameter of autofluorescence and WGA-ICC in mucins shown in Figure 4-12 and Figure 4-13. τ_i: fluorescence lifetime of the *i*-th decay component in ns, α_i the corresponding relative amplitude in %, $\bar{\tau}_{pop}$: mean fluorescence lifetime and χ^2_{red}: reduced chi square. Experimental conditions: λ_{ex} = 530 nm, λ_{em} > 545 nm, T=37°C.

Sample	c_{ICC} (µM)	$\boldsymbol{\alpha_1}(\%)$	$\boldsymbol{\alpha_2}(\%)$	$\boldsymbol{\alpha_3}(\%)$	$\boldsymbol{\alpha_4}(\%)$	$\boldsymbol{\tau_1}(\mathrm{ns})$	$\boldsymbol{\tau_2}(\mathrm{ns})$	$\boldsymbol{\tau_3}(\mathrm{ns})$	$\boldsymbol{\tau_4}(\mathrm{ns})$	$\boldsymbol{\bar{\tau}_{pop}}$	$\boldsymbol{\chi^2_{red}}$
Murine mucus	0	68.0	24.6	7.4		0.3	1.5	5.4		2.8	1.9
Mucin type II	0	57.4	29.6	13.0		0.2	1.1	4.0		2.5	1.1
HT29-mtx (blue)	0	46.9	36.0	15.8	1.3	0.4	1.5	2.4	4.3	1.7	2.5
HT29-mtx (magenta)	0	63.5	22.0	13.0	1.5	0.3	1.2	2.1	3.6	1.5	4.5
WGA-ICC	0.1	90.4	8.7	0.9		0.3	1.1	4.6		0.9	3.8
	0.2	91.6	7.8	0.6		0.3	1.0	4.5		0.7	5.4
	0.4	90.9	8.7	0.5		0.3	0.9	3.9		0.6	5.2
Diluted murine mucus +WGA-ICC	0.1	91.5	7.2	1.3		0.3	1.1	4.1		1.0	3.6
	0.2	92.0	7.0	1.0		0.3	1.0	4.0		0.8	4.9
	0.4	93.2	6.2	0.6		0.3	0.9	3.8		0.6	4.4
	0.6	92.9	6.6	0.5		0.3	0.8	3.6		0.5	6.4
	0.8	93.0	6.6	0.4		0.3	0.8	3.5		0.5	8.1
	1.0	93.2	6.4	0.4		0.3	0.8	3.5		0.5	2.4
	2.0	92.2	7.4	0.4		0.3	0.7	2.9		0.4	4.2
Undiluted murine mucus +WGA-ICC	0.3	86.5	11.2	2.3		0.3	1.1	3.4		1.1	2.8
WGA-ICC in PBS	1.0	95.1	4.8	0.2		0.2	0.7	2.0		0.3	4.0

Table A7. Fit parameter of 0.3 µM WGA-ICC in murine mucus of the small intestine shown in Figure 4-19. τ_i: fluorescence lifetime of the *i*-th decay component in ns, α_i the corresponding relative amplitude in %, $\bar{\tau}_{pop}$: mean fluorescence lifetime and χ^2_{red}: reduced chi square. "u" denotes the undiluted samples and accordingly "d" means diluted samples. Experimental conditions: λ_{ex} = 530 nm, λ_{em} > 545 nm, T=37°C.

	Sample		OD (600nm)	α_1(%)	α_2(%)	α_3(%)	τ_1(ns)	τ_2(ns)	τ_3(ns)	$\bar{\tau}_{pop}$	χ^2_{red}
Ampicillin + Gentamicin	1	u	0.84	91.1	8.3	0.7	0.3	0.9	3.1	0.6	8.8
		d	0.47	93.3	6.4	0.3	0.2	0.8	3.1	0.4	7.6
	2	u	1.85	73.2	24.4	2.4	0.4	1.3	3.9	1.3	4.4
		d	1.17	82.4	16.0	1.5	0.3	1.1	3.5	0.9	7.7
	3	u	1.93	74.7	23.5	1.8	0.4	1.2	3.7	1.1	4.4
		d	1.60	77.8	18.9	3.3	0.3	1.2	3.1	1.1	3.3
	4	u	0.38	90.9	8.7	0.5	0.3	0.9	3.4	0.6	4.1
		d	1.18	91.0	8.5	0.5	0.2	0.7	2.7	0.4	3.4
	5	u	2.02	77.1	21.0	1.9	0.4	1.1	3.3	1.0	3.0
		d	1.49	86.1	13.1	0.8	0.3	0.9	3.3	0.7	6.2
Meropenem + Vancomycin	6	u	1.72	75.0	22.7	2.3	0.4	1.1	3.1	1.0	3.3
		d	1.65	81.0	17.4	1.7	0.3	1.0	3.2	0.9	4.0
	7	u	2.21	80.5	18.6	1.0	0.4	1.5	5.0	1.2	5.3
		d	1.72	87.5	11.6	0.9	0.3	1.0	3.4	0.7	5.8
	8	u	2.64	76.6	21.6	1.7	0.4	1.2	4.0	1.1	4.3
		d	1.38	83.5	15.2	1.3	0.3	1.1	4.0	1.0	11.2
	9	u	-0.05	89.8	9.7	0.6	0.3	0.7	2.7	0.5	2.5
		d	0.13	93.2	6.6	0.3	0.2	0.7	2.7	0.4	5.2
	10	u	0.65	87.3	12.0	0.6	0.3	0.9	3.5	0.6	10.0
		d	0.37	90.4	9.1	0.4	0.3	0.8	3.0	0.5	4.8
	Ref1	u	1.74	88.2	10.4	1.5	0.3	1.0	3.4	0.9	6.0
		d	1.68	91.7	7.3	1.0	0.3	1.0	3.3	0.7	7.2
	Ref2	u	2.62	83.2	14.8	2.0	0.3	1.4	3.8	1.2	6.6
		d	2.36	90.0	8.5	1.6	0.3	1.2	3.3	0.9	5.7
	Ref3	u	3.58	82.3	15.2	2.4	0.3	1.2	3.6	1.2	7.2
		d	2.58	86.0	11.6	2.4	0.3	1.1	3.2	1.0	4.1

Table A8. Fit parameter of 0.3 µM WGA-ICC in murine mucus of the colon and cecum. τ_i: fluorescence lifetime of the *i*-th decay component in ns, α_i the corresponding relative amplitude in %, $\bar{\tau}_{pop}$: mean fluorescence lifetime and χ^2_{red}: reduced chi square. "u" denotes the undiluted samples and accordingly "d" means diluted samples. Experimental conditions: λ_{ex} = 530 nm, λ_{em} > 545 nm, T=37°C.

	Sample		OD (600nm)	$\boldsymbol{\alpha_1}(\%)$	$\boldsymbol{\alpha_2}(\%)$	$\boldsymbol{\alpha_3}(\%)$	$\boldsymbol{\tau_1}(\mathrm{ns})$	$\boldsymbol{\tau_2}(\mathrm{ns})$	$\boldsymbol{\tau_3}(\mathrm{ns})$	$\boldsymbol{\bar{\tau}_{pop}}$	$\boldsymbol{\chi^2_{red}}$
Ampicillin + Gentamicin	1	u	0.55	93.2	6.3	0.5	0.3	0.8	3.7	0.6	9.0
		d	0.32	94.6	5.0	0.4	0.2	0.8	3.5	0.5	7.3
	2	u	2.55	84.8	13.3	1.8	0.4	1.3	4.5	1.2	4.7
		d	1.37	91.5	7.6	0.9	0.3	1.0	3.9	0.8	7.0
	3	u	1.33	91.2	7.8	1.0	0.3	1.0	3.3	0.7	3.4
		d	0.84	93.5	5.8	0.7	0.3	1.0	3.2	0.6	5.1
	4	u	0.80	93.4	5.8	0.8	0.3	1.0	3.9	0.7	5.9
		d	0.47	93.8	5.5	0.7	0.3	0.8	3.7	0.6	7.1
	5	u	1.78	83.6	14.6	1.8	0.4	1.3	4.0	1.1	5.2
		d	--	--	--	--	--	--	--	--	--
Meropenem + Vancomycin	6	u	1.84	90.1	8.9	1.0	0.3	1.1	4.0	0.9	5.7
		d	0.95	92.5	6.6	0.9	0.3	1.0	3.8	0.7	2.9
	7	u	2.12	83.4	13.9	2.7	0.3	1.3	3.3	1.2	6.3
		d	1.11	84.2	13.6	2.2	0.3	1.4	3.7	1.2	8.1
	8	u	1.57	84.2	13.6	2.3	0.4	1.3	4.7	1.4	4.7
		d	1.85	92.6	6.5	0.9	0.3	1.2	4.4	0.9	6.4
	9	u	1.63	91.8	7.4	0.9	0.3	1.1	4.1	0.8	7.4
		d	0.82	93.7	5.8	0.5	0.2	0.8	3.1	0.5	8.6
	10	u	1.12	91.6	7.3	1.1	0.3	1.1	4.5	0.9	4.3
		d	0.75	91.3	7.9	0.7	0.3	0.7	3.1	0.5	2.5
	Ref1	u	0.55	93.2	6.3	0.5	0.3	0.8	3.7	0.6	6.2

Table A9. DL stability against enzymatic digest by endogenous enzymes of skin cells was tested using 53 nmol of DL and cell lysate of $5x10^5$ normal human keratinocytes (NHK) grown in monolayer cultures. For comparison, also esterase from rabbit liver (RLE) was used. NHK cell lysate was obtained by sonicating NHK cells for 60 min, and collecting the supernatant after centrifugation. For RLE, 0.3 mU was chosen as this enzyme activity hydrolyzes 53 nmol of a standard substrate in 120 min. In addition, also 10-fold and 10^4-fold excess of RLE was used and is shown for comparison. Percentage of intact DL was calculated based on ESI TOF mass spectrometry peak areas. Only at the highest RLE concentration (10,000-fold excess) a minor increase of free RhoB was detected. DL before digestion contained about 3% of free dye (Figure A3), which is well within the purity of the sample.

Enzymatic digest by	**Incubation Time (min)**	**Intact Dual Label (%)**
NHK lysate	60	(100±2)
NHK lysate	120	(100±2)
0.3 mU RLE	120	(98±2)
3.3 mU RLE	120	(98±2)
3.3 U RLE	30	(99±2)
3.3 U RLE	60	(97±2)
3.3 U RLE	120	(96±2)

Selbstständigkeitserklärung

Name: Stellmacher

Vorname: Johannes

Ich erkläre gegenüber der Freien Universität Berlin, dass ich die vorliegende Dissertation selbstständig und ohne Benutzung anderer als der angegebenen Quellen und Hilfsmittel angefertigt habe. Die vorliegende Arbeit ist frei von Plagiaten. Alle Ausführungen, die wörtlich oder inhaltlich aus anderen Schriften entnommen sind, habe ich als solche kenntlich gemacht. Diese Dissertation wurde in gleicher oder ähnlicher Form noch in keinem früheren Promotionsverfahren eingereicht.

Mit einer Prüfung meiner Arbeit durch ein Plagiatsprüfungsprogramm erkläre ich mich einverstanden.

Datum: _____ Unterschrift: _____

Danksagung

Ich möchte die Gelegenheit nutzen, um Prof. Dr. Ulrike Alexiev zu danken für die Gelegenheit in Ihrer Arbeitsgruppe dieses Forschungsvorhaben zu verwirklichen. Der vitale Austausch von Ideen, Ratschlägen und Anregungen mit ihr haben diese Arbeit erst ermöglicht.

Ich möchte auch Prof. Dr. Holger Dau danken für die Bereitschaft sich als Zweitgutachter bereit zu erklären.

Ein besonderer Dank gebührt allen Kooperationspartnern für die Vorbereitung von Proben und die ergiebige Diskussion der Ergebnisse. Insbesondere danke ich Prof. Marcelo Calderón, Prof. Rainer Haag, Ernesto Osorio-Blanco, Gregor Nagel, und Lydia Bouchet aus dem Fachbereich Chemie der FUB, Prof. Monika Schäfer-Kortine, Christian Zoschke und Leonie Gronbach aus dem Institut für Pharmazie der FUB, Prof. Martina Meinke, Silke Lohan und Pin Dong von der Charité Universitätsmedizin Berlin und Prof. Roland Netz, Robert Schulz und Amanuel Wolde-Kidan aus dem Fachbereich Physik der FUB.

Für die finanzielle Unterstützung in Form von Stipendien danke ich dem Graduiertenkolleg des SFB 1112, der Focus Area „NanoScale“ und dem Elsa-Neumann-Stipendium des Landes Berlin.

Ich danke allen Kollegen und ehemaligen Kollegen aus der Arbeitsgruppe für die Bereicherung durch fachlichen und persönlichen Austausch während und nach der Arbeitszeit. Besonders danke ich Tai-Yang Kim, Alexander Boreham, Alexander Wolf, Robert Brodwolf, Katja Ober, Jens Balke und Pierre Volz-Rakebrand für die schönen wie lehrreichen Stunden.

Für Zeit außerhalb der Uni möchte ich all meinen Freunden danken, für ihre Unterstützung durch ein offenes Ohr, eine helfende Hand oder einfach nur für den Ausgleich zur wissenschaftlichen Arbeit. Ich danke Tim, Lotte, Marius, Naima, Tamara, Valentin, Max, Anna, Antonia, Paula, Marco Vicky, Natascha, Robert, Eik, Alex und vielen wunderbaren Menschen mehr.

Zuletzt möchte ich noch meine Eltern und meiner Freundin Josi danken für die unendliche Geduld, moralische Unterstützung und das unerschöpfliche Vertrauen in mich in der finalen Zeit dieser Arbeit.